2023

Advancing cell signaling interrogation using theoretical and experimental approaches in eukaryotic model systems

BOSTON UNIVERSITY

COLLEGE OF ENGINEERING

Dissertation

ADVANCING CELL SIGNALING INTERROGATION USING THEORETICAL AND EXPERIMENTAL APPROACHES IN EUKARYOTIC MODEL SYSTEMS

by

CHUQIAO HUYAN

B.S., Beihang University, 2017
M.S., Boston University, 2020

Submitted in partial fulfillment of the

requirements for the degree of

Doctor of Philosophy

2023

Approved by

First Reader

Allyson E. Sgro, Ph.D.
Group Leader in Computation and Theory and 4D Cellular Physiology
Janelia Research Campus
Howard Hughes Medical Institute

Second Reader

Muhammad Zaman, Ph.D.
Professor and Vice Chair of Biomedical Engineering
Professor of Materials Science and Engineering
Assistant Professor of Global Health
Professor, Howard Hughes Medical Institute

Third Reader

Pankaj Mehta, Ph.D.
Professor of Physics
Professor of Biomedical Engineering
Professor of Computing and Data Sciences

Fourth Reader

Michael L. Smith, Ph.D.
Associate Professor of Biomedical Engineering
Associate Professor of Materials Science and Engineering

Fifth Reader

John T. Ngo, Ph.D.
Assistant Professor of Biomedical Engineering

Acknowledgments

I would like to acknowledge my mentors, colleagues, family, and friends for their support over the past five and half years. PhD is an exciting journey but far from an easy one, and it is the support from the people, both inside and outside of BU campus, that not only enabled this body of work but also helped me grow as a researcher.

Firstly, I would like to thank my advisor Dr. Allyson Sgro and my committee members Dr. Pankaj Mehta, Dr. Muhammad Zaman, Dr. Michael L. Smith, and Dr. John T. Ngo. for helping with my development as a scientist and making me feel you are in my corner throughout the years. Thank you Pankaj, for brainstorming ideas together in your office and providing critical inputs. Thank you Allyson, for introducing me to the fascinating world of microscopy, cellular dynamics, and quantitative biology. Knowing I had almost no background in quantitative biology, you generously took me in, provided a supportive environment for me to learn, and trusted me to explore new directions. I learned a great deal from you including but not limited to being rigorous in experiments and data analysis, and using writing as a way to shape ideas and inform experiment design.

I also feel privileged to have spent the past years with the Sgro lab members. Your critical feedback, generosity, and support have not only helped me develop scientifically but also made coming to the lab particularly enjoyable. Sam and Shwan, thank you for being great peer mentors and showing me the rope. Bre, thank you for all the insightful chats about science, generosity about sharing protocols, and friendship along the way, especially during the process of drafting this dissertation. Xinwen, thank you for being a great collaborator on work in Chapter 2, a source of critique and insights, and a caring roommate who kept me sane during the peak of the pandemic. Thank you Noshin for your inspiring ideas and hard work—Chapter 4 of this dissertation is made possible through working with you. Achini, Chiara, Emily, Mark, Maya, and Sophia, I learned so much from all of you. Thank you for the critical feedback during group meetings and on paper drafts, and thank you for

fostering a rigorous and collaborative environment.

I have been fortunate to work with several talented undergraduate researchers. Frank, Lordean, and Yujia, your enthusiasm and hard work kept reminding me of why I loved science in the first place. Learning and growing with you have been one of the best experiences during my PhD, and I am looking forward to seeing what you will do next.

Last but not least, I am grateful to my friends and family whose love and support have been essential throughout my PhD and beyond. Thank you my partner Long for being my best friend, and providing non-conditional support despite knowing all my drawbacks. Thank you to my Mom and Dad who instilled in me the love of science at a very young age, and who have always been my rock despite being on the other side of the video call.

ADVANCING CELL SIGNALING INTERROGATION USING THEORETICAL AND EXPERIMENTAL APPROACHES IN EUKARYOTIC MODEL SYSTEMS

CHUQIAO HUYAN

Boston University, College of Engineering, 2023

Major Professor: Allyson E. Sgro, Ph.D.
Group Leader in Computation and Theory and 4D Cellular Physiology Janelia Research Campus Howard Hughes Medical Institute

ABSTRACT

Understanding how cells use intracellular signaling to detect environmental changes and alter behaviors is essential for understanding a wide range of biological processes. The current gap of understanding resides in time-changing signals in individual cells (signaling dynamics) and cell-cell communication in multicellular contexts. Here, we used theoretical and experimental approaches to study cell signaling in two eukaryotic model systems, with a specific focus on processes that involve signaling dynamics and cell-cell communication. First, we focus on the starvation-induced population-level signaling oscillations in the social amoebae, *Dictyostelium discoideum*. By constructing a unifying theoretical framework, we were able to directly compare existing models and experimental data. From this systematic investigation, we identified that the key features in single-cell signaling networks that coordinate population-level oscillations are adaptive spiking and fold-change detection. We then applied experimental approaches to interrogate how temporal changes in a signaling molecule modulate cell behaviors (“signal decoding") and how environmen-

tal cues modulate the dynamics of a signaling molecule (“environment encoding") in mammalian fibroblast cells. First, we explored the impact of transient, direct activation of the cAMP pathway on cell migration using an optogenetic tool. We found that cell migration is inhibited by repetitive transient activation of the cAMP pathway, and the inhibitory effect depends on the extent of activation. By characterizing a series of single-cell behaviors, we found that transient activation of the cAMP pathway induces reversible cell contractile force relaxation and actin cytoskeleton reorganization, both of which can potentially mediate migration inhibition. Further, we confirmed that the induced actin cytoskeleton reorganization is mediated by calcium signaling. Next, we investigated cytosolic calcium dynamics in the presence of a common culture media supplement, serum. We found serum induces trains of calcium spikes and further identified a major serum component mediating this response as lysophosphatidic acid (LPA). Although features of calcium spiking display a great amount of variability among cells, the faction of spiking cells and spiking frequency generally encode the concentration of environmental LPA. Through a series of pharmaceutical inhibitor experiments, we identified major sources of calcium ions as well as other pathways that shape calcium spiking. This body of work demonstrates the different utilities of theoretical modeling and experiments in understanding cell signaling which provides an advanced understanding of biological processes that involve signaling dynamics or cell-cell communication.

Contents

List of Tables

List of Figures

List of Abbreviations

2D	.....	Two Dimensional
ACA	.....	Adenylyl Cyclase
ATP	.....	Adenosine 5′-Triphosphate
AUC	.....	Area-Under-Curve
CaAR	.....	Calcium-Mediated Actin Reset
cAMP	.....	Cyclic-Adenosine Monophosphate
CAR1	.....	Cyclic AMP Receptor 1
CCh	.....	Carbachol
CDINFB	.....	Coupled Direct and Indirect Negative Feedback
CNG	.....	Cyclic Nucleotide–Gated
Dicty	.....	*Dictyostelium discoideum*
DMD	.....	Digital Micromirror Device
DMEM	.....	Dulbecco's Modified Eagle Medium
EGF	.....	Epidermal Growth Factor
ER	.....	Endoplasmic Reticulum
ERK	.....	Extracellular Signal-Regulated Kinases
ERK2	.....	Mitogen-Activated Protein Kinase 1
FA	.....	Focal Adhesion
FCD	.....	Fold-Change Detection
FHN	.....	FitzHugh–Nagumo
FRET	.....	Förster Resonance Energy Transfer
fskn	.....	Forskolin
FWHM	.....	Full-Width at Half Maximum
GPCR	.....	G-Protein-Coupled Receptor
GsM	.....	GsMTx4
IBMX	.....	Isobutylmethylxanthine
IFFL	.....	Incoherent Feedforward Loop
INF2	.....	Inverted Formin-2
IP_3	.....	Inositol 1,4,5-Trisphosphate
IP_3R	.....	Inositol 1,4,5-Trisphosphate Receptor
IPNFB	.....	Interlocking Positive-Negative Feedback
ISI	.....	Interspike Interval
Ki	.....	Ki16425
LINC	.....	Linker of Nucleoskeleton and Cytoskeleton
LPA	.....	Lysophosphatidic Acid
LPAR	.....	Lysophosphatidic Acid Receptor
LPP	.....	Lipid Phosphate Phosphatases
MDCK	.....	Madin-Darby Canine Kidney
MEM	.....	Minimum Essential Medium

MLCP	.....	Myosin-Light-Chain Phosphatase
NES	.....	Nuclear Export Signal
NGF	.....	Nerve Growth Factor
Nif	.....	Nifedipine
PBS	.....	Phosphate-buffered saline
PDE	.....	Phosphodiesterase
PDGF	.....	Platelet-Derived Growth Factor
PIP_3	.....	Phosphatidylinositol 4,5-Bisphosphate
PKA	.....	Protein Kinase A
PKI	.....	Protein Kinase Inhibitor Peptide
PLC	.....	Phospholipase C
PMCA	.....	Plasma Membrane Calcium ATPase
RegA	.....	Intracellular cAMP-Specific Phosphodiesterase
RhoA	.....	Rat Associated Sarcoma
ROCK	.....	Rho-Associated Kinase
SACC	.....	Stretch-Activated Calcium Channel
SERCA	.....	Sarco/Endoplasmic Reticulum Calcium ATPase
SFI	.....	Stress Fiber Integrity
SKF	.....	SKF 96365
SOCE	.....	Store-Operated Calcium Entry
TF	.....	Transcription factor
TFM	.....	Traction Force Microscopy
TG	.....	Thapsigargin
UV	.....	Ultraviolet
VGCC	.....	Voltage-Gated Calcium Channel
Y27	.....	Y27632

Chapter 1

Introduction

1.1 Cell signaling is a process that takes environmental inputs and modulates cellular outputs

Eukaryotic cells exist in a constantly changing environment. Single cells need to sense and respond to those changes to maintain homeostasis at cellular, tissue, and organismal levels. Like parts in any engineering system, single cells serve as essential components of the multicellular biological systems, and the proper response of single cells is essential for the normal functioning of the whole system. We can borrow the language from engineering to describe the process of cells responding to environmental changes (an idea echoes that from previous reviews such as [1, 2, 3]). Generally, cells perceive information inputs (environmental changes) through sensing external cues such as changes in biochemical molecule concentrations and changes in surrounding physical forces. The input is then fed into a signal processing unit (cell signaling network) inside the cells, usually consisting of multiple signal processing steps including chemical reactions, diffusion, and physical transport. The outputs from those processing units are translated to generate cellular outputs (cell behavioral change) such as gene expression, fate decision, cell migration, etc. The process during which cells perceive and process external inputs, transmit information through the intracellular networks, and eventually modulate cell behaviors is termed cell signaling (Fig 1·1).

An example of how cells use signaling to respond to environmental inputs and modulate cellular outputs is the signaling molecule calcium [4, 5, 6]. Firstly, cytosolic calcium is reg-

ulated by a wide range of environmental inputs. The environmental biochemical molecules that can modulate cytosolic calcium activity include ATP which acts on fibroblasts [7], carbachol (CCh) which acts on HEK cells [8], peptide–MHC complex which acts on immune cells [9, 10], and lysophosphatidic acid (LPA) which acts on astrocytes [11], fibroblasts [12], and keratinocytes [13]. Cytosolic calcium can also be regulated by physical cues in the environment, including stretch [14], squeeze [15], fluid shear stress [16], and substrate stiffness [17, 18]. Secondly, calcium activity modulates a wide range of downstream effectors including cellular contractility [19], actin cytoskeleton organization [14, 16], migration [20, 21], proliferation [22], gene expression (reviewed in for example [4, 5]) and secretion [23]. The example of calcium signaling highlights how detecting environmental cues and coordinating cell behaviors is driven by complex cell signaling networks.

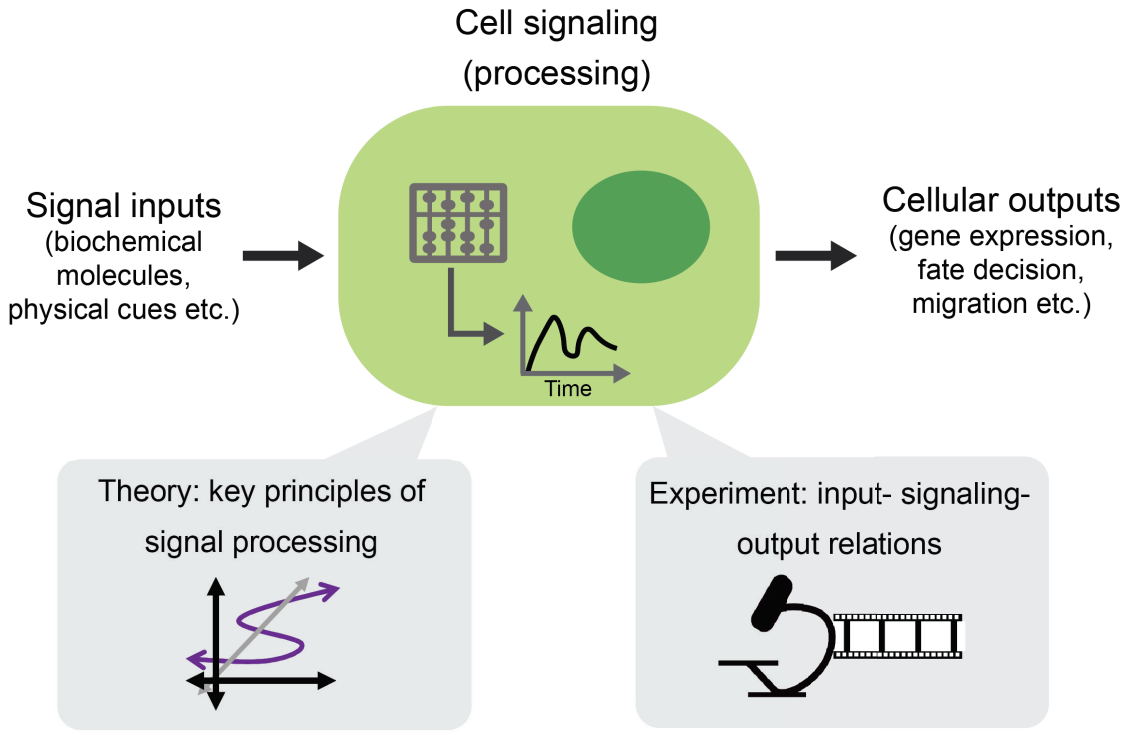

Figure 1·1: Two approaches for studying cell signaling.

1.1.1 Challenges and gaps in studying cell signaling

Our knowledge of cell signaling has taken the form of signaling networks, static maps consisting of hundreds of relevant signaling molecules and their interactions within a single cell (for example, the cAMP network delineated in [24]). However, these maps lack two essential types of information. Firstly, these maps do not reflect the dynamics of the signaling molecules in the system. Secondly, these maps do not contain information about communication between cells. As will be discussed below, both types of information play important roles in regulating biological processes in multicellular contexts.

Over the past decade, more examples started to emerge which showed that the dynamics, rather than the steady-state activity of signaling molecules, mediate cells' response to external cues (reviewed in [25]). For instance, in PC-12 cells, epidermal growth factor (EGF) treatment leads to transient ERK activation which results in cell proliferation, but nerve growth factor (NGF) treatment induces sustained ERK activation which results in cell differentiation [26]. Another example is that UV and γ irradiation elicit different dynamical profiles of p53 activity (pulsatile versus sustained activation) [27] which leads to different gene expression profiles that determine diverging cell fates (DNA damage recovery versus senescence) [28]. The last example is that multiple types of extracellular ligands are able to induce trains of cytosolic calcium spikes, with the concentration of those ligands encoded in the frequency or amplitude of the calcium spikes [29, 6]. The dynamical features of these calcium activities in turn modulate cell behaviors such as migration and gene expression [30, 31, 32]. These examples highlight the importance of studying the dynamic activity in cell signaling networks.

Cell-cell communication is another area that has started to receive more attention in the context of cell signaling. For example, communities of bacteria communicate with each other through secreting chemicals that help them modulate behaviors in response to changes in cell density or species composition, a process called quorum-sensing [33, 34].

Similar mechanisms can be found in a group of yeast as they collectively resist heat-induced damages [35] and cells in mammalian skin near hair follicles during hair regeneration [36]. Another type of cell-cell communication is characterized by cells modulating the dynamics of their environment and responding to these dynamic cues (termed dynamical quorum sensing [37]). For instance, the starvation-induced collective signaling in the social amoebae cells is mediated by the pulsatile production and release of the signaling molecule cAMP [38]. By detecting and responding to the dynamical changes of cAMP, cells are able to coordinate group-level behaviors manifested as cAMP oscillations and waves. A similar mechanism has been shown to drive metabolic oscillations in yeast populations upon nutrient source change [39, 40]. These gaps, the need to study the dynamics of cell signaling, and the need to study signaling in a native, multicellular context, have made understanding cellular signaling a challenge. Strategies that have yielded insights into this challenge have used both experimental and theoretical approaches.

1.2 Two approaches to study cell signaling

Two major approaches have been used to study cell signaling: theoretical modeling and experiments (Fig 1·1). For processes whose signaling responses are well-characterized or whose pathways are rather well-studied, theoretical modeling can be a powerful tool to facilitate not only testing different mechanisms underlying a biological process by quantitative formulation but also extracting basic principles or rules driving the biological processes. On the other hand, for processes in which the relevant signaling molecules are yet to be identified or the signal transduction is less well-characterized, experimental approaches are usually used to unveil how external inputs alter signaling molecules inside the cells, how the information is transmitted in the pathway, and how cellular outputs are modulated.

1.2.1 Theoretical approaches to illuminate essential principles about cell signaling

In the context of studying cell signaling, theoretical modeling can be used in several ways: (1) to quantitatively show the validity of potential mechanisms underlying a biological process, (2) to estimate unknown parameters, (3) to distinguish alternative mechanisms by generating falsifiable predictions, and (4) to distill essential mechanisms/principles that drive processes [41, 42, 43, 44]. The last usage of theoretical models can be a powerful way for us to understand cell signaling: it can help us identify the essential rules guiding a process as well as distill common principles that are generalizable across different processes.

An example that highlights this particular usage of modeling is the principles underlying collective oscillations in a group of cells that are coupled through environmental signals. This behavior is widely observed in cells that can respond to time-varying environmental signals and in turn alter the dynamics of these signals. Examples of this include the abovementioned collective signal oscillations in the social amoebae cells [38] and glycolic oscillations in yeast [40, 39]. Theoretical work suggested generalized requirements for initiating collective oscillations: cells need to anticipate the environmental signal and the signals generated by cells need to have sufficient amplitude [45]. This simple principle was able to predict key system behaviors such as threshold cell density at the onset of collective oscillations that were confirmed by experimental data in both the amoebae cells and yeast. This work demonstrates the utility of theoretical models to extract essential principles in signaling-mediated biological processes.

In addition to theory, other types of computational approaches, specifically bioinformatics/systems approaches, have been developed to study cell signaling. Initially, when full genome data became available, computational strategies were used to find and annotate genes [46]. More recently, with the advancement of experimental techniques, researchers are able to acquire large datasets containing information about mRNA translation (tran-

scriptomics), protein expression (proteomics), and molecular interactions in response to external inputs or in the contexts of different diseases [46, 47]. Based on these data, computational approaches are developed to generate or infer signaling networks that consist of interactions between molecular players. These networks can then be subjected to further analysis such as parameter estimation, module identification, and network attribute analysis, all of which advance the understanding of the general principles as well as specific characteristics of the networks [47, 48, 49]. For example, systems biology approaches were used to study variability in calcium signaling responses. By reconstructing calcium signaling networks and estimating model parameters based on experimental data, researchers found that the calcium signaling variability is likely due to the differences in cell states (model parameters) [50]. Although will not be the focus of this Dissertation, bioinformatics/ systems biology methods have offered a path to extensive and in-depth investigations into cell signaling networks.

1.2.2 Experimental approaches to study cell signaling

For signaling processes where the key signaling molecules and interactions are unclear, people generally apply experimental approaches to identify the key molecules and delineate the interactions. Experimental investigations into cell signaling can be roughly split into two classes based on which part of the process (inputs versus outputs) the study focuses on. Studies about “environment encoding" focus on how environmental cues change intracellular signaling pathways, whereas studies on “signal decoding" focus on how intracellular signaling is translated to alteration in cell behavior. To understand environment encoding, one can modulate the external environment and characterize the intracellular signaling molecule of interest. One can also gather a more detailed picture of the network by perturbing other potentially relevant nodes in the network. To understand signal decoding, one of the best approaches is to directly and specifically modulate the signaling molecule(s) of interest and characterize the resulting cell behavior.

Technological advancements have enabled direct measurements of not only the steady-state activity but also the dynamic changes of signaling molecules inside the cells [51]. Moreover, development in techniques such as microfluidics and optogenetics enabled accurate control over the environmental cues as well as the dynamics of intracellular signaling molecules [52].

A set of studies on intracellular calcium signaling exemplify how technological advancements allowed us to characterize and dissect the input-to-signaling dynamics, signaling dynamics-to-output, and the role of cell-cell coupling. Generally, a calcium signaling system functions by generating a pulse or trains of transients (spikes) of calcium activity [4]. By visualizing calcium dynamics using genetically-encoded calcium reporters, researchers established how calcium dynamics are modulated by changes in environmental cues. For instance, the frequency of calcium spiking has been shown to encode the concentration of external ligands in multiple cell types (reviewed in [6, 29]). Further, the use of microfluidics allowed controlled input of extracellular ligands, specifically in consecutive steps of different concentrations. These experiments helped suggest that calcium dynamics encode fold difference of ligand concentrations [8]. On the other hand, by experimentally modulating the calcium pathway using optogenetics, researchers were able to delineate how the calcium dynamics affect cell behaviors such as gene expression [32], actin cytoskeleton organization [53], and cell migration [54, 55]. Additionally, by modulating cell-cell communication strength through changing cell density, researchers revealed that a potential source for the large variability in calcium spiking frequency in a group of cells is calcium ion exchange between cells [56]. These experiments helped formulate an understanding of how external cues shape calcium dynamics, how these dynamics alter cell behaviors, and the role of cell-cell communication in determining calcium dynamics in multicellular contexts.

1.3 Summary

In this Dissertation, we took two separate approaches, the theoretical approach and the experimental approach, to study cell signaling in two eukaryotic model systems.

In **Chapter 2**, we focused on the single-cell level signaling processing features that coordinate population-level signaling oscillations in the social amoebae, *Dictyostelium discoideum* (*Dicty*). We took different models that suggest different single-cell signaling mechanisms and applied a unified simulation framework. This allowed us to directly compare the models and experimental measurements, which suggested single-cell adaptive spiking and fold-change detection are the essential single-cell features driving population signaling oscillations.

Using the experimental approach, we studied how an intracellular signaling molecule modulates cellular outputs (**Chapter 3**) and how the dynamics of another intracellular signaling molecule encode environmental inputs (**Chapter 4**) in the context of mammalian cell culture. In **Chapter 3**, we studied how transient, direct activation of the cAMP/PKA pathway modulates behaviors related to cell migration. Harnessing an optogenetic tool that allowed for tunable activation of the cAMP/PKA pathway, we found that higher activity of this signaling pathway inhibits cell migration. We further found that the inhibition of cell migration potentially resulted from changes in cell contractile forces and actin cytoskeleton structure, and the reorganization of the actin cytoskeleton is potentially mediated by cytosolic calcium. Next, in **Chapter 4**, we characterized calcium signaling dynamics in response to serum, a common component in cell culture media. We found that serum supplement led to calcium spiking in fibroblast cells, and identified one of the key serum components responsible for calcium spiking as lysophosphatidic acid (LPA). We then found that the features of calcium dynamics encode information about LPA concentration. Further, we identified major sources of calcium ions as well as other pathways that mediate and shape calcium spiking that is induced by LPA.

Together, these results demonstrate the different utilities of theoretical modeling and experiments in understanding cell signaling in two different systems: the social amoebae and mammalian cell culture. From these studies, we derived an advanced understanding of biological processes that involve signaling dynamics or cell-cell communication.

Chapter 2

Identifying key single-cell features driving robust collective oscillatory signaling in *Dictyostelium*

2.1 Disclosure & Copyright Statement

This chapter is a modified version of "Robust collective oscillatory signaling requires single-cell excitability and fold-change detection" by Chuqiao Huyan, Alexander Golden, Xinwen Zhu, Pankaj Mehta, and Allyson E. Sgro, 2021. BioRxiv. © The Authors.

2.2 Introduction

Cellular populations often work together to engage in complex emergent multicellular behaviors. These behaviors range from the computations performed by populations of neurons [57], to coordinated growth within a biofilm composed of thousands of bacteria [58, 59]. Remarkably, these population-level behaviors are often coordinated by biochemical intracellular signaling networks. This decentralized control of population-wide behaviors by internal signaling networks is impressive given that individual cells often have access to very limited information about their immediate surroundings. Furthermore, cell-cell communication mechanisms commonly utilize only a handful of signaling molecules, limiting information transmission between cells. This raises natural questions about the strategies cells employ to use this limited information to robustly control emergent population behaviors in a wide variety of contexts.

To address this question, we focus on one of the most notable and extensively-studied

examples of collective multicellular phenomena, the starvation response of the social amoeba *Dictyostelium discoideum*, where cells transition from a free-living unicellular state to a multicellular aggregate [38, 60]. Upon starvation, *Dictyostelium* cells initiate a developmental program where some cells start releasing pulses of cyclic AMP (cAMP) into the external space [61, 62, 63]. These oscillatory pulses are relayed through the population, creating external cAMP waves that act as a chemoattractant directing cell migration toward the source of cAMP during aggregation. These waves allow *Dictyostelium* to self-organize and develop into a stalk-and-spore structure in complex and ill-defined environments over group sizes that can vary by many orders of magnitude [38]. This type of collective oscillatory phenomena is found across a wide range of biological systems, ranging from pacemaker-driven electrical oscillations driving contractions in the heart [64] to other biochemically-coupled microbial systems that synchronize their internal states in response to environmental changes. For example, yeast exhibit sustained glycolic oscillations under specific environmental conditions [40, 65] while bacterial collectives pause and restart growth upon glutamate starvation and these are coupled to ion-driven electrical oscillations [58, 59]. Identifying how this level of control is achieved at the molecular level in these biochemically-coupled systems is still an open question as most studies on design principles that coordinate multicellular phenomena have focused on developmental networks in metazoans that use well-defined morphogen gradients to pattern their development [66, 67, 68, 69, 70].

Despite decades of work on this elegant phenomenon *Dictyostelium* exemplifies, identifying the critical features of single-cell signaling networks that drive this type of emergent population-level behavior poses a tremendous challenge as it requires identifying the specific underlying signaling network architecture. To begin to address this challenge, there has been a grand tradition of mathematical modeling to link the observed molecular and cellular behaviors to specific network architectures that can drive group-wide phenomena.

These models originally focused on population-wide oscillations based on biochemical data [71, 72, 73]. Recent experimental advances exploiting genetically-encoded cAMP sensors and microfluidic platforms have enabled measurements of single-cell signaling dynamics in both isolated cells and collectively-behaving populations, helping shed light on how the single-cell signaling network may be configured. [62, 63, 74, 75].

While all the models describing *Dictyostelium* signaling reproduce population-wide oscillations, not all of them produce the more complex single-cell and population behaviors revealed by these recent experiments. Furthermore, they make conflicting assumptions about the architectural features of single-cell signaling networks that lead to different behaviors beyond coordinated oscillatory signaling. Resolving these issues represents a major conceptual challenge because these models have different time and response scales with different arbitrary units. Here, we address this challenge by exploiting our recent single-cell measurements: when individual *Dictyostelium* cells are exposed to a threshold level of external cAMP stimulation, they respond with a characteristic adaptive pulse of internal cAMP with a reproducible timescale and magnitude [63]. We show below that we can use this characteristic cellular response to normalize the time and response amplitude scales of different mathematical models to one another to directly compare their behaviors. This allows us to screen for how accurately these mathematical models recapitulate experimentally-observed population and single-cell signaling phenomena from multiple experimental sources [62, 63, 74]. This analysis identifies the key signaling network features and single cell properties that are critical for driving population behaviors. Importantly, we find that single-cell excitability and fold-change detection are critical single-cell properties for robustly coordinating single cells through an external medium to drive population-wide oscillations.

2.3 Results

2.3.1 Simulation framework for comparing mathematical models of *Dictyostelium* signal relay

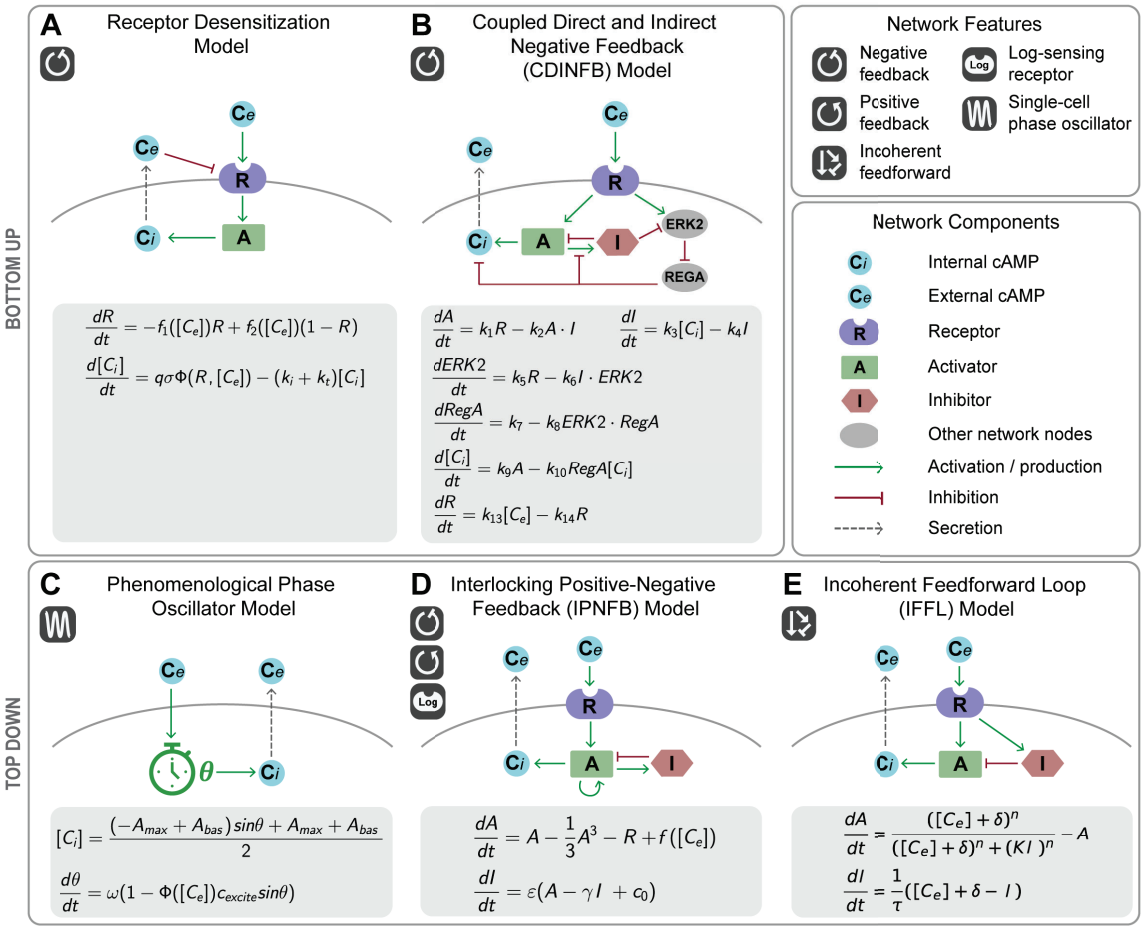

Figure 2·1: Five major mathematical models describing dynamical signaling relay behaviors in *Dictyostelium*. Models are abstracted as network diagrams with common signaling network components. The activator in each model either stands for the enzyme that directly produces cAMP (adenylyl cyclase) or internal cAMP itself. The top panel illustrates the bottom-up models based on receptor desensitization **(A)** and a coupled direct and indirect negative feedback (CDINFB) architecture **(B)** that use kinetic equations based on biological signaling networks. The bottom panel shows top-down models that use well-studied mathematical equations to recapitulate dynamics from recent experiments: a coupled phase oscillator model **(C)**, an interlocking positive-negative feedback (IPNFB) model that adapts the FitzHugh-Nagumo model framework and integrates a logarithmic sensing receptor module **(D)**, and an incoherent feedforward loop (IFFL) model **(E)**

.

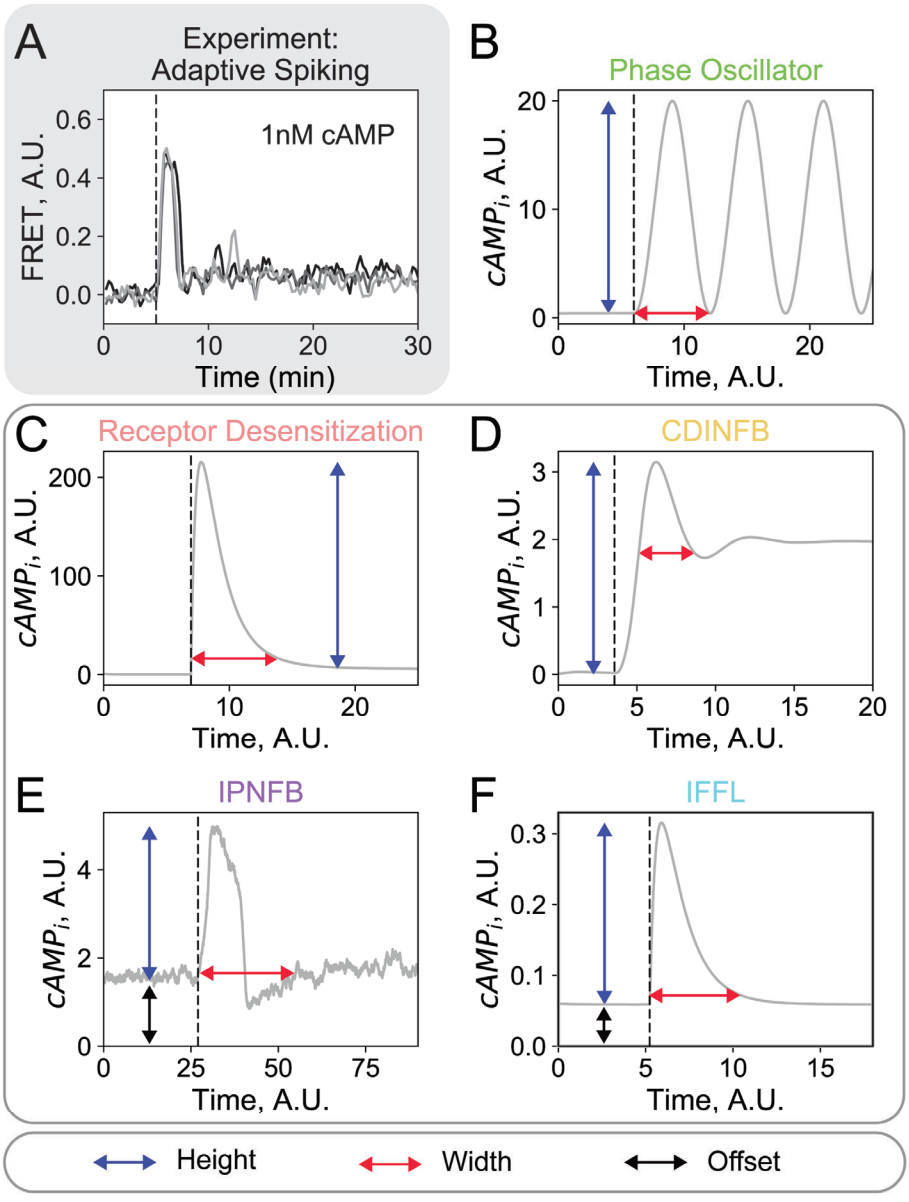

Figure 2·2: Normalizing model response and timescales to the characteristic adaptive spike in single cells

(A). Experimental data shows single *Dictyostelium* cells display an adaptive internal cAMP spike in response to a 1 nM external cAMP step input (n = 3 example cells). Data adapted from Sgro, et al. [63]. In each model, the time and response amplitude normalization parameters (time: red arrows; amplitude: blue arrows) are set to the height and width of either the oscillations **(B)** or the spike the model displays in response to 1 external arbitrary unit of cAMP **(C – F)**. In the IPNFB and IFFL models the response amplitude is offset to normalize their basal internal cAMP levels to 0 (offset: black arrows) **(E and F)**. In both the experimental data and model results, external cAMP is applied at the black dashed line. Input external cAMP concentrations were determined as described in the main text. Units shown in **B-F** are the original model units.

We analyze five major models that describe the *Dictyostelium* signal relay network (Figure 2·1). These models were developed over the last thirty-five years based on experimental observations and include both bottom-up mechanistic models that seek to directly relate variables to specific proteins [71, 73] and top-down phenomenological models that seek to abstract away molecular details yet still capture the observed dynamical behaviors [62, 63, 74]. In order to identify common features required to reproduce the observed dynamical behaviors and illuminate the design principles required for collective coordination, we classified models according to architecture and developed a unified simulation framework that allowed us to compare their behavior to both population and single-cell level experimental data. The different signaling network architectures are built up from different network design features. These features include control loops, such as positive feedback, negative feedback, and incoherent feedforward loops that can be integrated with one another. Other design features are logarithmic sensing receptors that sense order of magnitude changes in external cAMP inputs, and treating each cell as a phase oscillator. Furthermore, given recent work suggesting that noise plays a prominent role in population-wide coordination [62, 63], we constructed stochastic generalizations of the original deterministic models to understand the effect of noise on population-level behaviors. The models are implemented in Python using standard methods for solving ordinary differential equations (Figure 2·1) and their stochastic counterparts. The models are summarized in detail in the Appendix A, highlighting the underlying assumptions the models make about the network

architectures.

To permit direct comparison between the models, as well as to experimental data, we needed a common scale for three key parameters: external cAMP level, internal cAMP level, and time. To accomplish this, we normalized each model to match a characteristic experimental behavior: in response to a low-level 1 nM step of cAMP, single cells produce a spike of internal cAMP with reproducible height and width before returning to baseline (Figure 2·2A) [63]. For each model, we set 1 external arbitrary unit of cAMP equal to either the amount designated as 1 unit or 1 nM in the model [63, 62, 74] or the minimum amount of $[cAMP]_e$ that produced a robust spike of internal cAMP [71, 73] (Figure 2·2B-F). All models except the Phase Oscillator model display this spike, whereas phase oscillators are designed to bifurcate to oscillations at high levels of external stimulation, so we used either this spike or the oscillations to establish common internal cAMP levels and time units. Specifically, we set the internal cAMP response level of one arbitrary unit to the height of the Phase Oscillator oscillations at the equivalent of 10 μm external cAMP (Figure 2·2B) or the height of the internal cAMP response to 1 external arbitrary unit of cAMP (Figure 2·2C-F). Similarly, we set one arbitrary time unit to the intrinsic oscillation timescale in the Phase Oscillator model (Figure 2·2B) [62], the time to return to 5% of the internal cAMP amplitude over the post-stimulation lowest level of internal cAMP in the Receptor Desensitization, the CDINFB, and the IFFL models (Figure 2·2C-E) [71, 73, 74], and the adaptive spike timescale parameter set in the original paper in the IPNFB model (Figure 2·2F) [63].

2.3.2 Comparison of mathematical models to population and single cell experimental data

We compared dynamical behaviors displayed by the five different models against nine key dynamical behaviors observed in cellular populations and isolated single cells. The performance of the five models is summarized in Table 2.1 and full model details and simulation

results can be found in the Appendix A. For brevity, in the main text we limit our discussion to the four most informative behaviors for distinguishing between different network design features.

Population Behaviors

I. Sustained population cAMP oscillations and their repression by background cAMP application

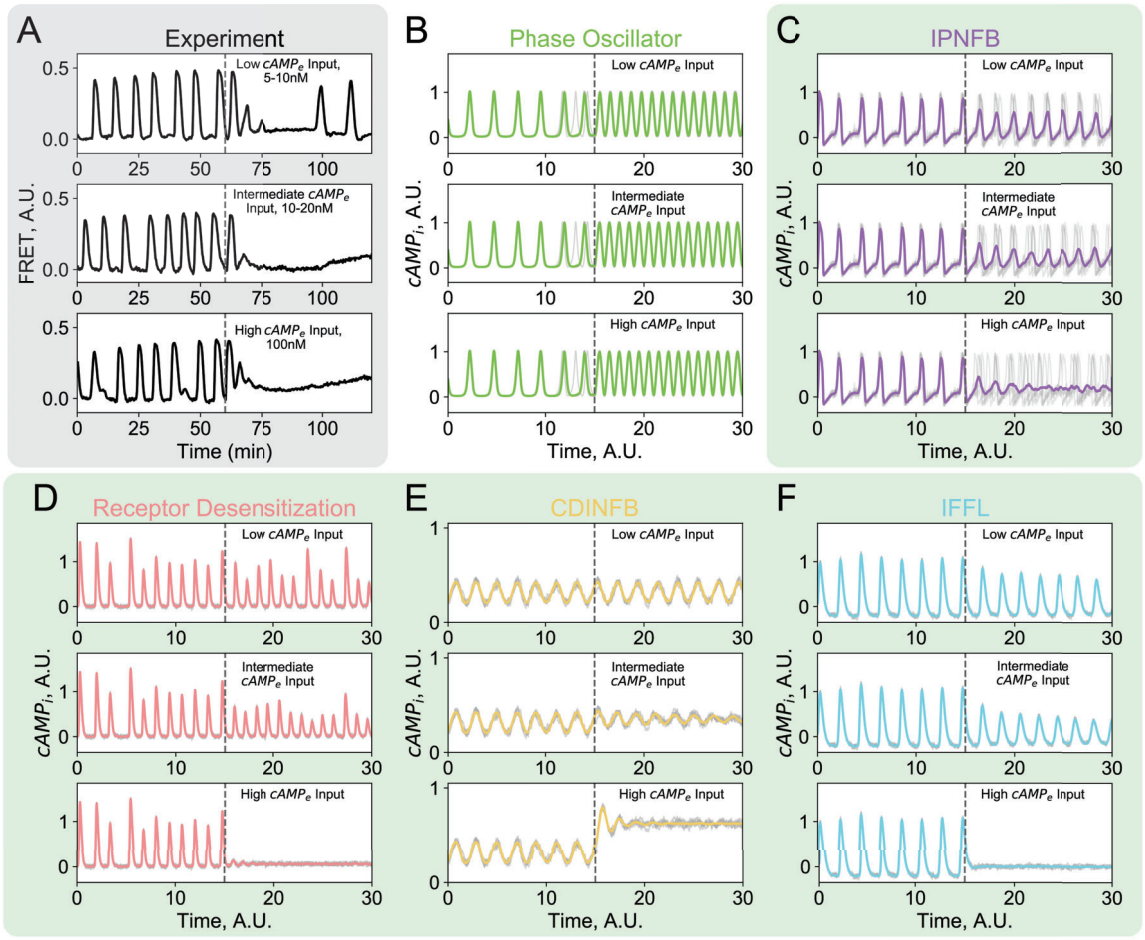

Figure 2·3: Evaluating models against population phenomena: population oscillations are suppressed by a step input of external cAMP.

The most distinctive signaling behavior *Dictyostelium* displays is synchronized cAMP oscillations across populations. These oscillations are mediated by cell-cell communication

(A) Experimental data adapted from Sgro, et al. [63] shows population-wide oscillations slow down upon low and intermediate external cAMP addition, and are completely suppressed by high concentrations of external cAMP. **(B)** The Phase Oscillator model does not reproduce the experimental data. The rest of the models investigated all qualitatively reproduce the experimental data, despite acting through two distinctive mechanisms. **(C)** In the IPNFB model, population oscillations slow down due to desynchronization between single cells upon external cAMP addition. **(D - F)** In the other three models, population oscillations slow down through inhibition of adaptive spike height in single cells. For model simulation results, solid colored traces are the mean internal cAMP of all the cells in the population, and gray traces represent single-cell dynamics from five cells in the population. The low, intermediate, and high cAMP levels in each model are determined arbitrarily, with a low external cAMP level slightly suppressing oscillations and a high level inhibiting the population oscillations entirely, except in the Phase Oscillator model as its oscillations speed up with increasing external cAMP. Gray dashed lines indicate the start of the step input of external cAMP. A gray shaded background highlights experimental data. A green shaded background indicates models that reproduce the experimental observations.

through a relay mechanism where cells produce cAMP internally upon detecting elevated levels of external cAMP. All of the models investigated recapitulate this phenomenon of synchronized population oscillations (Figure 2·3A, before external cAMP input). More recently, experiments demonstrate these collective oscillations can be suppressed by suddenly increasing the concentration of external cAMP (Figure 2·3A) [63]. All the models except for the Phase Oscillator model reproduce this behavior – the Phase Oscillator model displays the opposite behavior with higher background cAMP levels leading to faster and more coherent group oscillations (Figure 2·3B-F). This discrepancy suggests the observed population oscillations do not arise from a mechanism where coupled individual cells oscillate autonomously even in the absence of external cAMP.

In the remaining models, group oscillations are suppressed by background cAMP because the added cAMP masks the cell-secreted external cAMP that propagates through the population. However, this inhibition of population oscillations occurs through two distinct mechanisms depending on the model. One mechanism, exploited in the IPNFB model, is that raising background cAMP tunes the single-cell spiking rate and decreases the coherence of single-cell spiking events. As a result, the amplitude of the single-cell spikes

remains constant (Figure 2·3C, see gray traces for single cells) and the loss of collective oscillations is due to desynchronization between cells. The other mechanism, common to the remaining models, is that increasing background cAMP concentrations still result in coherent population-level oscillations, but now with a reduced oscillation amplitude. This can be seen in the simulation data where at intermediate background cAMP levels, single cells within the population still oscillate coherently, while the spike heights are reduced (Figure 2·3D - F, see gray traces for single cells). It should be possible to distinguish between these two mechanisms in future experiments by more extensively analyzing single-cell behaviors within populations in response to the addition of external cAMP.

II. Population oscillations depend on environmentally-mediated cell-cell coupling

Collective oscillations in *Dictyostelium* are mediated by the signaling molecule cAMP in a shared media. As a result, population-level oscillations depend strongly on environmental cell-cell coupling parameters such as cell density and the cAMP degradation rate (either through native enzymatic means using phosphodiesterases or through physical means such as fluid flow around the cells). How these parameters coordinate the emergence of population-wide oscillations can be experimentally explored by varying cell density and altering media flow rates over cells. Previous experimental work demonstrates that in most regimes, group oscillations emerge as cell-cell coupling strength increases through increasing cell seeding density or decreasing media flow rate. (Figure 2·4A) [62].

All of the models investigated qualitatively recapture the emergence of group oscillations as cell-cell coupling increases (Figure 2·4B-F). However, there are two key experimental features of the observed coupled oscillations that can be used to distinguish between models. First, these population-wide oscillations are experimentally observed across a large coupling parameter regime (Figure 2·4A). This observation is not reproduced by the Receptor Desensitization model, which displays collective oscillations only in a narrow regime (Figure 2·4B). The underlying reason is that sustained oscillations in this model are pos-

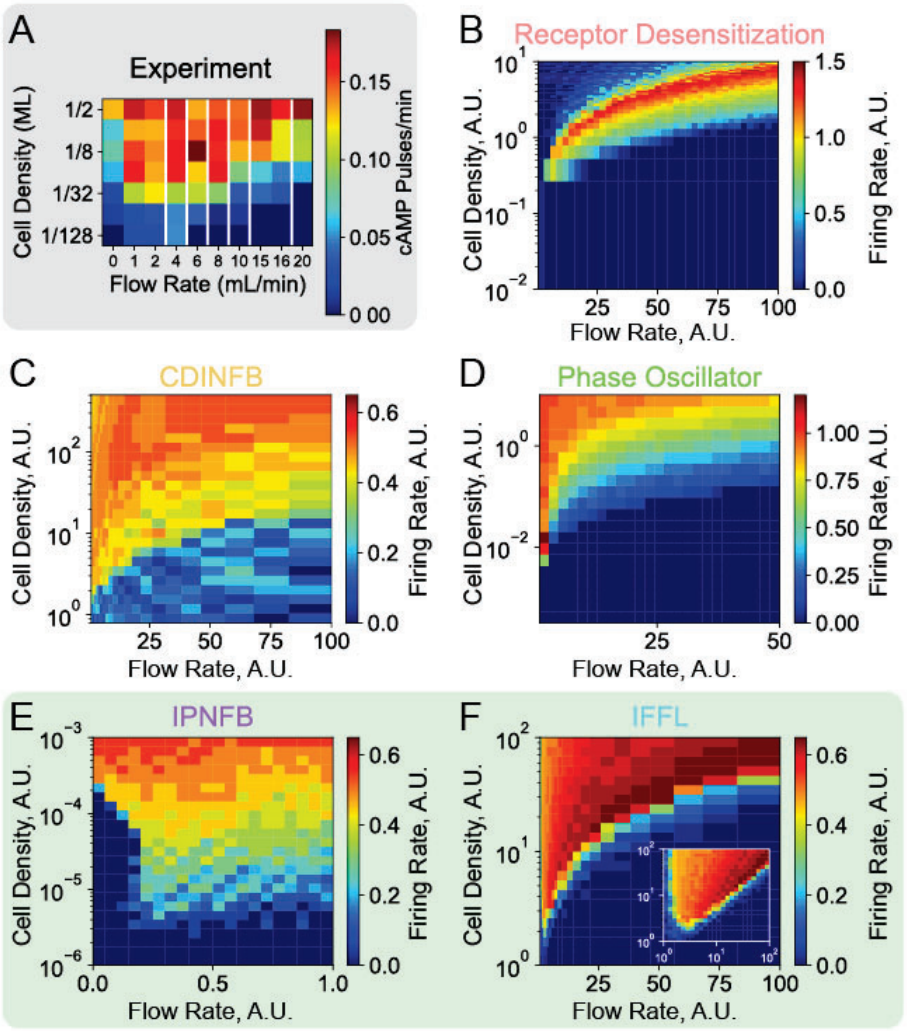

Figure 2·4: Evaluating models against population phenomena: population oscillations depend on cell density and external cAMP media flow rate.

(A) Experimental population firing rate phase diagram for *Dictyostelium* cells in a perfusion chamber with varying media flow rates and cell densities measured in fractions of a monolayer (ML) from Gregor, et al. [62]. **(B)** Unlike the experimental data, the Receptor Desensitization model only displays population oscillations in a narrow parameter range. **(C and D)** The CDINFB and Phase Oscillator models successfully reproduce collective oscillations over a large range of parameter space, but do not capture the dynamic death region at low flow rates found in the experimental data. **(E and F)** The IPNFB and IFFL models perform the best at reproducing the experimental data because both models display robust oscillations over a large parameter space as well as display a dynamic death regime at low flow rates. Inset in **(F)** shows simulation results plotted with a logarithmic x-axis to highlight the dynamic death regime in the IFFL model. We added noise to single cells in the population simulations as detailed in the **Methods**. A gray shaded background highlights experimental data. A green shaded background indicates models that reproduce the experimental observations.

sible only when external cAMP concentrations are restricted to a narrow dynamic range where the receptors are not saturated. Second, in the region where the external flow rate is extremely low, the population oscillations die off at all but the highest cell densities, due to a phenomenon known as "dynamic death" (Figure 2·4A, 1 mL/min Flow Rate). Past theoretical modeling efforts suggest dynamic death exists because external medium dynamics are too slow to catch up with the faster internal cAMP dynamics [76, 77]. In model simulations, only the IPNFB and IFFL models recapture this experimental observation (Figure 2·4E and inset in F).

Two major studies of population oscillations in *Dictyostelium* suggest a major role for noise in initiating and maintaining population oscillations [62, 63]. For this reason, we assessed how including noise alters population-level oscillations in each model by constructing stochastic generalizations of models without noise (Figure A·1). Simulation results show that for the Receptor Desensitization, CDINFB, and IFFL models, including noise in the single cell networks leads to a more gradual transition between no population-wide oscillations and collective oscillations but no other qualitative changes in behavior (Figure A·1B, C, F). Both the Phase Oscillator and IPNFB models, which were designed with stochasticity, display a change in behavior without noise. In the Phase Oscillator model, both in the original study and in this new analysis, noise aids in the initiation of

population oscillations by lowering the critical (lowest) cell density that allows for the oscillations (Figure A·1D) [62]. However, in the IPNFB model, noise is required for initiating and coordinating population oscillations because the removal of noise completely disables population-wide oscillations (Figure A·1E), suggesting noise is critical for driving population behaviors in the IPNFB model [63].

Single-Cell Behaviors

I. Single cells bifurcate from adaptive spiking to sustained oscillations in response to external cAMP step input

One of the most prominent experimentally-observed behaviors in isolated single *Dictyostelium* cells is that a small step change in external cAMP concentrations results in a large, sudden increase of internal cAMP concentration, which then returns back to near-baseline levels [63, 62]. This response has been termed an adaptive spike as it is reminiscent of similar phenomena in neural systems (Figure 2·5A). Experiments further show that if even higher levels of external cAMP are applied, single cells abruptly switch their response from producing an adaptive spike to an adaptive spike followed by sustained oscillatory behavior where internal cAMP concentrations oscillate in time even though external cAMP concentrations are constant (Figure 2·5B) [63]. These experiments suggest that external cAMP concentrations serve as a "bifurcation parameter" that drives the *Dictyostelium* signaling networks across a bifurcation from an excitable to an oscillatory regime.

To identify which network architectures could reproduce the key experimental observations, we ran simulations to check if the models produced: (1) single, excitable spikes after a low-level external cAMP step input and (2) a spike followed by a bifurcation to oscillations after a high-level cAMP step input. The Receptor Desensitization model, the IPNFB model, and the IFFL model produce canonical adaptive spikes where internal cAMP levels return back to near-baseline levels after a large response (Figure 2·5C). In contrast, the CDINFB model produces a large spike in response to a small input but fails to return back

to near-baseline levels, and the Phase Oscillator model fails to show any sort of adaptive spiking dynamics (Figure 2·5C). For this reason, for the remainder of the single cell phenomena tests beyond exploring the response to a large step input of external cAMP, we focus on the three models that produced adaptive spiking, as this is critical for all single-cell level phenomena. Further simulation results on the other models are in the Appendix A.

Next, we simulated single cell responses to large step inputs of external cAMP, with a specific interest in whether or not the the three models that show adaptive spikes also show a bifurcation to oscillatory behavior at high levels of external cAMP. The height of this large step input was chosen to be 10^4 times the low concentration based on experimental observations in Sgro, et al. that show robust oscillations at 10 μM external cAMP [63]. Only the IPNFB network displayed the bifurcation from excitable adaptive spiking to sustained oscillations (Figure 2·5D). The bifurcation to oscillations in the IPNFB model proceeds through a standard supercritical Hopf bifurcation based on a negative feedback loop with a time delay [78, 79]. Mechanistically, the origin of these oscillations is that the activator must build up to a sufficiently high level to activate the inhibitor, which then turns off activator production. The other two models lack either negative feedback (IFFL model) or a time delay (receptor desensitization only depends on instantaneous cAMP levels), accounting for the lack of single cell oscillations (Figure 2·5D). However, as discussed above, these later models can still support sustained population-level oscillations as the population-level oscillations originate from synchronized adaptive spikes in single cells.

II. Fold-change detection of external cAMP levels

During development, robust collective cAMP oscillations are observed from approximately 4 hours until as late as 20 hours post-starvation [62]. During this process, external cAMP levels vary dramatically because of changes in cell density due to cell migration. Single cells must robustly respond to this constantly changing and noisy external signal.

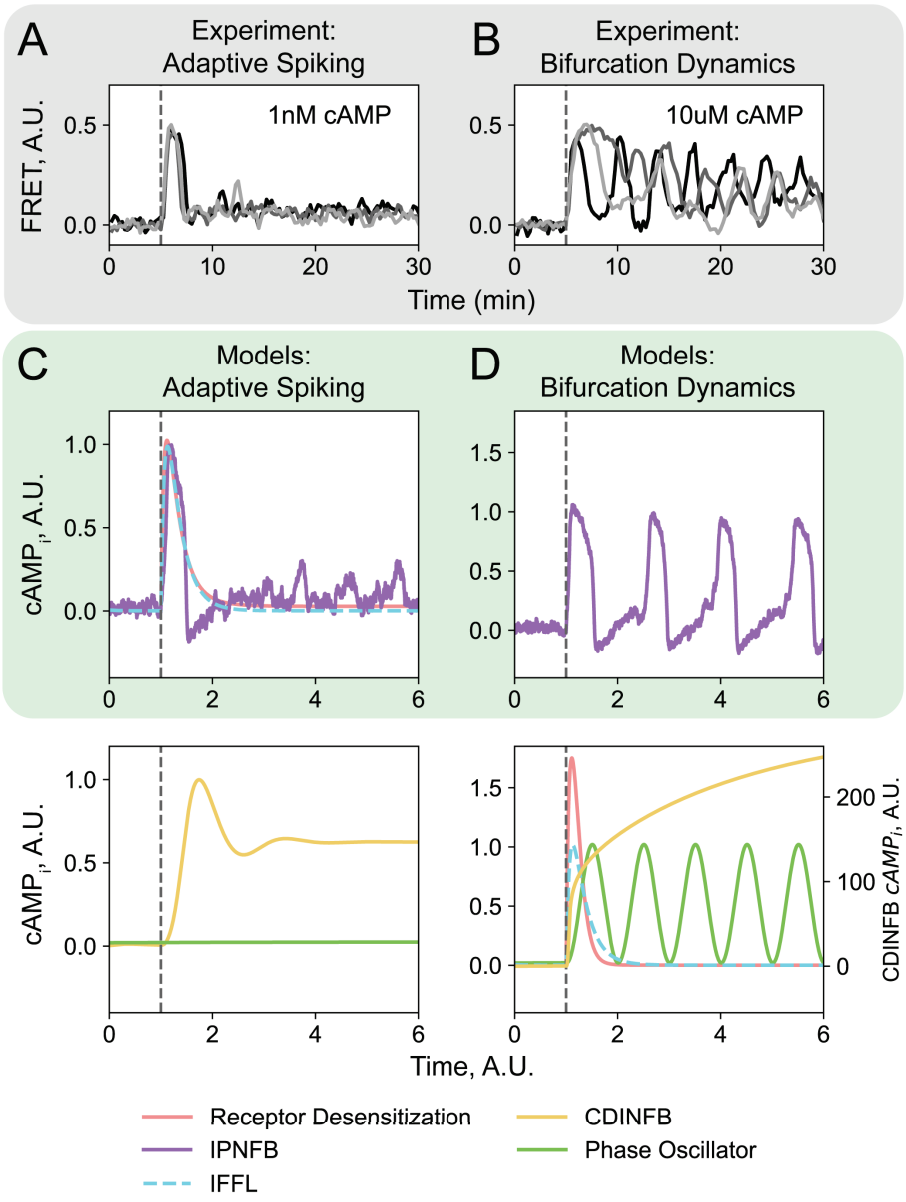

Figure 2·5: Evaluating models against single cell phenomena: cells bifurcate from adaptive spiking to sustained oscillations in response to external cAMP step input.

(A and B) Experimental data shows single *Dictyostelium* cells display a bifurcation in response to an external cAMP concentration step input, from adaptive spiking **(A)** to sustained oscillations **(B)** (n = 3 example cells per condition). Data is adapted from Sgro, et al. [63]. **(C and D)** Model simulations with low and high external cAMP step inputs show that only the IPNFB model recapitulates both behaviors, with the green-shaded upper panels displaying models that recapitulate the experimental observations, specifically the adaptive spiking behavior **(C)** and the bifurcation to sustained oscillations **(D)** and the lower panels showing models that do not recapitulate these phenomena. In both the experimental data and model results, external cAMP is applied at the gray dashed line.

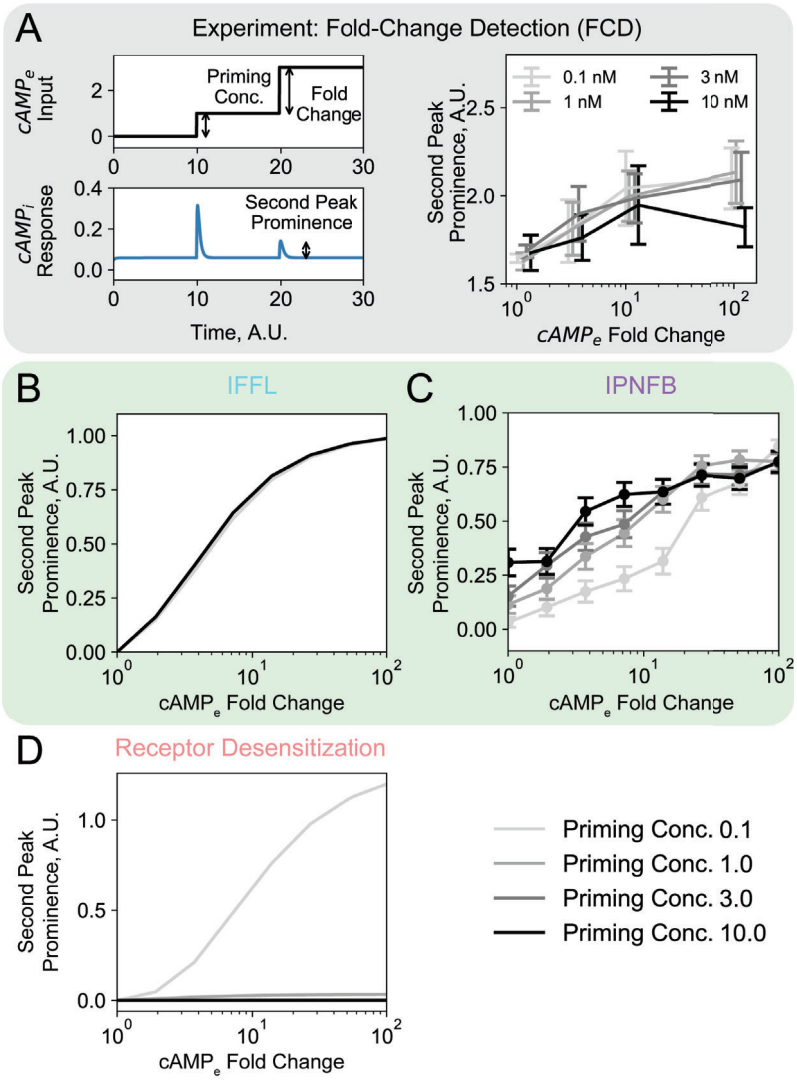

Figure 2·6: Evaluating models against single cell phenomena: cells are sensitive to fold changes in external cAMP levels.

(A) Experimental data shows *Dictyostelium* cells conduct fold-change detection. Left panel: diagram depicting how fold-change detection is quantified in both experimental and simulation data. Cells experience two consecutive external cAMP step inputs, with the first step height being the "Priming Concentration" and the fold change of the second step height over the first step height being the "Fold Change". The height of the internal cAMP spike in response to the second step input is quantified as "Second Peak Prominence" throughout the figure. Right panel: experimental data adapted from Kamino, et al. [74] shows single cells exhibit fold-change detection. **(B - D)** Simulation of different model responses shows that only the IPNFB and IFFL models qualitatively reproduce fold-change detection **(B and C)**. The IFFL traces representing different priming concentrations collapse on a single line in **(B)**. To account for single-cell noise in the IPNFB model, we ran 50 simulations for each priming concentration-fold change pair and display the mean and standard error of the mean from the simulations in **(C)**. The Receptor Desensitization model response traces to 3 and 10 unit priming concentrations collapse on a single line **(D)**. In simulations the one unit priming concentration is set to match the "low" $cAMP_e$ input level in Figure 2·5. A gray shaded background highlights experimental data. A green shaded background indicates models that reproduce the experimental observations.

Recent experiments show that single *Dictyostelium* cells conduct fold-change detection [74]: the response of single cells is determined only by the relative change in input signal (i.e. the ratio of the final cAMP concentration to the initial cAMP concentration), rather than absolute changes (Figure 2·6A). An important feature of fold-change detection is that it allows cells to operate in similar ways across a wide range of background cAMP concentrations [80]. This suggests that fold-change detection may underlie the ability of the *Dictyostelium* signaling networks to function in spatially and temporally heterogeneous environments during the development process.

To measure fold-change detection capabilities in the three models that reproduce single-cell adaptive spikes, we ran simulations that mimic the experimental design of Kamino, et al. where cells were subject to two consecutive step changes in external cAMP at different concentrations (the priming concentration and the secondary concentration, see Figure 2·6A) [74]. As in the experimental work, fold-change detection was measured by the prominence of the second adaptive spike and we scanned model responses to initial priming concentrations of 0.1 external units through 10 external units of cAMP. For a network that performs perfect fold-change detection, we expect the response curves for different priming

concentrations to collapse on a single line, a phenomenon observed in experiments (Figure 2·6A). The model with the best fold-change detection capabilities is the IFFL model which shows nearly perfect, deterministic fold-change detection over almost two orders of magnitude changes in external cAMP levels (Figure 2·6B). The IPNFB model, which is built with noise, also displays approximate fold-change detection (Figure 2·6C). In contrast, the Receptor Desensitization model does not exhibit fold-change detection (Figure 2·6D).

Interestingly, the IFFL and the IPNFB models achieve fold-change detection through two very different mechanisms. In the IFFL model, the response to fold-differences with different step heights is identical [74]. In contrast, the IPNFB model achieves only approximate fold-change detection through a combination of logarithmic-sensing and stochasticity-mediated modulation of the single cell firing rate (see Figure 2·6C) and Figure A·2).

Relating Network Architecture to Collective Behaviors

Our unified simulation framework allows us to identify the key components and network features needed to reproduce specific experimental observations (Figure 2·7). The analyzed models include disparate design features such as negative and positive feedback control, logarithmic environmental sensing, incoherent feedforward loops, and modeling single cells as phase oscillators. Nonetheless, there are some common themes that emerge from our analysis.

First, we find that negative feedback or feedforward motifs appear to be especially critical to produce excitability (i.e. adaptive spiking) at the single-cell level. These two features appear in all of the models except the Phase Oscillator model, the only model that fails to reproduce adaptive spiking on the single-cell level. This suggests that negative feedback or incoherent feedforward motifs drive single-cell excitability, consistent with past theoretical findings that negative feedback and incoherent feedforward loops are the core topologies that drive adaptive spikes [81]. Similarly, all of the models other than the Phase Oscillator model reproduce the observation that background cAMP inhibits collective oscillations,

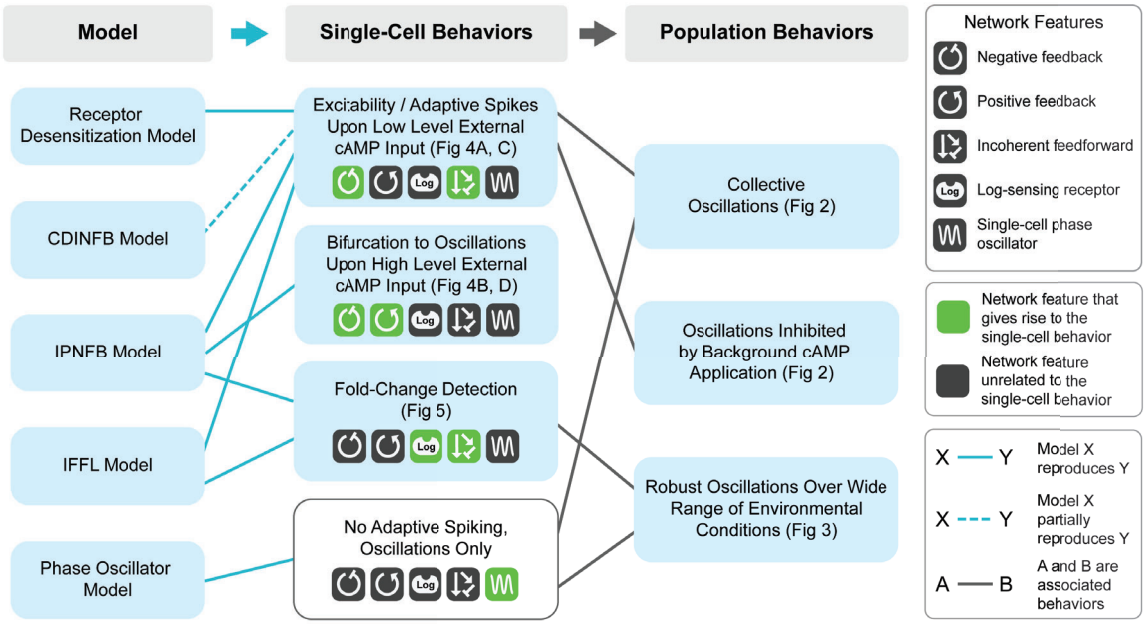

Figure 2.7: Graphical summary of our analysis reveals which network features give rise to single-cell and population-level experimental behaviors. All models except the Phase Oscillator model partially or fully reproduce at least one of the experimentally-observed single cell behaviors. These single-cell behaviors are driven by different network features in the models, suggesting there are multiple ways cellular signaling network architectures can generate these behaviors. Furthermore, several of the single-cell behaviors are associated with population-level behaviors, suggesting that the network features underlying the associated single-cell behaviors are critical for driving the associated population-level behaviors.

suggesting single-cell excitability may be the driving mechanism for this behavior.

Another key design feature that seems to be important for coordinating *Dictyostelium* behavior is positive feedback control. Positive feedback is a key element of the IPNFB model, the only model of the five we analyzed that can completely recapitulate all experimental observations at the single-cell level. The idea that positive feedback control might facilitate the single-cell bifurcation to oscillations is again consistent with past theoretical work demonstrating that interlocking positive-negative feedback loops give rise to more robust and reliable oscillatory behaviors [82].

We also found that both incoherent feedforward loops – present in the IFFL model – and logarithmic sensing – present in IPNFB model – enable fold-change detection [83,

84]. This observation, along with the fact that only these two models reproduce this phenomenon, suggests that one of these design features is necessary to drive fold-change detection in this context.

Finally, we find that in order to have robust population-level oscillations that persist despite environmental variations, single cells must either perform fold-change detection or behave as a phase oscillator. Given the inability of phase-oscillator models to recapitulate single-cell behavior, our analysis suggests that cells likely implement fold-change detection in order to coordinate population behaviors.

2.4 Discussion

Many different properties of single cells and cellular populations have been proposed to be conceptually important for coordinating collective oscillations in multicellular systems, including *Dictyostelium*. Here, we exploited the stereotypical spiking behavior displayed by single *Dictyostelium* cells to normalize models and directly compare them to each other, as well as to experimental observations. Our results show two types of networks fully describe the population-level behaviors: the IPNFB with a logarithmic pre-processing module and the Incoherent Feedforward Loop (IFFL) (Table 2.1). These networks both display two key single-cell level design features that are critical for coordinating the observed population-wide dynamics: excitable single-cell level dynamics and fold-change detection (Table 2.1, Figure 2·7). Furthermore, only the IPNFB model reproduces all of the observed single-cell and population-level behaviors. This suggests that while both networks are potential pathways for the design of collective oscillatory systems, the IPNFB model more accurately reflects the specific *Dictyostelium* signaling network. Through our analysis, we find that the observed population-level phenomena can be driven by a key single cell network design principle: excitable dynamics that respond to relative changes in external signals.

Excitability is a critical single-cell network design feature that drives collective oscil-

lations that are tunable by cell-cell coupling (Figure 2·7). Molecular networks that display excitable dynamics require two network features. The first feature is that the network includes either a negative feedback or incoherent feedforward motif that brings down the levels of or activities of the molecular species that are activated by external inputs [81]. Negative feedback and incoherent feedforward loops that drive single-cell excitability are found in the two models that succeed in recapitulating almost all experimental observations (Table 2.1). The second feature aiding excitable dynamics is timescale separation/time delay where after the increase of the activator species, the inhibitory interactions either respond on a slower timescale or have a built-in delay. This allows the input activation to dominate the early response before a strong inhibitory response begins, leading to an excitable spike in the activator species. In both example networks with superior performance, there is a time separation between the inhibitor species τ_I and the activator species τ_A facilitating excitability in the networks (see Figure A·5 for the effect of decreasing timescale separation). This timescale separation is naturally accompanied by refractoriness as is observed experimentally in single *Dictyostelium* cells (Table 2.1, Figure A·4). This refractoriness leads to unidirectional signal propagation in a population.

The second critical single-cell network design feature we identified is that internal dynamics must be dependent on the relative change of external signal as opposed to absolute concentrations, a feature known as fold-change detection (Figure 2·7). This feature coordinates robust population oscillations during development over a large range of environmental parameters such as large changes in cell density, varying ability to degrade external cAMP, and noisy fluctuations (Figure 2·4). Previous work has identified several major classes of fold-change detection-competent networks by conducting exhaustive scans of network topologies [83, 84]. These scans found that fold-change detection-competent models are extremely rare, and the two naturally occurring fold-change detection models, the incoherent type I feedforward loop (I1FFL) and the non-linear integral feedback loop

(NLIFL), are among the simplest networks suggested to achieve optimal response amplitude, speed, and noise-resistance. Another possible mechanism for achieving fold-change detection is logarithmic sensing at the receptor level which can theoretically be achieved with an allosteric protein [85]. The best-performing example networks from our analysis both fall into the canonical categories: one is an IFFL network and the other uses a logarithmic-sensing module (Figure 2·1 and 2·6). Although both networks display fold-change detection, we note there are subtle differences. With the IFFL model, the network tunes spike height in response to input fold change. The IPNFB model, however, modulates the probability of spikes in individual cells in response to input fold-change (Figure A·2), tuning the average response of a group of cells and thus displaying fold-change detection at the population level.

Additionally, our work also further reinforces previous findings that stochastic noise in the single cell network potentially plays a role in coordinating population behaviors. Previous studies on bacterial competence suggest that noise combined with an excitable module can explain both the initiation of and escape from the competent state, and that noise levels modulate the percentage of cells entering into and exiting from the competent state in bacterial communities [86, 87]. In *Dictyostelium*, work on the cAMP signaling and chemotaxis networks suggests that noise in network components with both positive and negative feedback loops plays a vital role in coordinating network dynamics [88, 63]. In our analysis, in the model that most accurately recapitulates behaviors in *Dictyostelium*, noise is crucial for fold-change detection and coordinating population oscillations (Table 2.1, Figure A·1). Stochasticity could provide a mechanism for initiating and maintaining population-wide oscillations without requiring specialized cells such as pacemaker cells for robustly coordinating the population, allowing for decentralized control. To answer whether and how noise modulates population-wide behaviors, better experimental techniques and longer timescale experiments that quantify noise-driven phenomena and modulate potential sources of noise

are required. Taken together, our analysis suggests that excitability that is insensitive to absolute environmental signals acts as a key network design feature that allows for efficient oscillations coordination in *Dictyostelium* populations, and noise in signaling networks plays a role in population-behavior modulation.

Coordinated population behaviors not only require specific features in single-cell signaling networks but also require coupling between cells. When the cells are coupled through the external medium, the timescales of the internal and external signal dynamics need to be effectively coupled. In the case of *Dictyostelium* populations, the time scale of the external signal dynamics is modulated by cAMP degradation and this rate is determined by phosphodiesterase concentrations and kinetics. At extremely high cAMP degradation rates, single cells cannot effectively communicate. By contrast, if the degradation rates are too low, the dynamics of the medium are too slow to follow the internal dynamics, leading to desynchronization of single cells, or “dynamic death" [76, 77], a phenomenon experimentally observed in Gregor, et al. and Sgro, et al. [62, 63]. In our analysis, the IPNFB and IFFL models reproduce the dynamics death phase, suggesting that cells match the timescales governing internal signaling networks and external signal propagation. Such timescale coordination may also be crucial for chemotaxis in *Dictyostelium* cells [89].

While all of the models investigated here take a mean-field approach – neglecting space and time for signal propagation between cells – in reality signals propagate through the population and create complex spatiotemporal patterns such as concentric waves and rotating spirals [61]. Traveling waves are a natural analog of the kind of coherent population-level oscillations discussed in this work and may represent an important design principle for coordinating behavior across large spatial reasons. In support of this idea, we note that waves are also observed during development, where mouse embryonic cells use excitable internal YAP dynamics that are coupled by Notch signaling to achieve long-range oscillatory waves for vertebrate segmentation [90], and *Drosophila* embryos use propagating Cdk1 waves to

synchronize cell cycles across large spatial scales [91]. In synthetic biology, engineered negative and positive feedback motifs can achieve excitability and robust waves across a large bacterial population when coupled through diffusible molecules [92, 93].

Altogether, this work identifies excitability and fold-change detection as key design features of internal signaling networks that allow for robust coordination of population-wide oscillations in heterogeneous ill-defined environments. These network features found in *Dictyostelium* are widely shared in natural and synthetic cell populations that display collective oscillatory behaviors, suggesting these network features could be a common control mechanism used by biological systems to coordinate signal transduction in multicellular contexts. These features enable many desirable behaviors for multicellular populations including coordination over orders of magnitude differences in population size, environmental insensitivity to small fluctuations, and fast, unidirectional long-range signal propagation. Our work suggests that there are relatively few signaling network design motifs that can robustly coordinate emergent multi-scale behaviors in biological systems.

2.5 Methods

Model equations were adapted from the literature [71, 73, 62, 63, 74], and the mathematical expressions and parameters for each model are detailed in the Appendix A. All simulations were solved by the Euler-Maruyama method. Time step sizes were empirically chosen to make sure simulation outputs are reliable such that decreased time step sizes would not produce alternative results. Exploring the emergence of population oscillations and their dependence on cell-cell coupling (Figure 2·4) requires investigating a wide range of parameter space and thus smaller time step sizes were taken to make sure the simulation outputs are reproducible. Models were normalized to one another as described in the *Results* section.

Noise in single-cell networks was added as a Langevin noise term $\eta(t)$ to the end

of the equation representing the internal “activator" component. The noise term satisfies $<\eta(t)\eta(t')>=\sigma^2\delta(t-t')$, with σ^2 denotes the noise strength. The noise strength in each model was chosen either from the original literature for models with noise in the original implementations, specifically the Phase Oscillator model and IPNFB model, or arbitrarily determined such that noise allows for a slight quantitative change in the phase diagram describing the emergence of population oscillations but not a qualitative change (Figure A·1). The respective noise strengths in the Receptor Desensitization model, CDINFB model, Phenomenological Phase Oscillator model, IPNFB model, and IFFL model were set to 10, 0.1, 0.02, 0.15, 0.01.

Code Availability Experimental data and Python code for all simulations are available on GitHub at https://github.com/sgrolab/dictymodels.

Behaviors/Models		Receptor Desensitization	Coupled Direct and Indirect Negative Feedback (CDINFB)	Phase Oscillator	Interlocking Positive-Negative Feedback (IPNFB)	Incoherent Feedforward Loop (IFFL)
Population	Background cAMP inhibits oscillations (Fig 2·3)	✓	✓	✗	✓	✓
	Robust oscillations over wide range of environmental conditions (Fig 2·4)	✗	✓	✓	✓	✓
	Dynamic death reproduced at low flow rates (Fig 2·4)	✗	✗	✗	✓	✓
	Noise-driven oscillations (Fig A·1)	✗	✗	✗	✓	✗
Single Cell	Excitability/fully adaptive spiking (Fig 2·5)	✓	✗	✗	✓	✓
	Bifurcation from adaptive spiking to oscillations (Fig2·5)	✗	✗	✗	✓	✗
	Fold-change detection (Fig 2·6)	✗	N/A	N/A	✓	✓
	Sensitivity to cAMP input dynamics (Fig A·3)	✗	✗	N/A	✓	✗
	Entrainable to repetitive stimuli and has refractory period (Fig A·4)	✓	✓	N/A	✓	✓

Table 2.1: Population and single-cell behaviors evaluated in different models. Green check marks indicate if the model successfully reproduces the specific experimental behavior. X marks indicate the model is unable to reproduce the experimental behavior. N/A (not applicable) indicates the experimental comparison cannot be made because the model either fails to produce single-cell adaptive spikes (as for the Phase Oscillator model) or only shows partial adaptation (as for the CDINFB model).

Chapter 3

Transient activation of intracellular cAMP modulates migration and induces actin cytoskeleton reorganization through calcium signaling

3.1 Introduction

In **Chapter 2**, theoretical modeling was used to investigate the essential features of the single-cell signaling networks that drive group-wide synchronous oscillations in the cellular slime mold. The extensive theoretical investigation is enabled by experimental measurements of the dynamic changes of the signaling molecules within individual cells. However, for many biological systems and processes, such data have not yet become available because of a lack of tools to measure and modulate the activity of the signaling molecules with high spatial-temporal precision. With recent advances in molecular sensors, optogenetic tools, and imaging, it has become possible to experimentally investigate the input-signaling-cellular outputs relations. Here in **Chapter 3**, new techniques that manipulate and measure the signaling molecule cAMP were used to investigate how this signaling molecule alters behavioral outputs related to migration in mammalian fibroblast cells.

Cell migration is a ubiquitous behavior that is essential for biological processes like tissue development, wound healing, immuno-response, and cancer metastasis. Mesenchymal migration, or crawling migration, is a major mode of cell migration that is observed in a wide range of cell types including embryonic stem cells, fibroblasts, keratinocytes, and

numerous cancer cells (reviewed in for example [21, 94, 95]). Mesenchymal migration starts by establishing cell polarity with a front and a rear side. The front side of the cell is characterized by extended dynamic protrusions that are driven by actin polymerization. At the same time, new adhesion sites, protein complexes termed focal adhesions (FAs), are formed and stabilized between the cell membrane and the substrate. The rear side of the cell is characterized by thick actin fibers that can generate high contractility and disassembly of the focal adhesions, both of which facilitate rear retraction and cell body movement. Cell migration requires coordination of the cytoskeleton structure as well as tension regulation [96], both of which are regulated by numerous signaling molecules such as focal adhesion kinase (FAK), Rho-GTPases, and calcium [21, 94, 95].

A key signal regulator of migration is the cyclic adenosine monophosphate/protein Kinase A (cAMP/PKA) pathway [97, 98]. Its important regulatory roles on migration have been shown in multiple cell types including epithelial cells [99], endothelial cells [100], neuronal cells [101], and fibroblasts [102, 103]. It is believed that the cAMP/PKA pathway affects migration mostly through modulating downstream signaling targets which then regulate focal adhesion assembly, actin polymerization, and contractility (extensively reviewed in [97, 98]).

Despite decades of experimental effort investigating how the cAMP/PKA pathway regulates migration, the observations have been paradoxical. In particular, literature has shown that either inhibition or hyper-activation of the pathway can lead to decreased migration (reviewed in [97, 98]). These observations suggest that proper spatial and/or temporal control of the cAMP pathway is essential for migration modulation. A previous study measuring static PKA activity at the protrusions suggests PKA is specifically activated at the protrusions and is essential for chemotactic migration [103]. More recent studies measured PKA dynamics using reporters that are localized at the cell membrane and sugge st membrane-localized PKA is essential for dynamic protrusion regulation [99, 104]. These studies have

shown that spatiotemporal control of the cAMP pathway is important for cell migration.

However, existing studies are mostly based on pharmaceutical or genetic perturbations that alter the steady state of this signaling pathway. Additionally, these perturbation strategies suffer from nonspecific effects on other signaling pathways (e.g. a widely-used PKA inhibitor H89 has multiple other kinase targets [105]) and/or changes in cell state, potentially confounding the results. Additionally, it is still unclear how temporal, global control of the cAMP/PKA pathway affects cellular behaviors related to migration. Here, we harness an optogenetic tool bPac [106] - a bacteria-derived adenyl cyclase that produces cAMP upon exposure to blue light - to understand how this pathway regulates migration by directly controlling cAMP dynamics in cells. This tool's minimal dark activity, high sensitivity, and fast on-and-off kinetics enable us to modulate cAMP/PKA activity at the minute timescale. With this tool, we achieved reproducible and tunable activation of the cAMP pathway. We observed inhibited migration in both 3T3 fibroblast and MDCK epithelial cell lines upon direct, repetitive activation of the cAMP pathway, with the extent of inhibition depending on the strength of pathway activation. Further, we found that this inhibitory effect is possibly due to decreased cell contractility as a result of the drastic reorganization of the actin cytoskeleton structure induced by transient cAMP pathway activation. Lastly, we found that the actin cytoskeleton reorganization is mediated by calcium signaling.

3.2 Results

3.2.1 bPac achieves temporal control of PKA activity with tunable duration and amplitude

To achieve direct, tunable control of the cAMP pathway, a tool needs to fulfill several major requirements. The tool needs to have minimal off-target effects, display little or no basal activity when turned off, be able to be activated reproducibly multiple times, be able to be activated and deactivated on a physiologically-relevant time scale, and achieve tunable

control of the cAMP pathway.

To meet these requirements, we chose to use the light-activated adenylyl cyclase, bPac, originally found in bacteria [106]. This enzyme is orthogonal to those found in mammalian cells, produces cAMP upon exposure to blue light, and has extremely low dark activity. To confirm tool expression and measure expression level, we fused the optogenetic tool to a mTurqoise2 fluorescent protein.

We first validated whether bPac can achieve repetitive activation of the cAMP/PKA pathway in a mammalian fibroblast cell line (NIH 3T3) by co-expressing the bPac construct and a reporter for the direct downstream effector of cAMP, protein kinase A (PKA) (Fig 3·1A). Because bPac activates in response to light with a spectra range below 500nm [106], we chose to use a PKA reporter that consists of orange and far-red fluorescent proteins, PKA-Booster [107] such that imaging the reporter signal would not activate bPac. The PKA-Booster reporter is based on Förster Resonance Energy Transfer (FRET) between the two fluorescent proteins, the FRET donor protein mKOκ, and the FRET acceptor protein mKate2. The donor and acceptor proteins flank a PKA substrate peptide and an FHA1 domain which binds to the peptide when the substrate is phosphorylated by PKA. Upon bPac activation, cAMP activates PKA which then phosphorylates the substrate in the reporter. After phosphorylation, the reporter changes conformation and brings the two fluorescent proteins closer, leading to FRET efficiency increase.

We first validated the reporter by treatment with forskolin, a drug that activates endogenous adenylyl cyclases through G protein-coupled receptors (GPCRs) [108]. FRET signal from cells expressing the PKA-Booster reporter increased immediately upon forskolin treatment (Fig B·1), confirming the reporter worked as expected. We then went on to validate and characterize the bPac tool with the PKA-Booster reporter in 3T3 fibroblast cells. By monitoring PKA activity with the PKA-Booster reporter while stimulating bPac with a blue-colored laser, we observed activation of PKA in multiple cycles with reproducible

dynamics, which is absent in control cells that did not express the bPac construct (Fig 3·1 A-B). The bPac tool activated PKA rapidly upon light stimulation, showing that the tool has a fast on rate. The off dynamics are comparably slower, which was likely determined by the concentration and kinetics of phosphodiesterases (PDEs) that degrade cAMP, and the activity of phosphatases that hydrolyze the phospho-groups on the reporter substrates. In summary, we have shown that in fibroblasts, expression of the bPac optogenetic construct achieves repetitive, reproducible activation of the cAMP/PKA pathway, and has relatively fast on and off rates.

To test whether we can modulate the extent of cAMP/ PKA pathway activation with the bPac optogenetic tool, we applied different intensities and durations of blue light (i.e. light dosages) to cells using the programmable Optoplate system [109], and quantified the response height and width of the resulting PKA reporter signal. We found that either increasing stimulation light intensity or duration increased the height and width of the PKA activation response (Fig 3·1 C-D). We note that at intensities above 1000 (A.U.) and time durations longer than 30 seconds, the amount of cAMP produced in cells saturated the range of the sensor, shown as a flat peak sensor response (Fig B·2). However, at this amplitude saturation regime, there is still tuning of the PKA response width, suggesting that bPac activation at those regimes remains tunable. Lastly, we asked whether the pathway activation response is dominated by the expression level of this optogenetic construct. There is no strong correlation between the expression level of the bPac construct (as is shown by the mTurquoise2/CFP channel intensity) and the response width or height from the PKA sensor (Figure B·3), suggesting that the different extent of PKA activation is dominated by stimulation profiles (length and intensity). To summarize, our data shows the bPac optogenetic tool is able to achieve robust, reproducible, and quick activation of the downstream effector PKA in a tunable manner.

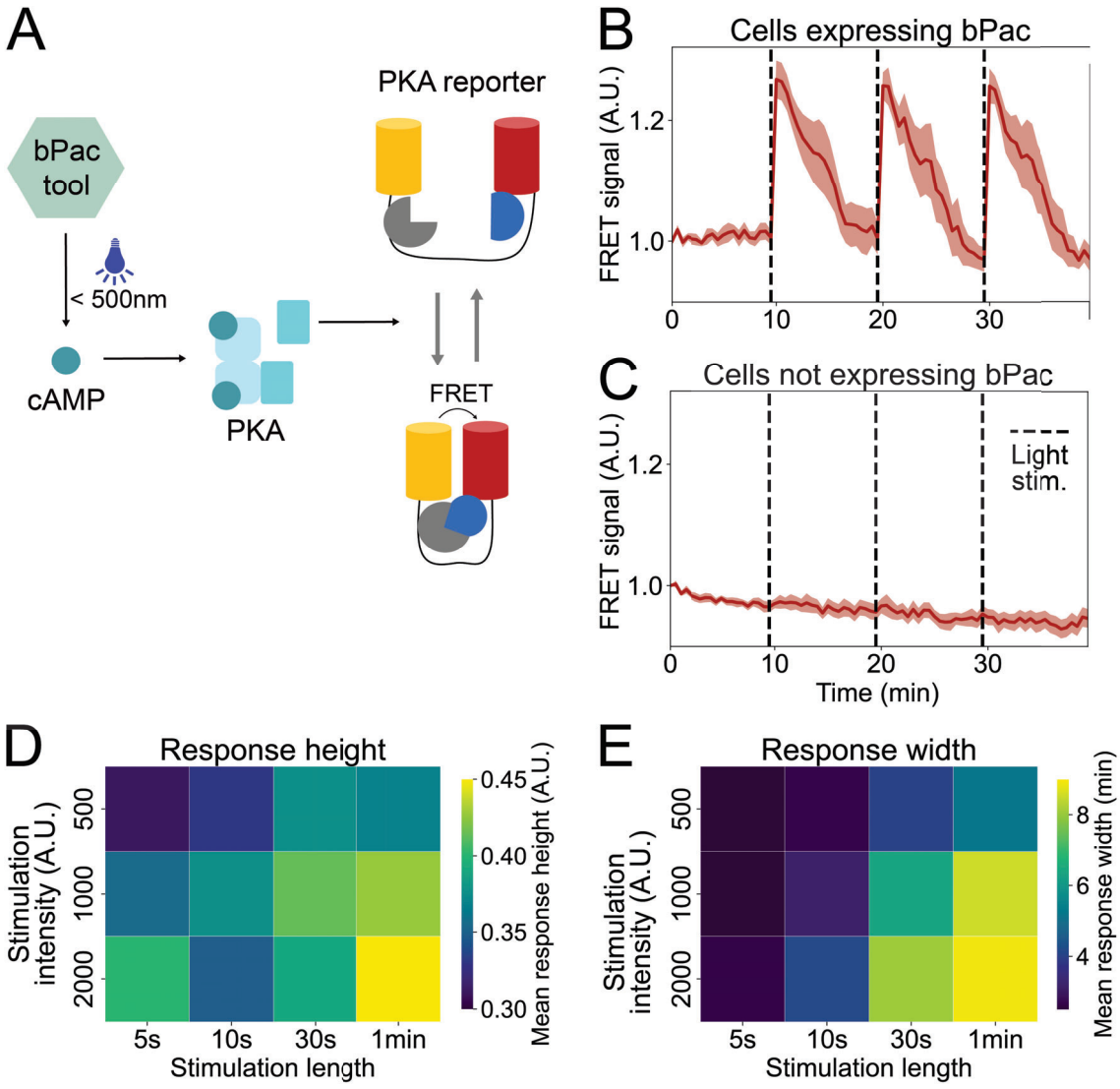

Figure 3·1: bPac construct validation and characterization in 3T3 fibroblast cells.

(**A**). Graphical demonstration of the bPac optogenetic tool validation experiments. Upon light stimulation (wavelength below 500nm), the bPac tool produces cAMP, activating the downstream PKA whose activity is read out by the PKA-Booster FRET reporter. (**B**)-(**C**). FRET signal traces measured by the PKA-Booster sensor are shown in cells that are expressing the bPac construct (bPac-mTurquoise2) in (**B**) or not expressing the bPac construct in (**C**). Traces are normalized to the baseline signal before stimulation and the mean and S.E.M. are shown. Light stimulation was turned on three times at the black dashed lines, with 445 nm laser at 25% power for 1 second. n = 7 cells for each condition (expressing or not expressing bPac) are included. (**D**) - (**E**). PKA-Booster reporter signal height (**D**) and width (half max height width, (**E**)) in response to different light stimulation duration and intensity, with heatmap colors corresponding to the mean from multiple cells. The signal traces are normalized to the baseline average before calculating the height and widths. For each photostimulation condition, n = 12 to 21 cells are included. Light stimulation was conducted using the 465 nm LED on the Optoplate system [109].

3.2.2 bPac activation inhibits 2D migration in a dose-dependent manner

To investigate whether and how cell migration is modulated by direct activation of the cAMP/PKA pathway, we used the classic two-dimensional scratch assay (for example, reviewed in [110, 111]). In addition to stably expressing the bPac optogenetic construct (bPac-mTurquoise2-NES), a red actin-labeling marker LifeAct-mScarlet(i) was also expressed to track gap closure over time without activating the optogenetic tool with bright-field light. To rule out the possibility that blue light exposure might affect migration, we included cells expressing the control construct (mTurqoise2-NES). For the bPac activation protocol, we picked the stimulation cycle length (every 5 minutes) to allow for sufficient degradation of cAMP after stimulation and to avoid potential toxicity from keeping intracellular cAMP at a constant high level.

We were able to generate accurate gap masks over time with custom-written analysis software and obtain gap areas as well as percentage gap closed measurements (Fig 3·2). As is shown in both the gap area and fraction closed, there was an initial lag immediately after gap creation followed by a regime where the gap area decreased at a constant rate before the gap completely closed (Fig 3·2C). We used the slope of the linear fit during the linear closure regime to quantify cell migration efficiency.

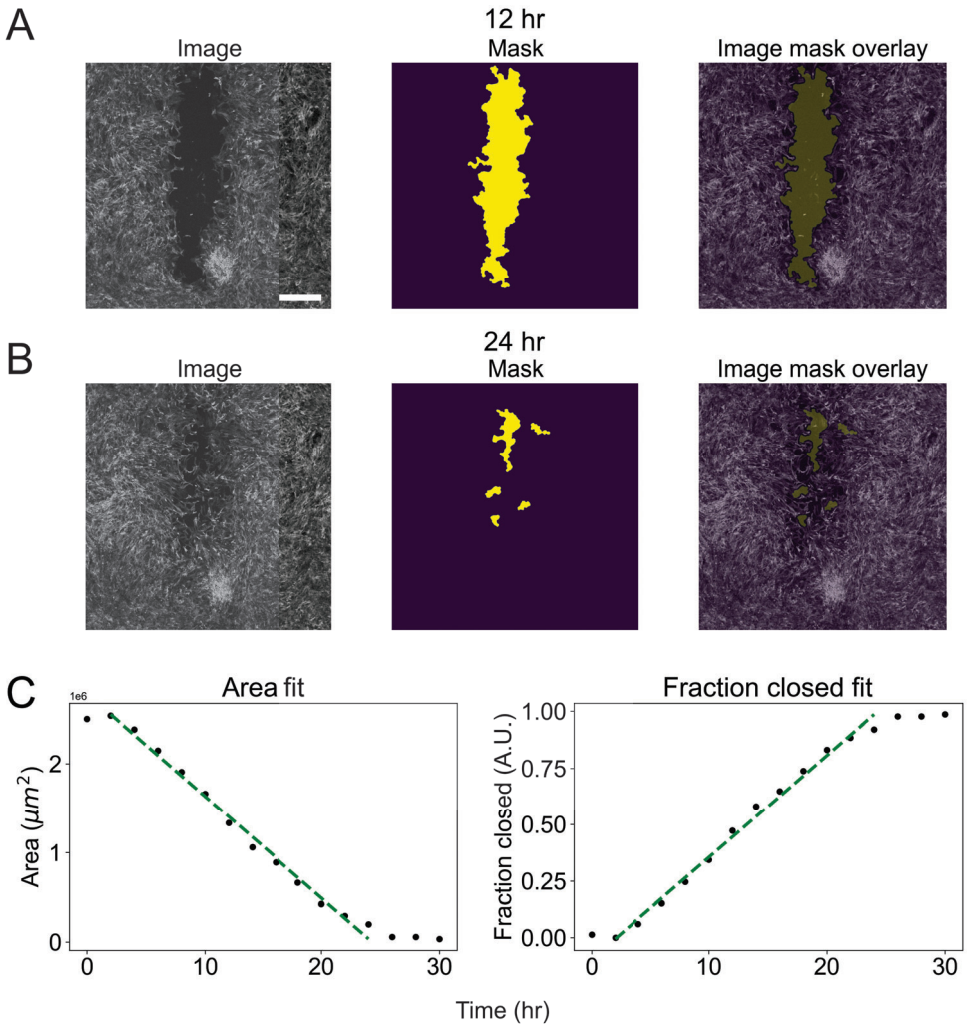

Figure 3·2: 2-dimensional gap detection and closure rate quantification.

Example outputs from the automatic gap detection pipeline at 12 hours (**A**) and 24 hours (**B**) after gap creation. In (**A**) and (**B**), the left panels show the raw fluorescent images of the LifeAct-mScarlet(i) marker, the middle panels show the binary masks generated, and the right panels show masks overlaid on the images. Scale bar = 500 μm. (**C**) shows the gap area change (left panel) and fraction area closed with regards to the initial gap area (right panel) over time. Black dots indicate the area or percentage closed at specific time points, and green dashed lines show linear fits between 2 to 24 hours after gap creation. Area closure rate and fraction closure rate are measured from the slope of the linear fitted lines (dashed green lines).

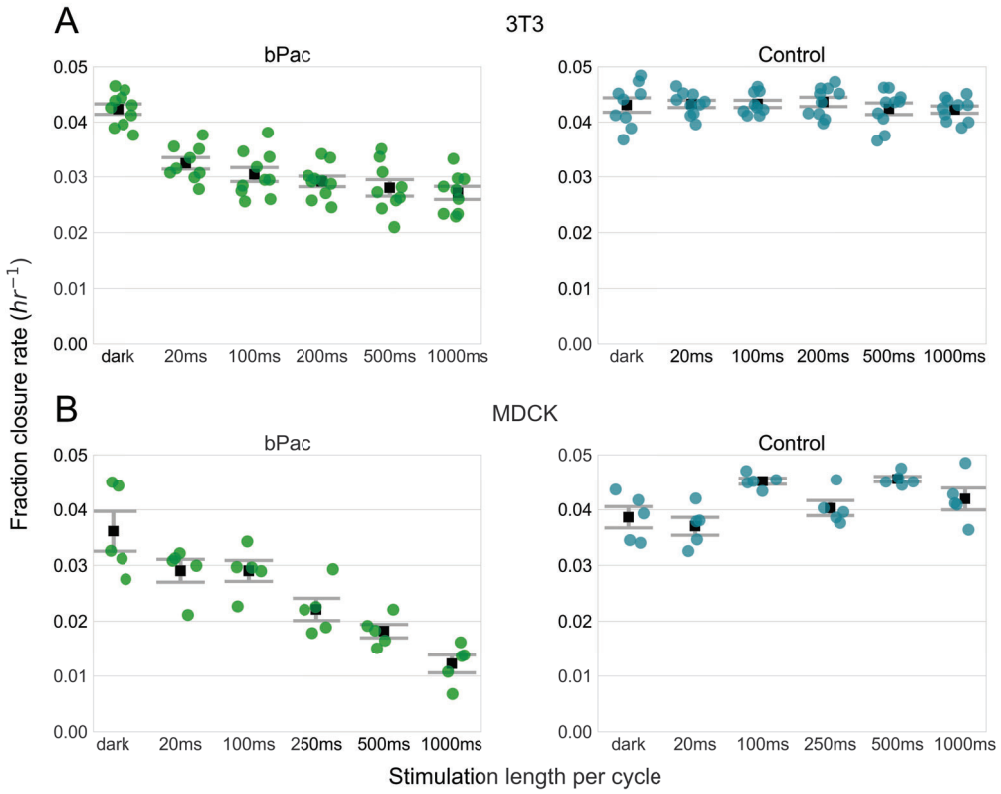

Figure 3·3: bPac activation inhibits two-dimensional cell migration in a dose-dependent manner in both 3T3 fibroblasts and MDCK cells. Fraction area closure rate was quantified with different light stimulation lengths (dark, light on for 20ms, 100ms, 200ms, 500ms and 1000ms every 5 minutes) in 3T3 fibroblasts (**A**) and MDCK cells (**B**). The left panels show the fraction closure rate with cells expressing the bPac optogenetic construct (bPac-mTurquoise2-NES) while the right panel shows that with cells expressing the control construct (mTurquoise2-NES). Each colored dot represents an independent experiment (well). Black square dots and gray bars represent mean and S.E.M. For (**A**) 9 to 10 wells are included for each stimulation length. In (**B**), 5 wells are included for each stimulation length.

We first checked whether expressing the bPac optogenetic construct would affect migration. Fraction closure rates without light stimulation (dark) are similar for cells expressing the bPac and the control construct (Fig 3·3) for both 3T3s and MDCKs, confirming stable expression of the bPac optogenetic construct has a neglectable influence on two-dimensional cell migration. In both cell types, increased bPac activation dosage (longer stimulation length per 5-minute cycle) led to a decrease in gap closure rate, whereas in

cells expressing the control construct, light stimulation did not affect the gap closure rate, ruling out the possibility that the decrease of migration efficacy was caused by exposure to blue light. In 3T3 fibroblasts, the inhibition effect from bPac stimulation saturated at around 200ms stimulation length, as increasing stimulation length beyond 200ms did not lead to a further decrease of closure rate (Fig 3·3A). This observation holds true even when the cells are exposed to up to 4000ms stimulation per 5-minute cycle (Fig B·4). This suggests that in 3T3 fibroblasts, either the downstream effectors of the cAMP pathway that are relevant in migration regulation are saturated beyond 200ms stimulation length, repetitive activation of the cAMP pathway leads to processes that compensate the inhibitory effect on migration, or the cells use mechanisms independent of the cAMP pathway to drive migration in this context. Interestingly, in MDCK cells, stronger bPac stimulation led to a stronger inhibitory effect on migration up to 1000ms stimulation length, with the highest stimulation dosage leading to a nearly 70% decrease in migration efficiency (Fig B·4). This suggests that properly-tuned cAMP pathway activity is essential for two-dimensional migration in this cell type.

One potential caveat in our assay is that because both cell lines actively divide, bPac activation could have a potential effect on cell proliferation which could contribute to the inhibition of gap closure rate [112, 113]. However, we observe differences in gap closure rate between different stimulation dosages as early as 3 to 4 hours after gap creation which is too early for proliferation modulation to happen. Therefore, bPac activation likely inhibits 2D migration regardless of whether it has any effect on proliferation. In summary, we have shown that transient, repetitive activation of the cAMP pathway with optogenetically-activated bPac inhibits 2D migration in both 3T3 fibroblast cells and MDCK epithelial cells, with the extent of inhibition related to the light stimulation dosage. In the following sections, we will focus on the 3T3 fibroblast cell culture model.

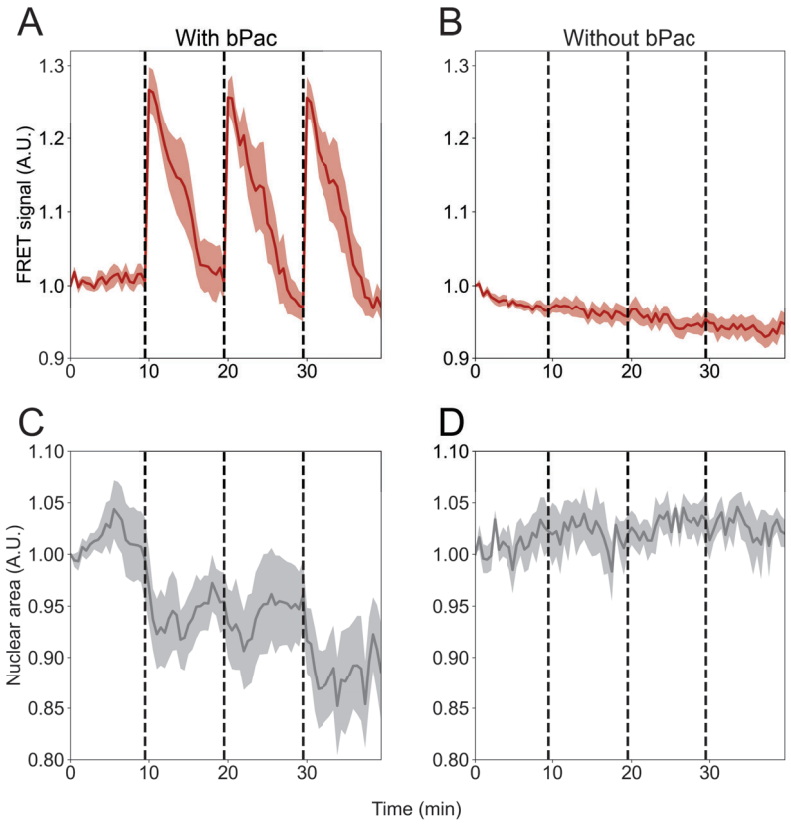

Figure 3·4: Activation of bPac led to changes in the nuclear area that is concurrent with PKA activity response. FRET signal traces measured by the PKA-Booster sensor are shown in cells expressing the bPac construct (bPac-mTurquoise2) in (**A**) or not expressing the bPac construct in (**B**), whereas nuclear areas in the same cells are quantified in (**C**)-(**D**). Traces are normalized to the pre-treatment values on a per-cell basis, and the mean and S.E.M. of traces are shown. Photostimulation was turned on three times at the black dashed lines, with 445 nm laser at 25% power for 1 second. n = 7 cells are included for each condition.

3.2.3 bPac activation induces cellular relaxation and disrupts the actin cytoskeleton

After establishing that bPac activation inhibits migration, we then investigated how this inhibition occurs. It has been shown that the cAMP/ PKA pathway modulates numerous downstream effectors that are closely related to migration, such as focal adhesion turnover, actin polymerization and cell contractility (reviewed in [97]). To investigate what mediates bPac-induced migration inhibition, we turned to an observation from the bPac validation

data (Fig B·1): upon bPac activation, the cell nucleus displayed a sudden, prominent, but reversible shape change. This shape change is reflected by the rapid decrease of nuclear area upon stimulation followed by a slower recovery, and its dynamics roughly match the dynamics of the measured PKA activity signal (Fig 3·4). Structurally, the nucleus is connected to the actin cytoskeleton fibers through the linker of nucleoskeleton and cytoskeleton (LINC) complex [114]. Additionally, it has been shown that nuclear shape is regulated by actin cytoskeleton contractility- the forces adhesive cells exert to the substrate that they reside on [115, 116]. Therefore, it is logical to hypothesize that the observed nuclear change upon bPac activation is driven by a change in the contractility of the cells.

To test this hypothesis, we measured cell contractility using traction force microscopy (TFM) [117, 118, 119]. In this assay, cells are seeded on elastic substrates containing fluorescent beads embedded close to the surface. When the cells change contractility, the traction force they exert on the surface changes, leading to the displacement of the beads. The displacement can then be tracked and correlated to the forces that cells exerted on the substrate. Upon blue light stimulation, cells expressing the bPac construct showed a rapid change in traction force (Δ traction force) that is partially reversed after the withdrawal of the stimulation (Fig 3·5 A-G). Because the cells are basally contracting the substrate, an outwards change in the Δ traction force field upon bPac activation (Fig 3·5 B) indicates relaxation of cell contractility. This behavior is not observed in cells expressing the control construct (Fig 3·5 D-H), confirming that the cell contractility decrease is not induced by blue light stimulation alone. The temporal profile of cellular relaxation also matched the fast on and slower off dynamics as is shown in both the nuclear deformation data and PKA response (Fig 3·4), suggesting that the cellular contractility change upon light stimulation is likely through the increase of intracellular cAMP upon bPac activation, and nuclear area change is at least partially mediated by change in cell contractility.

There are two major ways that cell contractility can be altered: through modulating

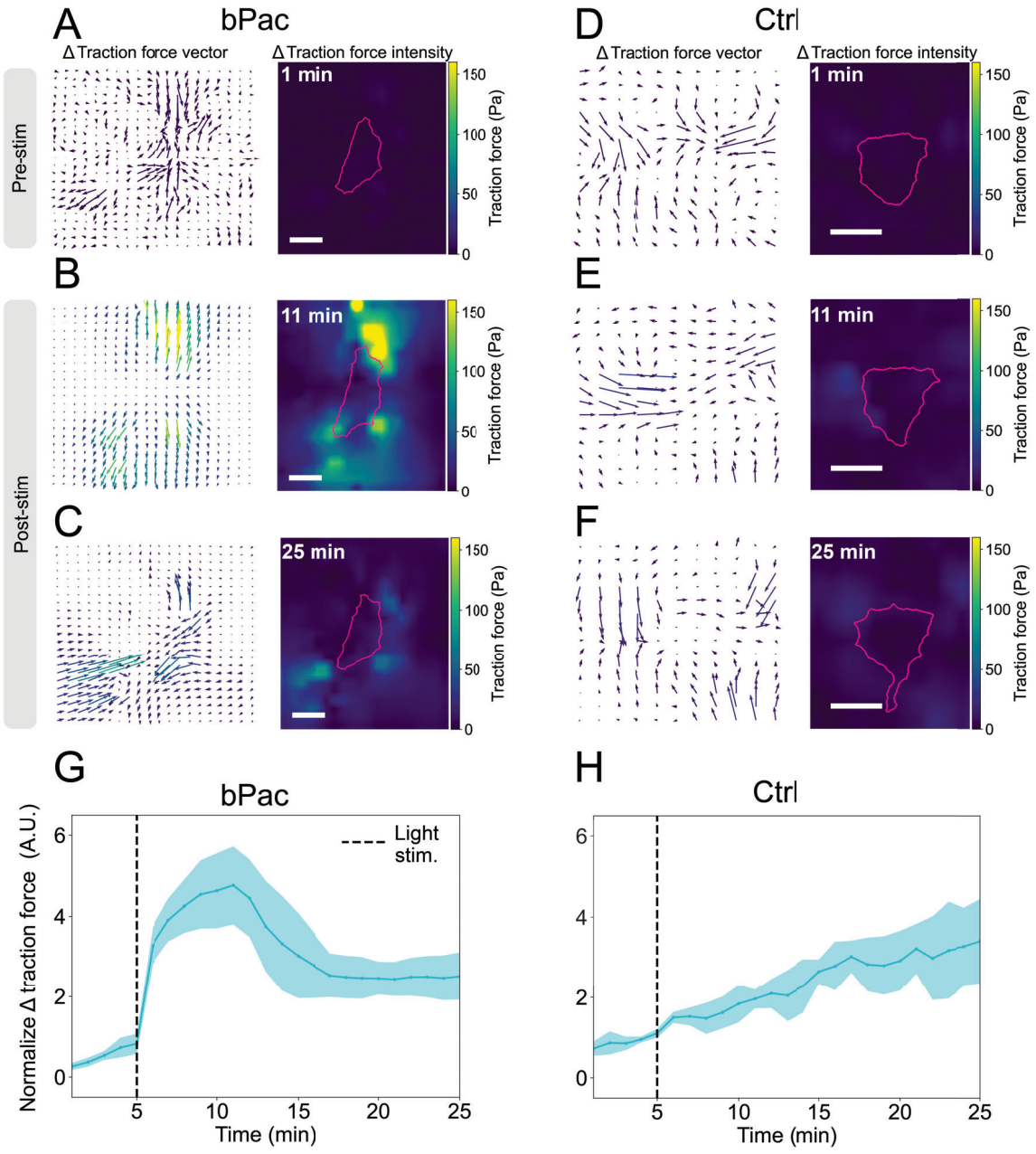

Figure 3·5: bPac activation induces cell relaxation.

A-**F** show the change in traction force (Δ traction force) vector field (left panels) and magnitude (right panels) respective to the first frame. Screenshots of Δ traction force 4 min before light stimulation (**A, D**), 6 min (**B, E**), and 20 min after light stimulation (**C, F**) are displayed, with (**A**)-(**C**) showing an example cell expressing the bPac construct (bPac-mTurquoise2-NES), and **D-F** showing an example cell expressing the control construct (mTurquoise2-NES). In both the vector and magnitude fields, color indicates magnitude. In the vector field, the lengths of the arrows are normalized for each frame. Cells are outlined in pink. Scale bars = 20 μm. (**G**) and (**H**) demonstrate the Δ traction force magnitude over time, with magnitude traces normalized to the pre-treatment values on a per-cell basis. Mean and S.D. of traces between n = 9 cells (bPac construct) and n = 4 cells (control construct) are shown. Photostimulation is applied at the black dashed line using a 445 nm laser at 25% power for 150 ms.

the myosin light chain phosphorylation state (by modulating myosin light chain kinase and phosphatase, for example, reviewed in [120, 121]), or through directly affecting the polymerization of monomeric actin that constitutes F-actin [122], both of which would accompany a structural change in stress fibers in the cells. To test whether bPac-induced cell relaxation is mediated through alternation to the actin cytoskeleton structures, we labeled F-actin with either LifeAct [123] (Fig 3·6 A) or fluorescently-tagged monomeric actin [124, 125] (Fig 3·6 B). In dark conditions, the fibroblast cells display thick, prominent stress fibers on the periphery and through the cell body mostly along the alignment direction of the cells (Fig 3·6 A and B). The stress fiber structures match those seen in earlier studies [126, 127]. Upon bPac activation with light, the thick stress fibers seemed to be dissociated: they became less prominent, with some fiber structures even disappearing. This observation is particularly prominent on the periphery of the cells where thick stress fibers reside before light stimulation (Fig3·6 A and B, left panels). To quantify the stress fiber structure change, we generated a metric we termed stress fiber integrity (SFI, Fig 3·6 C-D). The cell is first masked with an adaptive (local) thresholding algorithm to pick up the median signal intensities on the stress fiber structures (Fig 3·6 C, pink outline). This signal is then divided by the median signal intensity from the whole cell (Fig 3·6 C, blue outline), providing a measurement normalized to the expression level of the actin marker in the whole cell. This metric could reflect the structural change of stress fibers with one

caveat: the absolute quantities vary with the masking parameter (Fig B·5). As expected, when we increased the block size parameter for masking the stress fibers (i.e. a larger local area is used to determine the local threshold), fraction change in the SFI metric decreases upon bPac activation (Fig B·5 D). Nevertheless, the SFI metric acts as a semi-quantitative metric to measure stress fiber integrity.

When we plotted temporal changes of this metric, we see that there is a clear decrease upon bPac activation, which persisted for around 15 minutes after the light stimulation was turned off, followed by recovery (Fig 3·6 E and F, top panels). In the LifeAct-labeled cells, we observed a transient increase of SFI after the light stimulation was turned off. This could be due to the actin marker signal accumulating locally around the nucleus after bPac activation (for example, in Fig 3·6 A, 4 minutes after stimulation started). SFI changes are accompanied by nuclear area decrease (Fig 3·6 E-F, right panels), suggesting that the previously observed nucleus area decrease is likely the result of structural changes of stress fibers.

Variables that could potentially modulate the stress fiber structure change and nuclear area change include the expression level of the optogenetic tool and passage of the cells (with passaging on stiff culture plates, fibroblast cells tend to turn into a myofibroblast-like state [128, 129, 130]). Additionally, the basal levels of these two metrics could affect changes induced by bPac activation. Therefore, we tested whether the extent of stress fiber disintegration or nucleus area change is determined by either the expression level of the bPac tool, passage of cells, or the basal level of those metrics (Fig B·7). Correlation analysis reveals neither normalized decrease of SFI nor nucleus area is correlated with bPac expression level (approximated by CFP median intensity) with both actin markers (Fig B·7 A-D). Additionally, the decrease in the normalized nucleus area does not seem to correlate with the basal nucleus area. However, the reduction in normalized SFI is positively correlated with the basal SFI value, suggesting at this stimulation dosage, bPac stimulation

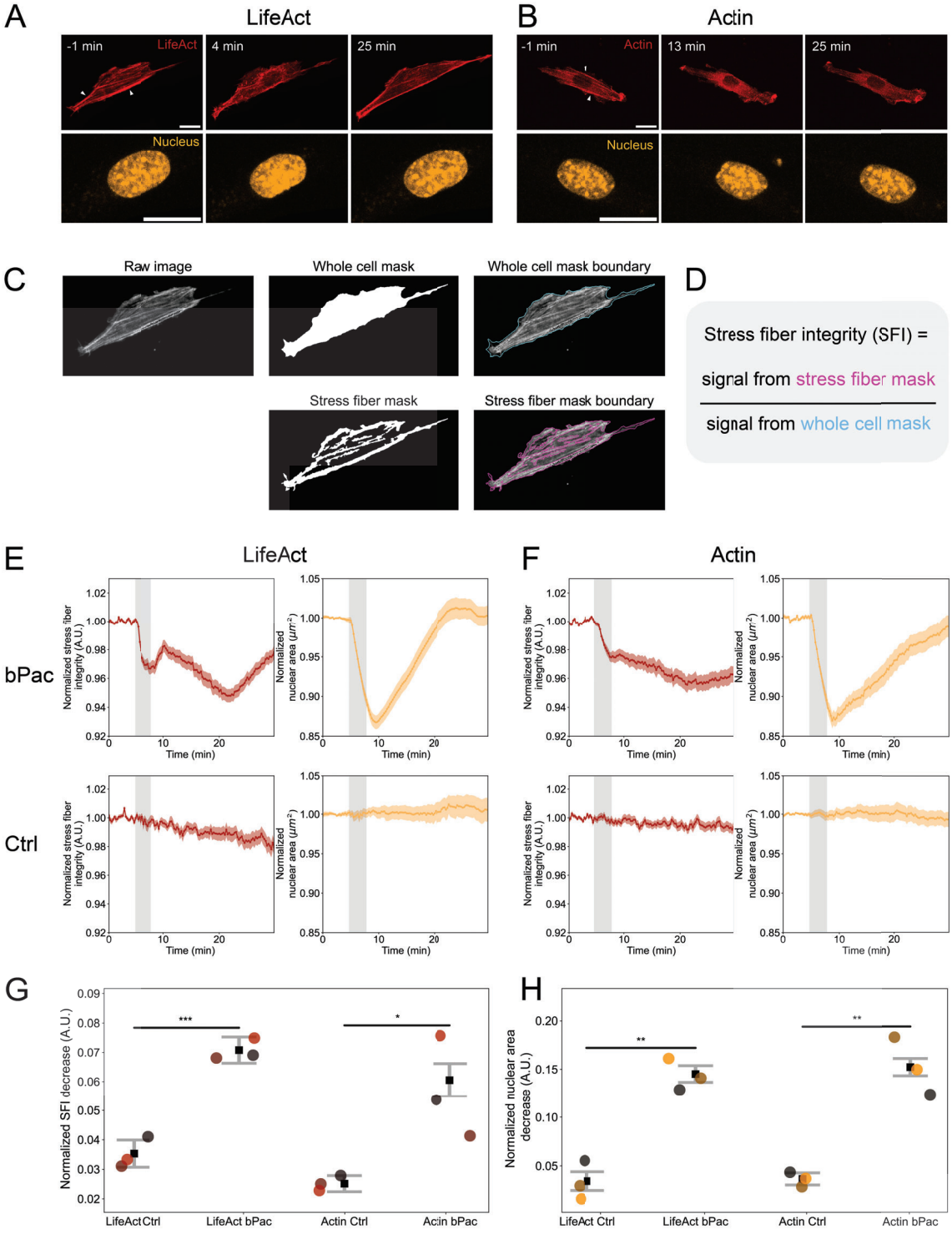

Figure 3·6: bPac activation induces a structural change of the actin stress fiber.

(**A**) and (**B**) show panels of images of the actin marker and the nucleus 1 minute before bPac stimulation, a few minutes after bPac stimulation, and 25 min after the stimulation start. Cells are expressing the optogenetic tool bPac, markers for actin cytoskeleton (LifeAct-mScarlet(i) in (**A**) and mScarlet(i)-actin in (**B**)), and the nucleus is stained with NucSpot. White arrows point at thick stress fibers that undergo disintegration upon bPac activation. Scale bars = 20 μm. (**C**) and (**D**) demonstrate the quantification metric for stress fiber integrity (SFI). In (**E**) and (**F**), the top panels show the quantification from cells expressing the bPac tool, whereas the bottom panel shows results from cells expressing the control construct (mTurquoise2-NES). Temporal traces for stress fiber integrity (SFI) and nucleus area are normalized to pre-stimulation values on a per-cell basis, and the mean and S.E.M. are shown in the left and right panels of (**E**) and (**F**). Photo-stimulation is applied at the grey-shaded region using a 490 nm LED at 10% power. Maximum decrease of SFI and nucleus area are shown in (**G**) and (**H**), with each data point representing the mean value from an independent experiment (cell seeding day), and different colors representing data from different experiments. In (**E**)-(**H**), the total number of cells included for bPac construct with the LifeAct marker, control construct with the LifeAct marker, bPac construct with the actin marker, and control construct with the actin marker conditions are 72, 34, 58, and 40. Student t-test is used for testing between-group differences in mean values from independent experiments. *: $p < 0.05$, **: $p < 0.01$, *** : $p < 0.001$.

decreases stress fiber integrity to a saturating extent (Fig B·7 A, C). We also found that neither decrease of normalized SFI or nucleus area is dependent on cell passage, as the distributions of both metrics are similar across different passages (Fig B·7 E-F).

The observed structural change of the stress fibers suggests the mechanism might involve the depolymerization of F-actin. To test this hypothesis, we labeled cells with a different actin marker, F-tractin [131], a small protein that binds with polymerized F-actin but not monomeric G-actin, distinct from the previous two types of actin markers which label both types of actin. Because the actin marker F-tractin-mScarlet(i) is relatively small in size (around 30 kDa, [132]), markers that dissociate from monomeric actin upon F-actin depolymerization would freely diffuse through the nuclear pore into the nucleus [133]. Upon bPac activation, similar to what is observed with the LifeAct marker, F-tractin signal dissociated from the thick stress fibers accompanied by the signals enriched around the nucleus (Fig 3·7 A-D, 2.5 min after stimulation). Interestingly, after bPac simulation was turned off (i.e. during the recovery phase of actin structure), the F-tractin signal diffused to the nucleus (Fig 3·7 A-B, yellow arrows), a phenomenon that is absent in cells labeled with

LifeAct actin markers (Fig 3·7 C-D). To quantify this observation, we measured the actin signal intensity within the nucleus. Upon stimulation, we observe a fast increase of nuclear actin signal which quickly goes back down after light stimulation was turned off (Fig 3·7) with both actin markers. This is likely due to F-actin dissociation from the stress fibers at the boundary of the cells such that the actin marker signal diffused to areas above or below the nucleus (which is counted as marker signal in the nucleus due to the use of max-z projection). About two minutes after light stimulation was stopped, we noticed a second peak of nuclear actin signal increase (Fig 3·7 E, yellow dot) that is absent in cells labeled with LifeAct. This observation suggests that actin stress fibers break apart during bPac activation phase, but depolymerization of F-actin into monomeric actin happens during the recovery phase.

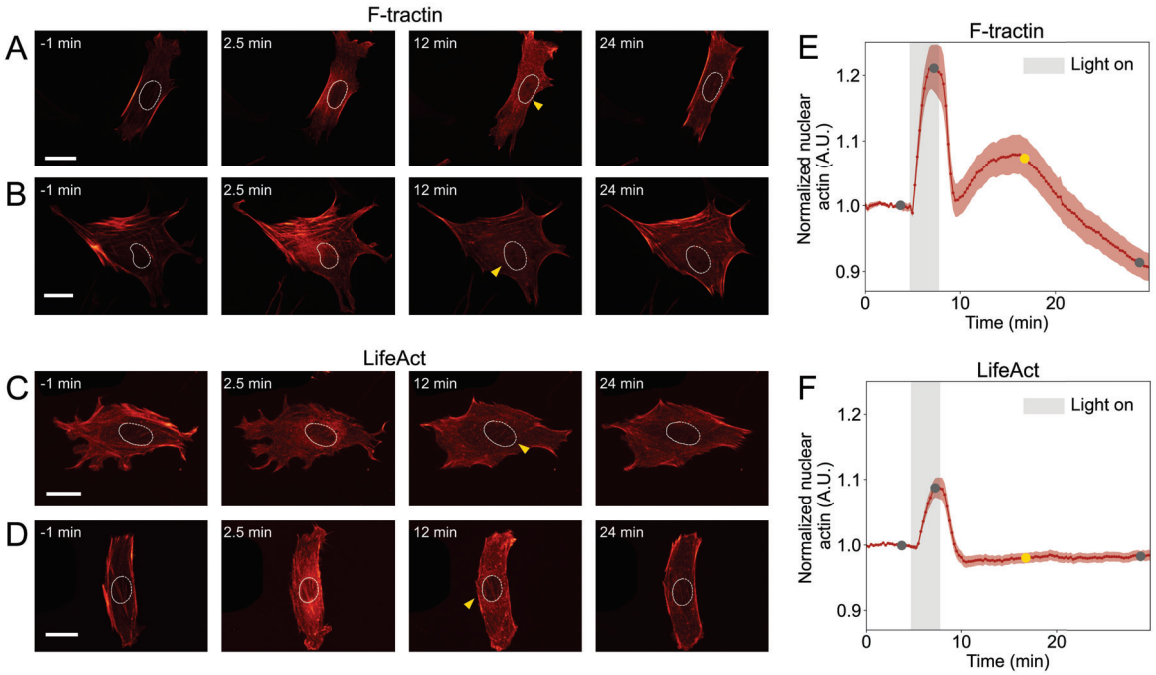

Figure 3·7: F-tractin marker dynamics reveals bPac activation induces F-actin depolarization.

Previous studies have shown that pharmaceutical activation of the cAMP pathway alters actin cytoskeleton structures on a much longer time scale (hours) [134, 135]. To test whether a similar actin stress fiber structure change on the sub-minute time-scale can be in-

(**A**)-(**D**) show panels of images of different actin markers one minute before bPac stimulation, and 2.5 minutes, 12 minutes, and 24 minutes after the stimulation started in representative cells. Cells are expressing the optogenetic tool bPac and actin cytoskeleton markers (F-tractin-mScarlet(i) in (**A**)-(**B**) and LifeAct-mScarlet(i) in (**C**)-(**D**)). Nuclei are outlined with white dashed circles. Yellow arrows point at F-tractin signal diffusing into the nucleus (**A**)-(**B**), suggesting depolymerization of F-actin; and LifeAct signal mostly stays outside of the nucleus (**C**)-(**D**). Scale bars = 20 μm. In (**E**)-(**F**), actin marker signal intensity inside the nuclear region is plotted, with (**E**) quantifying cells with the F-tractin marker (n = 24 cells), and (**F**) quantifying cells with the LifeAct marker (n = 72 cells). Traces are normalized to the pre-stimulation values on a per-cell basis. Black and yellow dots demonstrate data at the four time points as the image panels in (**A**)-(**D**). The solid lines and shading show mean and S.E.M. Grey bars indicate when the photostimulation was on. Photostimulation was applied for a length of 3 minutes using a 490 nm LED at 10% power.

duced with pharmaceutical activators of the cAMP pathway, we treated cells with a cocktail consisting of endogenous adenylyl cyclase activator forskolin (fskn, [108]) and phosphodiesterase inhibitor IBMX. Neither the stress fiber structure nor the nucleus area displayed a significant change upon cAMP activator drugs addition compared to the controls (Fig B·6) on the time scale of tens of minutes. This could be due to the fact that the amount or speed of cAMP production induced by the bPac tool largely exceeds that induced by pharmaceutical approaches. This highlights that the bPac tool uniquely allows us to study cell behaviors in response to transient, acute activation of the cAMP pathway.

Our results also suggest a potential mechanism through which nuclear shape is maintained: the nucleus is basally under tension generated by the contractile actin cytoskeleton. Upon bPac activation, the disintegration of the stress fibers leads to a decrease in these forces. Since the nucleus is linked with the plasma membrane through the stress fibers [136], our data suggest that the nucleus is under outwards tension basally. Therefore, stress fiber tension relaxation leads to the observed nuclear area decrease.

3.2.4 bPac modulates actin cytoskeleton structures through calcium

After establishing that bPac activation induces structural changes in the actin cytoskeleton, we investigated what mediates this response. The cAMP/ PKA pathway has been shown to

modulate multiple protein targets involved in actin structure modulation including myosin light chain, Rho GTPases, and calcium [97, 98]. Calcium is of particular interest because cytosolic calcium activity has been shown as a key regulator for both cell contractility and actin cytoskeleton organization [20, 19] and has extensive crosstalk with the cAMP/PKA pathway [137, 138].

Calcium in the cytosol is modulated by calcium ion exchange between two major stores, the intracellular store (endoplasmic reticulum, ER) and the extracellular space (reviewed in [4, 5]). ER calcium release is generally induced by extracellular ligands activating G protein-coupled receptors (GPCRs) that activate the phospholipase C (PLC) pathway. This leads to inositol 1,4,5-trisphosphate (IP3) production, which sensitizes and promotes the opening of the IP3 receptor (IP3R) on the ER membrane, causing ER calcium release. Calcium influx from the extracellular space can take place when different calcium channels on the plasma membrane open up, either upon the presence of external cues (for example, stretch-activated calcium channels open upon stretch application), or when ER calcium is depleted (leading to calcium influx through store-operated calcium channels). Literature shows the cAMP/PKA pathway modulates intracellular calcium by acting on various aspects of the calcium pathway: including calcium release from the ER store (through sensitizing IP3R), stretch-activated calcium channels (SACCs), and store-operated calcium entry (SOCE) channels [137, 138].

Recent studies have demonstrated a behavior termed calcium-mediated actin reset (CaAR) - a general stress response displayed in multiple cell types during which cortical actin cytoskeleton rapidly reorganizes upon cytosolic calcium increase either through mechanical perturbation [14], pharmaceutical treatment [16] or optogenetic activation [53]. This cellular response shares similarities with the bPac-induced actin fiber reorganization we observed. We thus asked whether the acute actin structure reorganization is mediated through calcium.

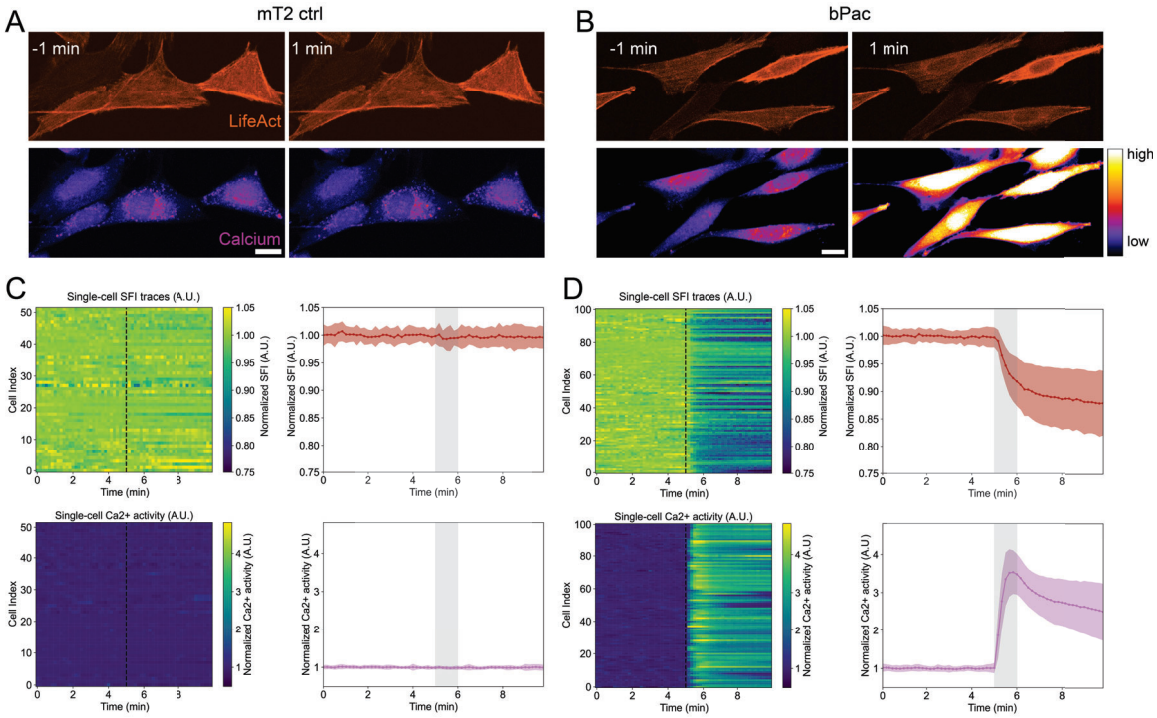

Figure 3·8: bPac activation induces immediate intracellular calcium increase that accompanies actin structure reorganization. (**A**) and (**B**) show representative images of cells expressing the mTurquoise2 control (mT2 ctrl) construct and the bPac construct, respectively. The top panels show actin cytoskeleton (labeled with LifeAct-mIRFP), and the bottom panels show calcium activity dye (Calbryte 590) one minute before and one minute after the start of blue light stimulation. Scale bars = 20 μm. In both (**C**) and (**D**), single-cell SFI traces over time are shown on the left, and the average and S.D. of these traces are shown on the right. Traces are normalized to the pre-stimulation levels on a per-cell basis. On the left panel, the black dashed line denotes the start of bPac stimulation. On the right panel, the grey shaded regions mark the start to the end of the stimulation. For the bPac and mT2 control construct, n = 101 and 52 cells are included respectively. 490 nm LED at 10 %power is used for photostimulation.

We first investigated whether bPac activation induces changes in cytosolic calcium levels. To simultaneously visualize the cytosolic calcium activity and the actin cytoskeleton structure, we used a red calcium dye (Calbryte 590) together with a far-red actin cytoskeleton label LifeAct-mIRFP. Fibroblast cells in culture media basally show sporadic calcium spiking because of serum-residing signaling ligands such as LPA which induce periodic calcium releases from the ER (Fig 3·8 C-D. For a more detailed discussion about serum-induced calcium spiking, please refer to Chapter 2). Upon light activation, we observe

immediate stress fiber disintegration (as is measured in the decrease of SFI) accompanying a large pulse of intracellular calcium (Fig 3·8 B, D). Both changes were absent in cells expressing the control tool mTurquoise2 (Fig 3·8 A, C), confirming that the responses are due to bPac activation. Additionally, the increase in cytosolic calcium occurred at the same time as the onset of SFI decrease, suggesting that both processes are induced immediately (within 10 seconds) upon bPac activation.

After establishing that actin stress fiber reorganization and cytosolic calcium increase are correlated upon transient cAMP activation using bPac, we further tested whether calcium mediates bPac-induced actin reorganization. For cultured cells in steady-state, cytosolic calcium concentration is in the 100 nM range [4]. Calcium increase in the cytosol could come from two major stores: the extracellular space (in the 1 mM concentration range) and the endoplasmic reticulum (ER, calcium concentration in the 100μM range) and is regulated by numerous signaling components (calcium toolkit) [4].

To investigate whether calcium mediates bPac-induced actin reorganization, we first tested cellular response to bPac activation in calcium-free media. Calcium-free media not only eliminates calcium influx from the stretch-activated and voltage-gated channels but also disables calcium from the SOCE process. In calcium-free media conditions, we observed a calcium response of similar height as the cells in the control media (Fig 3·9 B and E) upon bPac stimulation. However, the long tail—sustained high calcium levels after the light stimulation stopped—disappeared in cells residing in calcium-free media, which is reflected in the significant decrease of area-under-curve (AUC) measurement from the calcium traces (Fig 3·9 E and I). Additionally, cells residing in calcium-free media also displayed a decreased change in the SFI metric in response to bPac activation (Fig 3·9 E and J), suggesting that calcium response is essential for mediating bPac-induced actin structure organization. Because we observed residual calcium activation response and SFI response upon bPac activation under calcium-free media conditions, we asked whether cal-

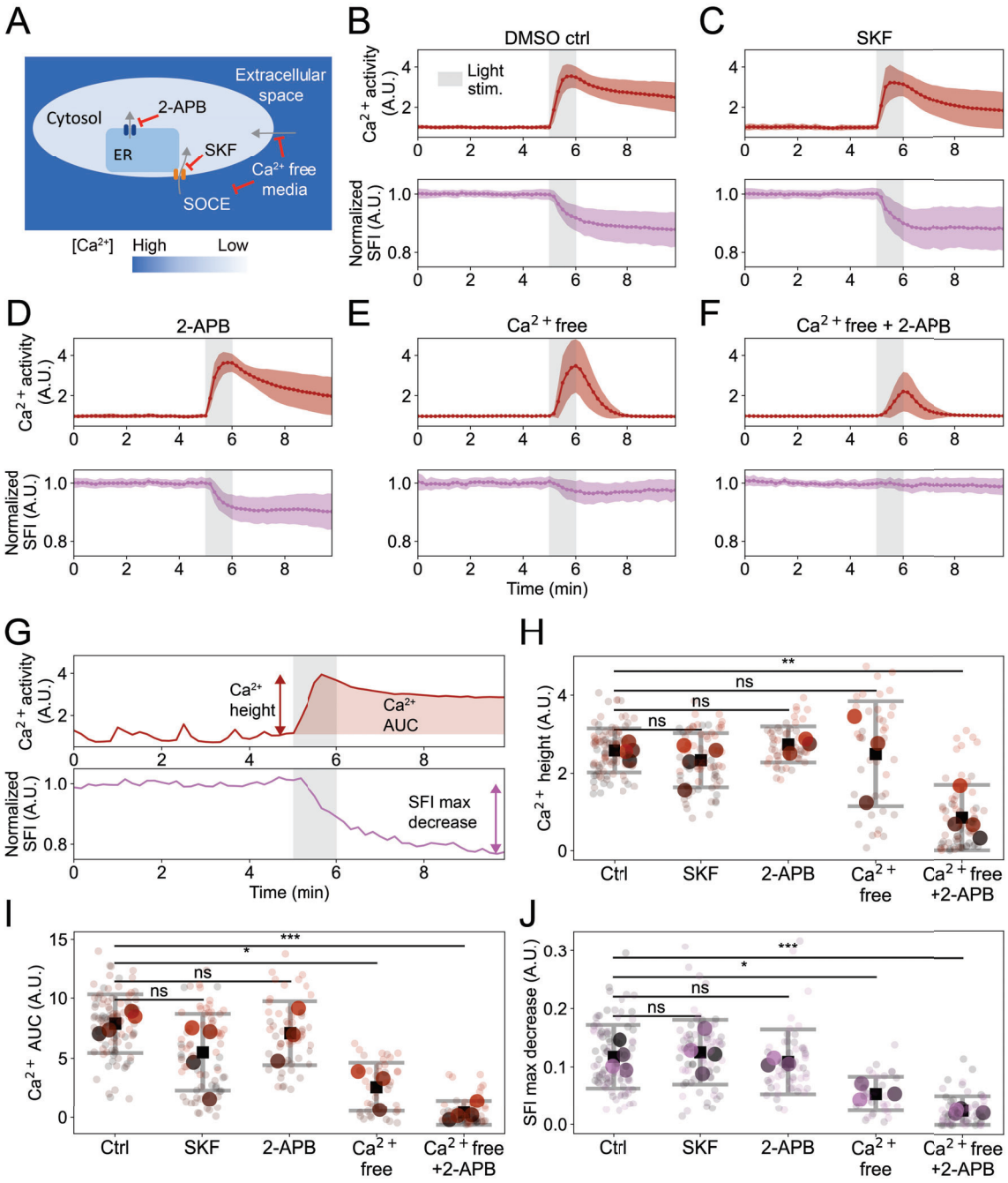

Figure 3·9: bPac-induced actin structure change is mediated through the calcium pathway.

(**A**). Schematic demonstrating two major calcium stores (extracellular space and ER) and acting mechanisms of inhibitor drugs. (**B**)-(**F**). Calcium and stress fiber integrity (SFI) in different media conditions, with top panels showing the calcium signal from the Calbryte 590 dye, and bottom panels showing SFI. Both calcium and SFI traces are normalized to the pre-stimulation levels on a per-cell basis. The mean and S.D. of the traces are displayed. Grey-shaded regions indicate blue light activation. (**G**) demonstrate quantification metrics for calcium and SFI responses. Calcium height (red arrow), calcium area-under-the-curve (AUC, red shaded region), and SFI max difference (pink arrow) are labeled on top of traces from an example cell. Scatter plots of these metrics are shown in (**H**) (calcium height), (**I**) (calcium AUC), and (**J**) (stress fiber integrity maximum decrease). All cells in the experiments stably expressed the bPac construct and the LifeAct-mIRFP actin marker and were stained with Calbryte 590 dye for calcium activity measurement. In (**H**)-(**J**), the black square dot and grey bars mark the mean and standard deviation between individual cells for each media condition, and large colored data points represent the mean value from independent experiments (cell seeding days) and small colored data points mark data from individual cells, with colors representing different experiments. For the control (DMSO) and the SKF (50 μM) media, 2APB (50 μM), calcium-free media, and calcium-free media plus 2APB (50 μM) conditions, n = 101, 76, 56, 41, and 64 cells are included respectively. 490 nm LED at 10%power is used for photostimulation. Statistical tests between conditions are conducted between independent experiments with Tukey's HSD method for data with equal variance and Games-Howell post-hoc test for data that does not show equal variance. ns: not significant, **: $p<0.05$, **: $p<0.01$, ***: $p<0.001$. Statistical results are only calculated between the control media and other treatment conditions.

cium from the ER store could explain these residual responses. To answer this question, we further treated the cells with an IP3 receptor inhibitor 2-APB that inhibits ER-mediated calcium release. Cells in calcium-free media that were treated with 2-APB showed calcium response with a smaller height and AUC, accompanied by almost no change in actin stress fiber organization (Fig 3·9 F, H-J). This suggests ER-mediated calcium release also plays a role in bPac-induced actin stress fiber structure change.

To further investigate the respective roles of ER calcium release and SOCE, we measured cell response to bPac activation in regular culture media in the presence of either the IP3 receptor inhibitor 2-APB or SOCE inhibitor SKF-96365 (SKF). Surprisingly, we observed no apparent differences in the calcium response under IP3R inhibition (2-APB, Fig 3·9 D, H, and I). As expected, SOCE inhibitor treatment (SKF) led to a faster decrease in calcium level after the withdrawal of light stimulation (Fig 3·9 C, also shown in the slight decrease of calcium area-under-the-curve response in Fig 3·9 I), suggesting SOCE is likely

involved in maintaining sustained high calcium levels upon bPac activation. However, there is no significant decrease in calcium area-under-the-curve response when cells were treated with the SOCE inhibitor SKF (Fig 3·9 I). Aligned with the unaltered calcium response, the actin fiber reorganization induced by bPac activation was preserved under either IP3R inhibitor or SOCE inhibitor treatments (Fig 3·9 C, D, J). We suspect the reason to be at least two-fold. Firstly, it has been suggested in the literature that cAMP increase induces calcium release from an ER compartment that is independent of the calcium store released by IP3 alone [139]. Therefore, it is possible that the acute cAMP increase in cells upon bPac stimulation unmasks the ER calcium store that 2-APB can not fully inhibit. Secondly, the effect of bPac activation could be too strong for both inhibitors to act against. Because the SFI metric is normalized to the basal level and therefore only reflects relative changes in actin fiber organization, we checked whether drug inhibition of the calcium pathway would alter the basal level of SFI. When we quantified the basal level of the stress fiber integrity (SFI) metric, we observed no significant difference between calcium-inhibited media conditions compared to control media conditions (Fig B·8). This indicates that the observed differences in actin fiber organization (quantified by SFI) under different media conditions are likely not due to the differences in basal SFI. In summary, our data suggest that bPac-induced actin stress fiber reorganization is mediated through increasing cytosolic calcium, with the initial calcium peak dominated by ER-mediated calcium release and the sustained high cytosolic calcium level mostly mediated by SOCE which requires extracellular calcium.

3.3 Discussion

In this work, we harnessed an optogenetic tool bPac to investigate cell migratory behaviors under direct, transient control of the cAMP/PKA pathway. We first characterized the optogenetic tool using a fluorescent reporter for PKA, and confirmed that the tool can

achieve repetitive pathway activation at the minute-timescale upon light exposure. More importantly, we have shown that the extent of pathway activation can be controlled by light stimulation length and intensity. Using this tool, we applied different strengths of pathway activation by using different light dosages to investigate the effect on cell migration in a standard 2D scratch assay. We found that in both the fibroblast cell line and the epithelial cell line, higher cAMP pathway activation led to lower 2D migration efficiency. By measuring the cell-generated traction force and visualizing the actin cytoskeleton structure, we found that optogenetic activation of the pathway led to a reduction in cell contractility and disruption of stress fiber integrity, both of which can explain migration inhibition induced by cAMP pathway activation. Lastly, we have shown that the optogenetically-induced stress fiber structure change is mediated by cytosolic calcium increase that requires both extracellular calcium influx and ER calcium release.

Our work here is the first work to my knowledge that investigates the modulation of cell migration and actin cytoskeleton structure upon direct, transient control of the cAMP pathway. Previous work has shown that pharmaceutical cAMP/PKA pathway activation leads to a decrease in cell migration efficiency in endothelial cells [140] and epithelial cells that are migrating through confined channels [141]. Additionally, pharmaceutical studies have shown activation of the cAMP/PKA pathway leads to structural change in the actin cytoskeleton in human neuroblastoma cells [134] and astrocytes [142]. Our results show that direct transient activation of the cAMP pathway inhibits migration and induces stretch fiber integrity decrease, which aligns with what was shown in the literature. The key difference between the actin cytoskeleton structure change induced by pharmaceutical studies and bPac activation is that the two processes happen at drastically different timescales (1 to 2 hours for drug treatment, and within a minute for bPac activation, refer to Fig B·6 and 3·6). To understand the origin of this difference, we looked into previous work that compared the effects induced by drug and bPac activation [106]. The work shows that in CA1

pyramidal cells, the cyclic nucleotide-gated cation channel (CNG channel) current induced by bPac is significantly faster and larger in amplitude compared to that induced by a strong pharmaceutical treatment (100 μM fskn + 100 μM IBMX). This suggests that in our work, the difference between bPac activation and the traditional drug treatment is likely dominated by the rate at which cAMP is produced as well as the maximum level of resulting cAMP, and that the actin cytoskeleton structure and migration could be modulated by the time-integral of the cAMP pathway activation.

One unique observation that we had is the recovery dynamics of the cytoskeleton structure and cell contractility—the stress fiber integrity metric recovered around 50% within 10 minutes after integrity reached the lowest point after bPac activation(Fig 3·6 E, F), and the cell contractility displayed a similar extent of recovery within 5 minutes after cells reached maximum relaxation (Fig 3·5). This observation indicates cells are robust to changes in cytoskeleton structure and contractility in response to cAMP pathway activation. It is not clear what cellular components and processes mediate the recovery. Further investigation into these questions would help us understand how cells achieve restoration of the cytoskeleton structure as well as cell contractility.

In this work, we found that bPac activation led to changes in both the structural integrity of stress fibers and cell contractility. More importantly, in both processes, the dynamical responses showed similar time scales: a fast disintegration of stress fibers/relaxation of cell contractility and a slow recovery of stress fiber/cell contractility (Fig 3·6, 3·5). This led to the question of whether the two processes have causal relations. Previous work has shown that during cell adhesion, contractile displacements generated by cells temporally correlate with the dynamics of the density of the actomyosin network, suggesting that actin density is the key modulating parameter for cell contractility [143]. The simultaneous change in actin structure integrity and cell contractility that we observed, although under perturbation of a signaling pathway, echoes the observations in the previous work, and suggests that actin

structure change could be a driver for cell contractility change. In our case, however, it is unclear whether the bPac-induced relaxation is also due to the modulation of myosin contractility. Previous literature suggests PKA can modulate both the myosin light-chain kinase (MLCK) and myosin-light-chain phosphatase (MLCP) to decrease myosin contractility [97, 98]. This calls for further investigation into the potential role of myosin activity in the context of cAMP pathway-induced contractility relaxation, especially with the aim to tease apart the respective roles of actin structure and myosin activity.

In this Chapter, we used different light stimulation strengths for different assays to characterize bPac activation-induced changes in cells, partially due to the fact that different optics were used to deliver light stimulation. To be able to directly compare the responses from different assays, it is necessary to measure the integrated light power applied within each assay. Moreover, to be able to associate responses on the multicellular (cell sheet migration) and single-cellular (contractility, stress fiber reorganization etc.) scales, future work is needed to investigate these responses under identical light stimulation power.

We have shown cytosolic calcium mediates the bPac-induced actin cytoskeleton structure change. However, we have not probed what mediates the calcium-induced cytoskeleton change. There are two potential mechanisms by which calcium increase could lead to the structural change of actin. The first mechanism is inspired by a phenomenon shown in previous work termed "calcium-mediated actin reset" (CaAR) that roughly matches what we observed in bPac-induced actin structure change. Specifically, CaAR describes that an increase of cytosolic calcium (through fluid shear stress, mechanical stretch, drug treatment, or optogentic control) leads to cortical actin disassembly and actin enrichment at the peri-nuclear region [14, 16, 53]. This phenomenon is suggested to be mediated by the formin protein INF2 that rapidly removes actin from the periphery of the cells and forms new F-actin near peri-nuclear ER regions. However, there is a discrepancy between previous work and this work, especially in the cell migratory output. In the previous work,

cytosolic calcium increase induced by extracellular ligand ATP led to increasing 2D migration efficiency in epithelial cells, an observation that is opposite from the bPac-induced migration inhibition that we showed. The second potential mechanism is through a calcium-regulated actin filament-capping protein named gelsolin. Gelsolin is an F-actin filament severing and capping protein whose activity is directly modulated by cytosolic calcium concentrations. Upon binding to calcium ions, gelsolin is activated, which leads to F-actin depolymerization and shorter-length actin filaments [144, 145, 146]. The potential roles of INF2 and gelsolin in the context of bPac-induced actin structure reorganization still deserve to be studied.

In this work, we studied how cAMP/PKA pathway modulates cell behaviors through global control of cAMP. Previous work has shown that subcellular dynamics of the cAMP/PKA pathway are important modulators of cell migration (reviewed by [97, 98]. Specifically, PKA activation was exclusively detected at the protrusions but not in the whole cell [103]. Another work showed oscillatory PKA dynamics at the cell membrane that are correlated with protrusion-retraction cycles. This work further established that protrusion-localized PKA acts as an essential component of a signaling circuit comprising PKA, RhoA, and Rho protein GDP dissociation inhibitor (Rho-GDI), and PKA activity sets the pace of the protrusion-retraction cycles [104, 99]. More generally, cAMP molecules in cells are compartmentalized, and cells usually use the subcellular activity of the cAMP/PKA pathway to execute signal transduction. Compartmentalization of cAMP is established through mechanisms such as PDE degradation [147] and buffering by liquid droplets formed by PKA regulatory units [148]. In addition to regulating protrusion dynamics, subcellular dynamics of the cAMP/PKA pathway also regulate a wide range of downstream effectors and cellular behaviors such as neuronal migration [149], Hedgehog signaling [150], and oncogene-induced cell transformation [148]. Although we did not focus on subcellular control of the cAMP pathway here, the bPac tool can potentially be used to study the role of subcellular

pathway dynamics by tagging the tool to different cellular compartments or using a digital micromirror device (DMD) to achieve subcellular activation.

Here, this body of work focuses on one cell type, the 3T3 fibroblasts, as the model. However, it has been shown that cAMP increase leads to ER calcium release in multiple cell types including HEK cells, DT40 cells, Hela cells, and cardiac cells (reviewed in [151, 138, 152]). Additionally, changes in cytoskeleton structure and cell contractility in response to cytosolic calcium change have been observed in a wide range of cell types (for example, [14, 16, 53, 153]. Therefore, similar phenomena likely exist in other cell types and await further investigation.

In summary, our work provides an in-depth characterization and mechanistic investigation of how the cAMP/PKA modulates migration under direct control of the cAMP/PKA pathway. This work suggests potential mechanisms related to cell contractility, actin cytoskeleton structure, and cytosolic calcium that relate the cAMP pathway activity to migratory outputs.

3.4 Methods

Cell culture, transient transfection, and establishing stable cell lines

NIH 3T3 fibroblasts (American Type Culture Collection, ATCC, CRL-1658) were cultured in DMEM with 4.5 g/L glucose, L-glutamine, and sodium pyruvate (Corning), supplemented with 10% bovine serum (Gibco) and 1% penicillin-streptomycin (Invitrogen). Passages under 12 were used in experiments. MDCK NBL-2 cells (American Type Culture Collection, ATCC, CCL-34) were cultured under passage 21 in Eagle's Minimum Essential Medium (EMEM, ATCC) supplemented with 10% fetal bovine serum (Gibco) and 1% penicillin-streptomycin (Invitrogen). Cells were maintained at $37^{\circ}C$ and 5% CO_2 and passaged at 80-90% confluency with media changed every 2 to 3 days.

Transient transfection was conducted using the Lipofectamine 3000 Transfection Reagent

kit (Invitrogen) according to the manufacturer's instructions. To establish stable pools of construct-expressing cells, the PiggyBac Transposase system [154] was used. Cells were plated and co-transfected with the constructs and Super PiggyBac Transposase using the Lipofectamine 3000 Transfection Reagent kit (Invitrogen). The optogenetic construct (bPac-mTurquoise2-NES) and its control (mTurqiouse2-NES) were co-expressed with Zeocin-resistance gene and selected with media supplemented with 400 μg/mL Zeocin (Invivogen); the actin label and PKA-Booster sensor constructs were co-expressed with a Blasticidin-resistance gene and selected with 5 μg/mL media supplemented with Blasticidin (Invivogen).

Transiently-transfected cells were used for Fig 3·1, B·1, B·3, 3·4, 3·5. Stable pools were used for Fig 3·3, B·4, 3·2, B·5, B·6, B·7, 3·6, 3·7, 3·8, 3·9.

Scratch assay experiments

Cell seeding, optogenetic activation, and imaging

3T3 fibroblasts and MDCKs stably expressing the optogenetic construct, bPac - mTurquoise2-NES, or the control construct, mTurquoise2-NES, and a red cytoskeleton marker LifeAct-mScarlet(i) were seeded in 96-well plates and allowed to form a monolayer. The Auto-Scratch platform (BioTek, Agilent) was used to achieve reproducible gaps in all experimental wells. Cells were maintained in a 37$^{\circ}C$ and 5% CO_2 environment during imaging. Light stimulation and imaging experiment was done using the Cytation 5 plate reader/microscopy system (Biotek, Agilent). Light stimulation was achieved by imaging specific wells using the 488 nm excitation LED. To track cell migration, cells were imaged in TRITC channel through a 4x air objective every 20 minutes. By programming acquisition in Gen5 software (Biotek, Agilent), we multiplexed different temporal stimulation patterns while doing imaging that allowed for tracking of the gap closure process.

Image analysis

Image analysis was conducted using Fiji [155] and Python [156]. Time stacks from the

TRITC channel were first down-sampled to one image every 2 hours. Custom-written Fiji macros were written to generate masks. Briefly, rolling-ball background subtraction was applied to raw fluorescent images followed by contrast enhancement. The resulting images went through a median filter, bandpass filter, variance filter, and maximum filter before finally going through thresholding to generate binary masks. Custom-written Python code was used to extract gap area information at each frame. The fraction of gap area closed was calculated by normalizing the gap area to that at 2 hours after gap creation. Data between 2 hours to 24 hours were used for linear fitting and closure rates were determined by the slope of the fitted lines.

Single-cell imaging experiments

Cell seeding and imaging

Cells were seeded on glass-bottom plates and placed in an incubator chamber maintained at $37°C$ and 5% CO_2 (OKO Labs) for imaging experiments. Confocal imaging was conducted with Ti-2E Eclipse Microscope with a perfect focus system (Nikon Instruments) with Dragonfly Spinning Disk Confocal System (Oxford Instruments), and time-series images were acquired with an iXon 888 Life EMCCD camera (Oxford Instruments). Samples were imaged through a 20x air objective for Fig 3·1 and B·3; a 40x air objective with a 1.5x zoom in the microscope for Fig 3·6 ; a 40x air objective for Fig 3·4, B·1, 3·5, B·5, and B·8; a 60x oil objective for Fig 3·7 and B·6. Specific imaging settings are detailed below. Before imaging, culture media was replaced with imaging media consisting of Fluorobrite DMEM (Gibco) supplemented with 1% Glutamax (Gibco) and 10% serum depending on cell type.

Optogenetic activation

Optogenetic activation was conducted in one of the three following ways. In the first way, the Optoplate system was built as instructed in literature [109], and was programmed to apply different durations and intensities of 465 nm light stimulation. In a second way, the

stimulation was applied with a 445 nm laser in the confocal microscope system. In the last way, 490 nm LED on the PE4000 LED system (CoolLED) was used, and light intensity and duration were controlled using a Mightex control pad. Specific light stimulation settings are detailed in figure captions.

PKA-Booster sensor

For imaging PKA Booster sensor in the drug validation experiments (Fig B·1), samples were imaged using a 445/514/561/640 dichroic. The donor-donor channel was imaged using a 514 nm excitation laser, and 540/15 emission filter; the donor-acceptor channel was imaged using a 514 nm laser and 698/77 emission filter; the acceptor-acceptor channel was imaged using a 561 nm excitation laser and 698/77 emission filter. For imaging PKA Booster sensor in the bPac stimulation experiments (Fig B·1 and 3·1), to prevent activating bPac during sensor imaging, 561 nm excitation laser with 540/15 emission filter was used for the donor-donor channel, and 561 nm excitation laser with 698/77 emission filter was used for the donor-acceptor channel.

Actin cytoskeleton, nucleus, and calcium activity imaging

Actin was labeled with LifeAct [123], F-tractin [131], or actin monomer attached with mScarlet (i) [132] or mIRFP670 [157]. Nuclei are labeled with NucSpot 650 Live Cell Nuclear Stain (Biotium) following the manufacturer's instructions. Samples were imaged through a 445/514/561/640 dichroic. 561 nm excitation laser and 620/60 emission filter are used for imaging the mScarlet-(i) signal, 634 nm excitation laser and 698/77 filter are used to image the NucSpot650 signal or the miRFP670 signal. To visualize calcium dynamics, cells were incubated with Calbryte 590AM calcium indicator dye (ATT Bioquest) according to the manufacturer's instructions for 40 minutes before imaging. Confocal imaging using 40 μm pinholes was conducted. To capture actin fiber structures throughout cell height, z-stack images were acquired for a total of 6 steps with 1 μm/ step. Max projections of the z-stacks were used for visualizations and quantifications. The step size of z-stack was

determined such that smaller sampling steps would neither improve resolution qualitatively nor change the SFI metric quantification.

Optogenetic bPac construct imaging

At the end of time-series imaging, bPac-mTurquoise2-NES channel was imaged with a 445 nm excitation laser and 480/40 emission filter through a 445/514/561/640 dichroic.

Image analysis

All image analysis was conducted using Fiji [155] and custom-written Python [156] scripts. For all quantification metrics (FRET signal, SFI, nuclear area, calcium intensity), masks were generated by built-in functions from the scikit-image package [158]. The raw traces generated from each time frame were normalized to the mean baseline values (mean values across time points before light stimulation) before further analysis (e.g., peak detection, height/width measurement).

For FRET signal extraction, background subtraction was applied to each channel of the multi-channel time series before further analysis. Cells were masked using the adaptive thresholding method on the channel with the highest brightness. FRET signal was calculated from the pixel-by-pixel division of the donor-acceptor channel over the donor-donor channel. Median pixel values from the mask were extracted as the FRET signal. PKA response peaks were detected using the find_peaks function in Scipy package [159]. Height was calculated by the prominence of the detected response peak, and width was calculated by the full width at half maximum (FWHM) of the response peak.

To quantify actin stress fiber integrity (SFI), maximum z-projections from the z-stacks of the actin channel images were first calculated. Whole-cell masks were generated by adaptive thresholding followed by median filtering and filling-holes. Actin stress fiber masks were generated by adaptive thresholding with a smaller neighborhood size followed by median filtering. The median pixel intensity from the stress fiber mask is divided by that from the cell mask to generate SFI measurements. Maximum difference of SFI was

calculated by subtracting the minimum value of SFI after light stimulation from the baseline SFI value.

The nuclear area was measured either from the dark void region in cells expressing the PKA-Booster sensor with a nuclear escape sequence (NES), or from the nuclear channel when the nucleus is labeled with NucSpot650 dye. In both cases, area measurements were generated from masking with adaptive thresholding methods on every frame.

As for calcium activity, the whole cell mask generated with the actin label channel was used, and the median intensity in the calcium channel was extracted. Calcium response height was calculated from peak prominence detected by the find_peaks function in Scipy package [159].

Traction force microscopy

Traction force microscopy was conducted following procedures published previously [117, 160]. Briefly, polyacrylamide hydrogel substrates with an elasticity of around 1.25 kPa were made on glass bottom plates. Infrared-colored beads (Carboxylate-modified microspheres, Thermo Scientific, 0.2 μm diameter) were used to track substrate deformation to calculate the change in cell contractility. To allow for efficient coating of the extracellular matrix (ECM) protein onto the substrate, Sulfo-SANPAH (Sigma) was UV-crosslinked to the polyacrylamide gel. The gel was then incubated with the ECM protein fibronectin (from bovine plasma, Sigma) before being seeded with cells.

Cells and fluorescent beads embedded in the substrate were imaged using confocal imaging with 40 μm pinholes through a 445/514/561/640 dichroic. Cells expressing mKO-κ-NES were imaged with 561 nm excitation laser and a 540/30 emission filter to avoid activating the bPac construct. Infrared beads were imaged with a 634 nm excitation laser and 698/77 filter. Z-stack images were acquired for a total of 8 steps with 2.5 μm/step. Max projections of the z-stacks were used for visualization and quantifications. Sets of two images of the beads from the first frame and the following frames were used to calculate the

change in traction force (Δ traction force). Δ traction force was calculated using custom-written imageJ and Python scripts [161] taking advantage of the imageJ plugin PIV and FTTC [162, 163]. The average magnitude across the whole FOV was used to quantify Δ traction force at a specific time frame with a single cell.

Pharmaceutical inhibitor treatment

Calcium-free media consists of DMEM (high glucose, no glutamine, no calcium, Gibco) and 1% Glutamax (Gibco). Cells were rinsed with calcium-free PBS before being changed to calcium-free media. Calcium pathway inhibitors used are 2-APB (50 μM, Santa-Cruz) and SKF 96365 (50 μM, hydrochloride, Cayman Chemical). The cAMP/PKA pathway inhibitor cocktail includes 20 μM forskolin (Sigma) and 1 mM IBMX (Sigma). Cells were incubated with inhibitor drugs for about 1 hour before imaging. For the PKA-Booster sensor validation experiment (Fig B·1), 10 μM forskolin (Sigma) was injected into imaging wells while imaging was paused.

Recombinant DNA

Plasmids used in this work were constructed with standard Gibson cloning methods [164], with parts coming from different sources as detailed below.

Plasmid name	**Source**	**Identifier**
pCAGGS-4493NES (PKA-Booster)	Addgene	#138373
pCAG-4589NES (PKA-Booster(T/A))	Gift from Dr. Kenta Terai lab	N.A.
pPBbsr-PKA-Booster-NES	Custom made	N.A.
pPBbsr-PKA-Booster(T/A)-NES	Custom made	N.A.
pPBbsr-mKOκ-NES	Custom made	N.A.
pPBzeo-bPac-mTurquoise2-NES	Custom made	N.A.
pPBzeo-mTurquoise2-NES	Custom made	N.A.
pPBbsr-LifeAct-mScarlet(i)	Custom made	N.A.
pPBbsr-LifeAct-mIRFP670	Custom made	N.A.
pPBbsr-Ftractin-mScarlet(i)	Custom made	N.A.
pPBbsr-mScarlet(i)-actin	Custom made	N.A.
pCAG-SuperPiggybac	Gift from Dr. Wilson Wong lab	N.A.

Chapter 4

Serum induces intracellular calcium spiking through LPA-mediated ER calcium release

4.1 Introduction

In **Chapter 3**, we investigated how a behavioral output (migration) is controlled by the intracellular signaling molecule (cAMP) in mammalian cells using new experimental techniques. Here in **Chapter 4**, we turned to investigating how environmental input is encoded in intracellular signaling molecule, again harnessing the new experimental tools. Specifically, this **Chapter** focuses on the signaling molecule calcium in response to the presence of an external molecule.

Calcium is a ubiquitous signaling molecule that is important for regulating cell behaviors across cell types. Calcium signaling has been shown to play a significant role in regulating biological processes like cell migration [165], embryonic development [166] and cancer progression [167]. Cytosolic calcium is one of the master regulators that links a variety of environmental inputs to various types of cellular outputs [4, 5]. Environmental cues that modulate cytosolic calcium activity include biochemical ligands such as ATP released from damaged cells [7] and applied forces such as stretch [14] and squeeze [15]. Cellular outputs that are regulated by calcium include cellular contractility [19], actin cytoskeleton organization [14, 16], migration [20], proliferation [22], gene expression (reviewed in for example [4, 5]) and secretion [23]. Understanding how environmental inputs modulate cytosolic calcium (termed calcium encoding) is essential for understanding mechanisms

coordinating a wide range of biological processes.

One outstanding feature of calcium signaling is that it generally functions by generating changes in dynamics rather than steady-state levels to encode environmental information and modulate downstream behaviors [4, 5, 6, 168]. Generally, there are two types of calcium dynamical responses: an immediate increase of cytosolic calcium which eventually returns to baseline (a calcium pulse), or persistent trains of calcium transients (commonly called oscillations, or in this work, calcium spiking).

Cytosolic calcium dynamics can be modulated by environmental inputs. For example, a calcium pulse can be elicited by lysophospholipid acid (LPA) in karatinocytes [13], stretching forces in fibroblasts [14], fluid shear stress in multiple epithelial cell lines [16], and electrical signals in muscle cells [169]. On the other hand, calcium spiking can be induced by ATP in fibroblast cells [56], carbachol (CCh) in HEK cells [8], peptide–MHC complex in immune cells [9, 10]), or culturing on stiff substrates in mesenchymal stem cells [17, 18]. Calcium dynamics also play an important role in regulating downstream effects (reviewed in [30]). For example, by orthogonally controlling calcium oscillation frequency and duty cycle (integrated calcium concentration over a period), researchers found the calcium-regulated transcription factor NFAT is sensitive to the duty cycle rather than the frequency of calcium activity [32]. These results highlight the important role of calcium dynamics in both encoding external cues and regulating downstream behaviors.

When studying the environment encoding of calcium activity, there are three major classes of questions: (1) how do calcium dynamics encode information about the environment, (2) where do the calcium ions come from, and (3) because there is crosstalk between calcium and multiple other intracellular signaling pathways, how do these pathways modulate calcium?

Decades of work have investigated how external cues modulate calcium dynamics in different cell types. A significant fraction of the previous work on in vitro cell culture mod-

els was conducted under regular cell culture media conditions (with serum supplement), likely to maintain cell health (for example, [17, 170, 171, 172]). However, a full characterization of Ca^{2+} dynamics and their origins have not been made in standard cell culture conditions. One component in culture media that could potentially shape calcium dynamics is serum, which consists of numerous bioactive components such as growth factors, albumin, and lipids.

In this work, we focus on the encoding of calcium dynamics in a mammalian fibroblast cell line (NIH 3T3) under standard cell culture conditions. We found that serum supplement in regular culture media induces repetitive calcium spiking in fibroblast cells. We then identified one key serum-borne component accounting for serum-induced spiking, lysophosphatidic acid (LPA), and characterized how different LPA concentrations shape calcium dynamics. Further, we investigated which calcium toolbox components are relevant in LPA-induced calcium spiking. We confirmed extracellular calcium is indispensable for LPA-induced calcium spiking, and ER calcium release is the major source of calcium spiking. Additionally, given LPA's ability to activate a wide range of signaling pathways, including ones that have extensive crosstalk with calcium, we investigated the role of those pathways in shaping LPA-induced calcium dynamics. We identified PKA as one important signaling molecule that shapes the LPA-induced calcium dynamics. Our work suggests that future studies focusing on the environmental encoding of the calcium pathway take the effect of serum into account.

4.2 Results

4.2.1 Serum induces calcium spiking in 3T3 fibroblast cells and LPA is the major responsible component

To characterize calcium dynamics in regular culture media, we stably expressed the genetically encoded calcium sensor jGCaMP7b [173] in 3T3 fibroblasts (Fig 4·1A). By simply

incubating cells in culture media (basal media supplemented with 10% bovine serum), nearly all cells displayed repetitive calcium spiking, with each spike characterized by a sharp calcium increase in the whole cell body followed by a quick decrease to the baseline (Fig 4·1B). By contrast, this whole-cell calcium spiking behavior was absent in cells in basal media (without serum supplement, Fig 4·1E), suggesting that serum-residing component(s) are responsible for the calcium spiking behavior. While for cells cultured in basal media (media without serum supplement), we observed calcium fluctuations with small amplitudes in subcellular compartments like protrusions, rarely did any cells show whole-cell spiking (data not shown). To confirm that the calcium spiking behavior is not specific to one serum preparation, we incubated cells in media containing serum from three different vendors. All three lots of serum induced repetitive calcium spiking in a large percentage of the population (Fig C·1), confirming that serum-induced calcium spiking in 3T3 fibroblasts is a general phenomenon that is not specific to a particular serum lot.

After establishing that serum supplementation in basal culture media induces calcium spiking in 3T3 fibroblast cells, we asked what serum component(s) are responsible for this behavior. Serum is derived from animal blood whose components are usually poorly defined. Serum components that can potentially regulate cell signaling include various growth factors, hormones, and lipids. We investigated two serum components that could potentially be responsible for serum-induced calcium spiking in fibroblast cells, manganese ions (Mn^{2+}) and lysophosphatidic acid (LPA). Both components exist in abundance in serum but are not present in basal media. First, Mn^{2+} has been shown to induce the activation and clustering of integrins [174, 175, 176]. Because integrin engagement has been shown to induce cytosolic calcium increase in a variety of cell types [177, 178], we hypothesized that Mn^{2+} could be a potential serum component that induces calcium spiking. Second, LPA is a lysophospholipid usually bound to albumin that is naturally abundant in serum (100 nM to the micromolar range) [179, 180]. Previous studies have shown that LPA induces

cytosolic calcium increase through calcium release from the endoplasmic reticulum (ER) in several cell types including astrocytes [11], keratinocytes [13, 181], and human foreskin fibroblasts [12, 22].

To investigate whether Mn^{2+} may account for serum-induced calcium spiking in fibroblasts, we supplemented basal media with Mn^{2+} at concentrations similar to those found in fetal bovine serum [182]. Mn^{2+} supplemented media did not induce calcium spiking in the majority of fibroblast cells (Fig C·1A), indicating that it is unlikely the component responsible for serum-induced calcium spiking.

To investigate whether LPA may act as a potential serum component inducing calcium spiking, we first measured the calcium dynamics while incubating cells in serum-supplemented media that was treated with activated charcoal. Activated charcoal strips fatty acid components from the media [183, 184, 185], including LPA. The fraction of spiking cells is reduced by more than half in charcoal-stripped media (Fig 4·1 C, E), suggesting that the major calcium-inducing component in serum is likely a fatty acid. Supplementing the charcoal-stripped media with 10 μM purified LPA rescued calcium spiking in almost all cells (97.8%), a significant increase from the 33.8% of spiking cells in charcoal-stripped media (Fig 4·1 D, E). Next, we asked whether LPA alone is sufficient for inducing calcium spiking. Basal media supplemented with 10 μM LPA induced calcium spiking in almost all cells with no significant difference between the LPA- and serum-supplemented media conditions (Fig 4·1E).

To further confirm that LPA is the major serum component responsible for the observed calcium spiking, we treated cells with an LPA receptor (LPAR) inhibitor Ki16425 (Ki), which inhibits several subtypes of LPARs on the plasma membrane including LPA1, LPA2 and LPA3 [186, 187]. The addition of Ki to serum-supplemented media did not completely abolish calcium spiking (Fig 4·1 F). However, the spiking frequency significantly slowed down after Ki inhibitor addition (Fig 4·1 F). To quantify the change in spiking rate after

Ki treatment, we first used the inverse of the mean calculated from interspike-intervals (ISI, demonstrated in Fig 4·2A) to measure spiking frequency, and then calculated the fold difference of spiking frequency between after and before Ki treatment. Indeed, Ki inhibitor decreased spiking frequency significantly compared to treatment with the DMSO control (Fig 4·1 G). The persistence of calcium spiking upon Ki inhibitor treatment, albeit at decreased frequency, could be explained by the fact that Ki only strongly inhibits a subset of LPA receptors (including LPA1 and LPA3), but weakly inhibits others such as LPA2 which is expressed in 3T3 fibroblast cells [187].

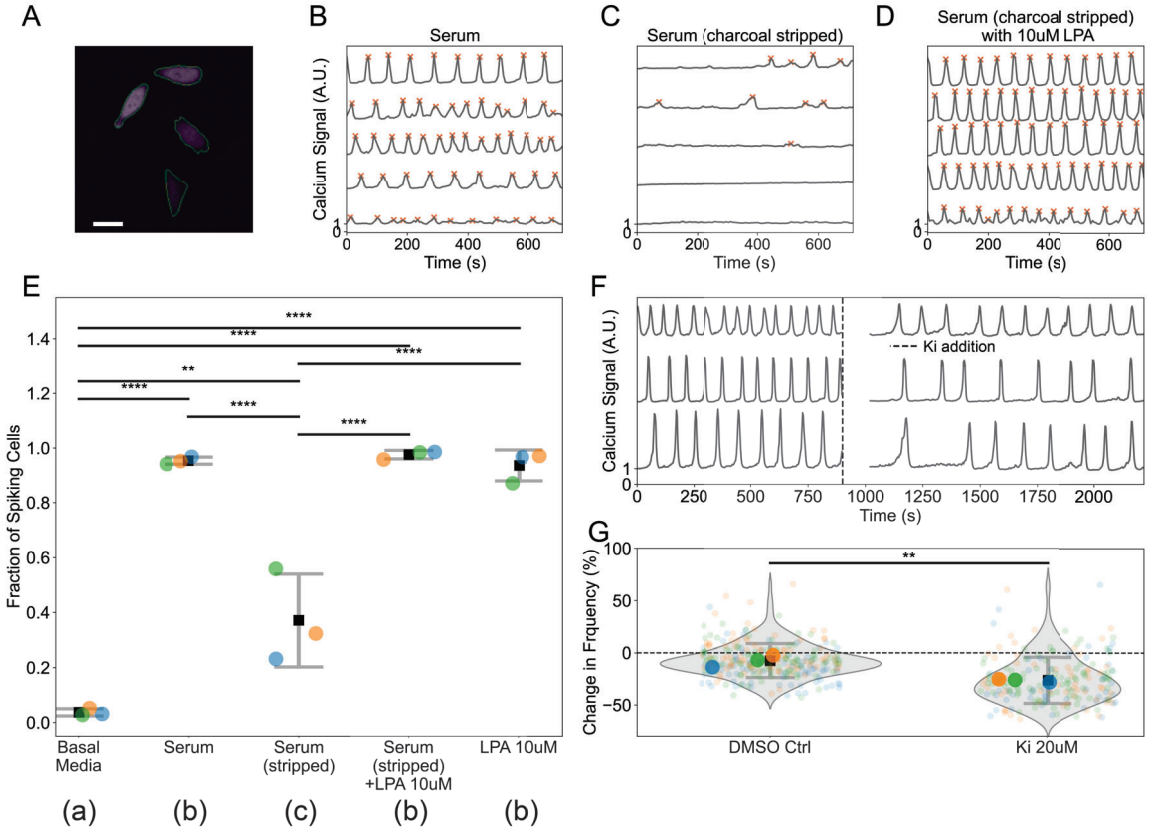

Figure 4·1: Serum induces calcium spiking in 3T3 fibroblast cells and LPA is a major active component in serum

It has been shown that biochemical inputs (composition and concentrations of ligand) often encode the frequency of calcium dynamics [188, 168]. Therefore, we asked whether

(**A**) Image of 3T3 fibroblasts expressing the genetically-encoded calcium sensor jGCaMP7b [173]. Green lines outline cell boundaries from automatic segmentation output. Scale bar: 25 μm. Temporal traces of calcium dynamics from 5 representative cells are shown for cells incubated in basal media supplemented with bovine serum (**B**), basal media supplemented with charcoal-stripped serum (**C**), and basal media supplemented with 10μM LPA (**D**). Red cross marks represent detected spikes. (**E**) Fraction of spiking cells in basal media, basal media supplemented with bovine serum, charcoal-stripped serum, charcoal-stripped serum + 10μM LPA, and just 10μM LPA. Large colored dots represent data from individual wells. The total number of cells is n = 829, 710, 813, 681, and 823 for the five respective conditions. Each condition includes 3 independent experiments (cell seeding days). Black squares and error bars represent the mean and S.D. from independent experiments. (a) to (c) labels are used to distinguish conditions with significant statistical differences. (**F**) Calcium dynamics of 3 representative cells in serum-supplemented media upon addition of the LPAR inhibitor Ki16425 (Ki). At the dashed line, 20μM was added. (**G**) Percentage change of spiking frequency before and after Ki inhibitor application. In (**G**), large colored dots represent the mean frequency change in each experiment, while small colored dots represent data from individual cells. Black squares and error bars represent the mean and S.D. between independent experiments. n = 197 and 273 cells from 3 independent experiments were included for Ki inhibitor or DMSO control, respectively. In both **E** and **G**, colors represent different experiments. Statistical tests were conducted with data from independent experiments. Tukey's HSD method was used for data with equal variance and Games-Howell post-hoc test was used for data that does not show equal variance. ** $p<0.01$, **** $p<0.0001$. The significance value is not marked for condition pairs that do not show a significant difference.

the spiking frequency is modulated by different media conditions. The mean spiking frequency for cells cultured in charcoal-stripped media is 11.7 mHz, which is significantly lower compared to 18.0 mHz measured from cells in regular serum-supplemented media (Fig C·2). Both replenishing 10 μM LPA to serum-stripped media and supplementing basal media with purified LPA rescued the frequency decrease (Figure C·2), indicating that LPA in serum modulates the frequency of calcium dynamics.

These results show that serum in culture media induces calcium spiking in 3T3 fibroblasts and that LPA accounts for a major part of serum-induced calcium dynamics. Previous studies investigating environmental encoding of calcium signaling often include serum in the media, likely to maintain cell health throughout experiments (for example, [18, 56, 170, 172]). Our findings suggest that the observed calcium activity in such cases is potentially confounded by calcium spiking due to LPA in serum.

4.2.2 LPA concentration tunes the threshold, frequency, and potentially amplitude of calcium spiking

Calcium dynamics induced by external ligands are often fine-tuned. Ligand concentration can not only determine the type of calcium response (for example, one pulse or repetitive spiking) but also in many cases modulate the frequency and amplitude of calcium spiking (termed frequency encoding and amplitude encoding) [6, 30, 29, 189]. For example, calcium spiking frequency is modulated by ATP concentration in fibroblast cells cultured on soft substrates [171], and by carbachol (CCh) concentration in HEK cells [8]. However, a lack of frequency modulation has also been observed in several cell and ligand types. For example, frequency encoding does not seem to take place for calcium spiking in fibroblasts cultured on stiff glass in response to ATP [56], for calcium spiking in mouse lacrimal cells in response to methacholine [190], or for calcium spiking in fish cells in response to several different ligands [191]. Another characteristic related to calcium dynamics is spike amplitude. Amplitude encoding of calcium dynamics by external ligands is observed in various

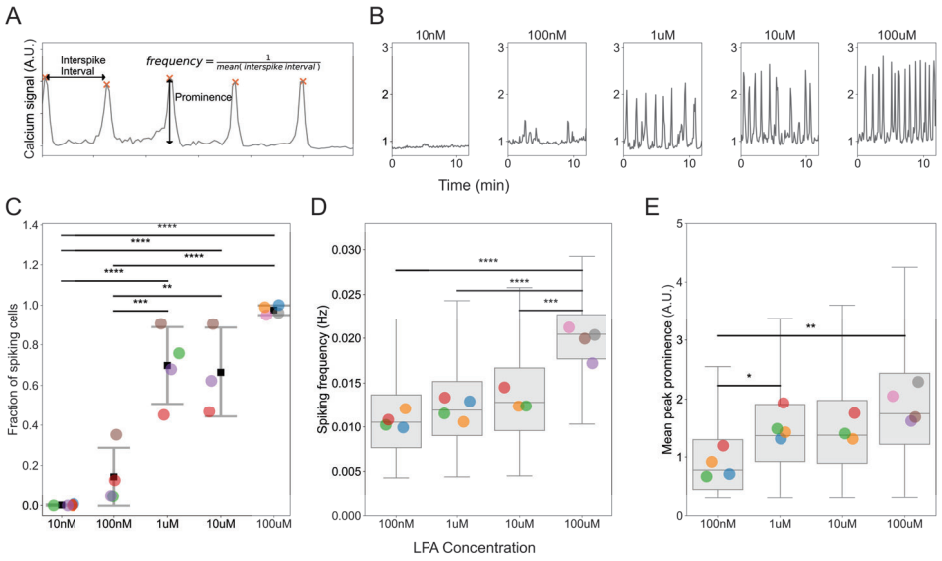

Figure 4·2: LPA concentration modulates the threshold, frequency, and amplitude of calcium spiking in 3T3 fibroblast cells. (**A**). Representative calcium signal trace (gray) and quantification metrics. Orange cross marks represent detected spikes. Calcium signal frequency is quantified by the inverse of the mean of interspike intervals (ISI), and amplitude is quantified as peak prominence. (**B**) Representative calcium signal traces under different LPA concentrations. (**C**) Fraction of spiking cells with different LPA concentrations in basal media. n = 1390, 1539, 2061, 1135, and 996 cells were included for the five respective conditions. Large dots represent the fraction of spiking cells from independent experiments (cell seeding days). Black squares and error bars represent the mean and S.D. from experiments. (**D-E)** show spiking frequency and amplitude under different LPA concentrations. Large dots represent the mean metrics calculated from independent experiments. Box plots show data from individual cells, with the upper and lower bars representing the maximum and minimum value, box boundaries representing the 75th and 25th percentile, and the center bar representing the median of data. n= 225, 1432, 740, and 968 cells were included for the four respective conditions. In (**C-E**), different colors represent different experiments. Statistical tests between conditions are done between independent experiments with Tukey's HSD method for data with equal variance, and Games-Howell post-hoc test for data that does not show equal variance. * $p<0.05$, ** $p<0.01$, *** $p<0.001$, **** $p<0.0001$. For condition pairs that do not show a significant difference, significance values are not marked.

cell types including hepatocellular carcinoma [192], fish hepatocytes [191], intestinal stem cells [193], and macrophages [194]. In addition to encoding information related to the average calcium concentration, amplitude encoding is also suggested to be more robust to changes in environmental temperature [195]. Because in many cases, these detailed characteristics of calcium dynamics are closely associated with cell behaviors and functions (for example in [32] and reviewed in [30, 29]), delineating how they are shaped by external cues is important for understanding the biological consequences of these cues. Along this line, we asked how LPA concentration shapes calcium dynamics in 3T3 fibroblast cells.

To investigate how LPA concentration modulates calcium spiking, we recorded calcium dynamics after injecting LPA of different concentrations (from 10 nM to 100 μM) into the basal media. To capture a range of characteristic behaviors related to calcium dynamics, we investigated the threshold, frequency, and amplitude of calcium spiking in fibroblast cells. The spiking threshold for a population of cells is approximated by the fraction of spiking cells. Because calcium spiking is sporadic in nature [8, 196], we used the mean of interspike interval (ISI) to approximate spiking frequency. To measure spike amplitude, we first normalized the signal intensity to baseline reporter intensity and used the mean prominence of the spikes as an approximation to calcium spiking amplitude (Fig 4·2A).

Firstly, we observed time-dependent behavior in calcium spiking after LPA injection into media (Fig C·3). Across all concentrations, after LPA injection, the fraction of spiking cells, spiking frequency, and prominence all decrease over time. This could be explained by lipid phosphate phosphohydrolase (LPP) that is naturally expressed on the plasma membrane that degrades LPA over time [197, 198]. Additionally, the LPA receptor, like other G-protein-coupled receptors, goes through desensitization and internalization upon sustained LPA stimulation [199, 200, 201], which leads to decreased sensitivity to LPA over time after the exposure to LPA, potentially leading to decreased calcium spiking over time. The time-dependent reduction in calcium spiking was not observed in serum-induced cal-

cium spiking. This could be in part due to the fact that binding to serum albumin protects LPA against degradation by lipases [202]. To be able to compare calcium spiking dynamics between LPA concentrations, we chose a common investigation time window (15 to 30 minutes after LPA injection) across all concentrations.

We observed the fraction of spiking cells increases as we applied a higher concentration of LPA (Fig 4·2C). At low concentrations of LPA (10 nM and 100 nM), less than 20% of cells were spiking. As LPA concentration was increased to 1 μM and 10 μM, more than half the cells displayed calcium spiking. The effect of LPA appeared to saturate around 100 μM with 97% of cells spiking. We observed a uniquely large range of variability in the fraction of spiking cells incubated in 1 μM and 10 μM LPA, which is likely due to heterogeneity in individual cells' sensitivity to LPA activation at those concentrations [203].

We then investigated whether LPA concentration modulates calcium spiking frequency in fibroblast cells. The first feature we noticed was the large variation between individual cells within each LPA concentration, as is shown by the relatively large spread of spiking frequencies (Fig 4·2D). This large variability was previously observed in the same cell type under ATP stimulation [171, 56] as well as in other cell types in response to other ligands (for example, phenylephrine-induced calcium spiking in hepatocytes and CCh-induced calcium spiking in HEK cells [8]). LPA at a low concentration (100 nM) induced a mean calcium spiking frequency of around 10 mHz, and a slightly higher spiking frequency at intermediate concentrations (1 μM and 10 μM), around 12 mHz. As LPA concentration was increased to 100 μM, the mean spiking frequency increased to around 20 mHz. These results show that in 3T3 fibroblasts, although with high cell-cell variability, the frequency of calcium spiking is tuned by LPA concentration.

After establishing that LPA concentration modulates the fraction of spiking cells and spiking frequency, we tested whether it regulates spiking amplitude. Similar to spiking frequency, a prominent observation is that spiking amplitude displayed high cell-cell vari-

ability (Fig 4·2E). Nevertheless, we observed a significant increase in spiking amplitude on the population level with increasing LPA concentration (Fig 4·2E). The population-averaged amplitude increased 75% as LPA concentration increased from 100 nM to 1 μM, and 30% as LPA concentration increased from 10 μM to 100 μM (Fig 4·2E). The fact that there was no significant amplitude tuning at the sub-ten-micromolar concentration range suggests that amplitude encoding of calcium dynamics in response to different LPA concentrations is non-linear, and that there is potentially a regime (1 μM to 10 μM) where calcium spiking amplitude is robust to changes in LPA concentration. One caveat from our data is that because we used a single-color calcium reporter, despite normalized to baseline levels, the intensity does not reflect concentrations quantitatively. This caveat can be potentially addressed by expressing a constitutive fluorescent protein at the same level as the calcium reporter (similar approach adapted in [194]). In summary, our data showed LPA concentration modulates the fraction of spiking cells and spiking frequency, and there is large cell-cell variability in calcium spiking responses under the same environmental conditions. Our data also suggested potential amplitude modulation in calcium spikes by different concentrations of LPA.

4.2.3 LPA-induced calcium spiking requires extracellular calcium and is mediated by ER calcium release.

It is well established that LPA acts through GPCRs, which induce ER calcium release through IP_3 production [179]. This mechanism accounts for the LPA-induced single-pulse calcium response observed in astrocytes [11], keratinocytes [13], and human foreskin fibroblasts [12]. However, the mechanisms controlling repetitive calcium spiking, especially in the context of LPA-induced calcium spiking, are less well understood. To this end, we investigated potential calcium toolbox components that could mediate LPA-induced calcium spiking in 3T3 fibroblast cells.

Calcium in the cytosol is modulated by calcium exchange between two major stores,

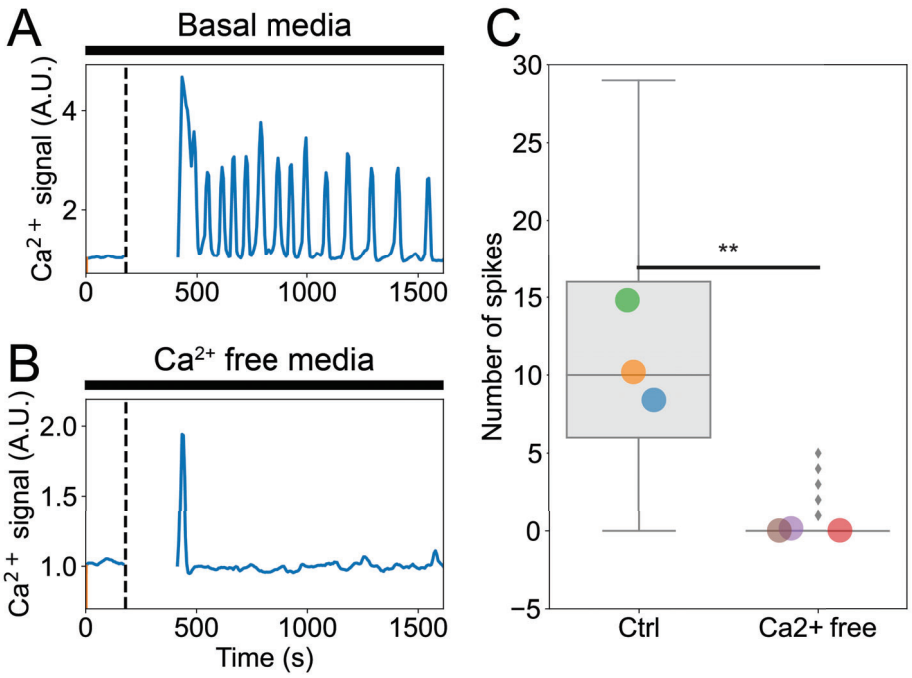

Figure 4·3: LPA-induced calcium spiking requires extracellular calcium. Calcium traces from example cells cultured in the basal media (**A**) and calcium-free media (**B**). At the black dashed line, 10 μM LPA was added to the media. (**C**) demonstrates the number of calcium spikes identified in the 20 minutes after LPA addition. Each dot represents average data from cells in an independent experiment, with the colors representing data from different experiments (cell seeding days). For the control media condition, n = 1135 cells from 6 wells were included. For the calcium-free media condition, n = 424 cells from 3 experiments were included. Box plots show data from individual cells, with the upper and lower bars representing the maximum and minimum value, box boundaries representing the 75th and 25th percentile, and the center bar representing the median of data. Grey diamonds mark outlier dells. Statistical tests between conditions were done with mean data from independent experiments with Games-Howell post-hoc test. ** $p<0.01$.

the intracellular store (endoplasmic reticulum, ER) and the extracellular space (Fig 4·4A, reviewed in [4, 5]). Generally, cytosolic calcium is maintained at around 0.1 μM, while the ER calcium (around 100 μM) and the extracellular calcium (around 1 mM) concentrations are at much higher levels. An increase in cytosolic calcium is usually mediated by the opening of channels such that calcium ions are able to freely diffuse along the concentration gradient, whereas a decrease in cytosolic calcium is generally mediated by molecular pumps that require energy consumption.

We first investigated whether extracellular calcium is required for LPA-induced calcium spiking. We incubated cells in calcium-free media and measured calcium dynamics in response to LPA treatment. Upon LPA addition, cells residing in the basal control media displayed repetitive spiking, with an average of 11.13 spikes in the 20-minute time window that we recorded. On the contrary, cells cultured in calcium-free media displayed an average of 0.079 spikes in the same time length, with the majority of cells either displaying a single spike or did not display any spikes at all. These results agree with literature that suggests the maintenance of ER calcium store requires extracellular calcium and that eliminating extracellular calcium drains the ER calcium store slowly over time [139]. This result confirms that extracellular calcium is required for LPA-induced calcium spiking.

We then investigated potential calcium toolbox components that could mediate or modulate LPA-induced calcium spiking dynamics. We primed the cells with 10 μM LPA, and then injected inhibitors targeting different molecular components from the calcium toolbox [4], (Fig 4·4A). The toolbox components that we tested include ones that mediate ER calcium release (IP_3R and sarco/endoplasmic reticulum Ca^{2+}-ATPase (SERCA) pump) and membrane calcium channels including stretch-activated calcium channels (SACCs) and voltage-gated calcium channels (VGCCs), all of which are expressed in 3T3 fibroblasts [204, 205]. Before drug addition, most cells displayed repetitive calcium spiking behavior. Upon drug addition, cells either continued repetitive spiking with possibly different spiking

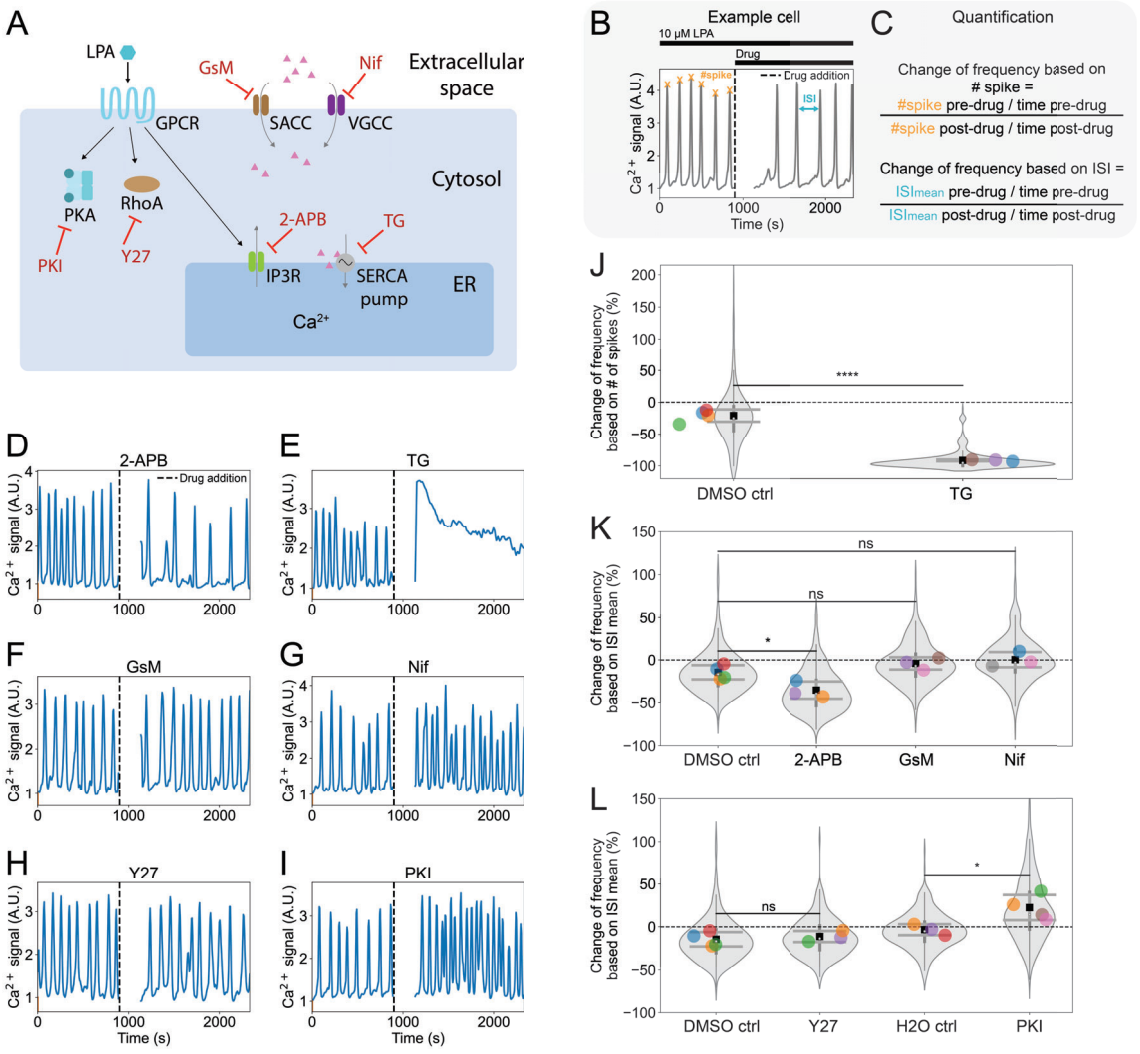

Figure 4-4: LPA-induced calcium spiking is mediated by ER calcium release and is shaped by PKA activity.

A. Graphical schematic showing calcium toolbox components [4] as well as other signaling molecules (PKA and RhoA) potentially involved in modulating calcium dynamics in response to extracellular LPA ligand. Inhibitor drugs used to test the role of different components are marked in red. Metrics used to quantify the change of calcium spiking behavior pre- and post-drug application are demonstrated in (**B**) and (**C**). (**B**) shows cytosolic calcium dynamics in an example cell in grey, with the black, dashed line marking the time point when the drug was applied, orange Xs marking the spikes, and blue arrow marking the interspike interval (ISI) between two spikes. Two ways of quantifying the change in calcium spiking behavior after and before drug addition (based on the number of spikes and based on the mean of ISI) are displayed in (**C**). (**D-E**) show example calcium traces with different types of inhibitor drugs (drugs added at the time point marked by black dashed line). Change of frequency based on the number of spikes upon thapsigargin (TG) addition is shown in (**J**). Change of frequency based on the interspike interval (ISI) with different calcium toolbox inhibitor drugs is displayed in (**K**), and that with either RhoA or PKA pathway inhibitor drugs is shown in (**L**). In (**J-L**), colored dots represent the mean metrics of cells from independent experiments (cell seeding days), with colors representing different experiments. Black squares and grey error bars demonstrate the mean and S.D. between the mean from independent experiments. The violin plots display data distribution from single cells, with white dots representing the median, thick black bars representing the interquartile range, and thin gray lines representing the rest of the distribution. Statistical tests between conditions are done with mean data from individual experiments with Tukey's HSD method for data with equal variance, and Games-Howell post-hoc test for data that does not show equal variance. * $p<0.05$, ****, $p<0.0001$, ns, not significant ($p>0.05$). TG, thapsigargin; GsM, GsMTx4; Nif, Nifedipine; Y27, Y27632; PKI, protein kinase inhibitor (14-22).

frequencies or respond with a single large calcium pulse (upon thapsigargin treatment, Fig 4·4E). To measure the percentage change in spiking frequency between after and before drug treatment, we used two metrics for the two types of responses. For drugs that did not eliminate repetitive spiking in most cells, we used the inverse of the mean of interspike intervals to calculate frequency; for drugs that eliminated repetitive spiking in most cells, we calculated frequency using the number of spikes per unit time (Fig 4·4B-C).

When treated with thapsigargin (TG) which inhibits ER calcium release by inhibiting the SERCA pump located on the ER membrane, cells displayed a single pulse of cytosolic calcium (Fig 4·4E), and no repetitive spiking was observed. This response is also reflected by an almost 100% decrease in spiking frequency after adding thapsigargin (Fig 4·4J). After the initial pulse, cytosolic calcium stayed at a relatively high level, possibly due to store-operated calcium entry induced by ER calcium depletion. This result matches those from the previous studies where thapsigargin induced a pulse of calcium concentration increase followed by prolonged high cytosolic calcium level (for example, [13, 17, 206]). To confirm whether IP_3-mediated ER release mediates LPA-induced calcium spiking, we treated the cells with IP_3 receptor inhibitor, 2-APB. Upon treatment, we observed an immediate decrease in spiking frequency (35.6% decrease on average from the pre-treatment values), which was significantly different from the control treatment case (14.0% decrease)(Fig 4·4D and K). These results confirm that ER-mediated calcium release is essential for modulating LPA-induced calcium spiking.

To investigate whether stretch-activated calcium channels (SACCs) and voltage-gated calcium channels (VGCCs) are involved in modulating LPA-induced calcium spiking, we used specific inhibitors GsMTx4 (for SACCs [207]) and nifedipine (for VGCCs). Calcium spiking persisted after the addition of both inhibitors (Fig 4·4 F-G). For both inhibitor treatments, we observed an average percentage change of frequency that was slightly smaller than the control treatment (Fig 4·4 K). However, neither the SACC inhibitor nor the VGCC

inhibitor induced a significant difference compared to control treatments (Fig 4·4 K). The result with nifedipine treatment matches previous work that shows VGCC inhibition in fibroblast cells only slightly alters the calcium dynamics induced by platelet-derived growth factor (PDGF), which is another extracellular ligand that induces ER-mediated calcium spiking [208]. In summary, we found that LPA-induced calcium spiking requires extracellular calcium and is mediated by IP_3- mediated ER calcium release. Our data also suggested that LPA-induced calcium spiking is not likely to be mediated by the activity of either stretch-activated calcium channels or voltage-gated calcium channels.

4.2.4 The cAMP/PKA pathway modulates LPA-induced calcium spiking

3T3 fibroblast cells express multiple subclasses of LPA receptors which can activate various types of G-proteins [187]. Activation of different G-proteins can lead to the activation of various downstream pathways including two pathways that have potential crosstalk with the calcium pathway, the RhoA pathway and the cAMP/PKA pathway [179]. The RhoA pathway is activated through $G\alpha_{12/13}$, whereas the cAMP/PKA pathway is activated through $G\alpha_s$. Previous sudies have shown that the RhoA pathway can modulate calcium dynamics by enhancing cell contractility through the RhoA-ROCK-myosin II axis [209, 210]. On the other hand, the cAMP/PKA pathway modulates cytosolic calcium by acting on various calcium toolbox components, usually by phosphorylation with PKA. Those components include IP_3R, stretch-activated calcium channels (SACCs), store-operated calcium entry (SOCE) channels [137, 138], and membrane pumps. Because these two pathways are activated by LPA in parallel with the calcium pathway, and they have been shown to modulate calcium activity, we hypothesize the activity of these two pathways might affect calcium dynamics induced by LPA.

To test whether the RhoA pathway and the cAMP/PKA pathway shape LPA-induced calcium spiking, we applied specific inhibitors of these two pathways, followed by quantification of the percentage change in frequency after and before drug treatment (Fig 4·4 B-C).

To inhibit the RhoA pathway, we chose Y-27632 (Y27) which directly inhibits the immediate downstream effector of RhoA, ROCK [211]. To inhibit the cAMP/PKA pathway, we chose the Protein Kinase A Inhibitor peptide (PKI) that has a much higher specificity compared to other PKA inhibitors [212, 213]. Upon RhoA pathway inhibition, we observed qualitative change in cell shape: cells shrunk in size and became star-like in shape, confirming the inhibitor worked as expected. However, we did not observe a qualitative change in calcium spiking behavior (Fig 4·4 H), nor did we observe a significant difference between the frequency change from cells treated with Y27 inhibitor or the control (Fig 4·4 L).

Interestingly, PKA inhibition with PKI induced a significant increase in spiking frequency, with the mean spiking frequency increased by 22% (Fig 4·4 I,L). This is surprising because canonically PKA is thought to be able to enhance ER calcium release by phosphorylating and sensitizing the IP_3 receptor on the ER. Previous work shows that activating the cAMP/PKA pathway speeds up calcium spiking rate in other ligand-induced calcium spiking cell culture models [8]. Along the same line, our own data shows direct activation of the cAMP/PKA pathway induces ER-mediated calcium release (Chapter 3). On the contrary, our data in this experiment suggest the cAMP/PKA pathway exerts an inhibitory effect on LPA-induced calcium spiking. In summary, we found that the cAMP/PKA pathway, but not the RhoA pathway, shapes LPA-induced calcium spiking. Our data suggest that in presence of LPA, PKA inhibits cytosolic calcium spiking.

4.3 Discussion

Here, we investigated cytosolic calcium dynamics under regular cell culture conditions using a fibroblast cell culture model. We found cells display repetitive calcium spiking behavior in the presence of serum, and further identified LPA as the major serum component responsible for inducing calcium spiking dynamics. By characterizing detailed features of

calcium spiking, we found that LPA concentration determined the fraction of spiking cells as well as population-averaged spiking frequency and amplitude. Through an inhibitor screen, we confirmed that LPA-induced calcium spiking requires extracellular calcium and is mediated by ER-calcium release. Additionally, we found that the cAMP/PKA pathway, which is also activated by LPA, shapes calcium spiking, suggesting that LPA-activated PKA exerts an inhibitory effect on cytosolic calcium. Although previous work has shown serum or LPA induces a single pulse of cytosolic calcium [13, 12], we took a unique focus on the repetitive spiking calcium dynamics induced by serum/LPA.

Our finding that the serum component LPA induces repetitive calcium spiking has important implications for studies about calcium signaling in standard cell culture media. We found that LPA concentration encodes multiple aspects of calcium spiking. Specifically, higher LPA concentrations increase the fraction of spiking cells, spiking frequency, and spiking amplitude. Decades of previous work have focused on how external cues (including biochemical cues and mechanical cues) modulate calcium dynamics. However, a significant fraction of these studies, especially those using cell culture models, was conducted under standard cell culture media conditions with serum supplement (example work includes [17, 170, 171, 172]). Because LPA receptors are expressed in numerous cell types and the molecular toolkit for calcium spiking exists across mammalian cell types [187, 4, 179], LPA-induced calcium spiking is expected to be observed in other mammalian cell types. This calls for attention to the presence of a bioactive molecule present in serum that induces and regulates calcium dynamics in a wide range of cell types. Our work suggests that past and future studies should be careful about interpreting calcium dynamics data in serum-supplemented media, and include proper controls to tease apart the effect induced by LPA.

We found that on the population level, calcium spiking frequency is positively tuned by LPA concentration. However, we notice a rather large cell-cell variation across all concen-

trations. This large variability has been reported in multiple existing works (for example, [171, 56, 8]). With this high level of cell-cell variability, two questions emerge. Firstly, what could be the origin of this variability? Secondly, how do cells reliably decode their environment through reading these variable calcium dynamics?

One possible origin of this variability is strong cell-cell communication due to high cell density and intrinsic noise within the signaling networks [56]. In our experiments, although the cell density was kept low enough such that cells usually have less than two neighbors, there were still patches of cells with relatively high density due to uneven seeding. Therefore, it is likely that a similar cell-cell communication mechanism contributes to the large cell-cell variability we observed.

In terms of how cells reliably encode extracellular ligand concentration with a signal with enormous cell-cell variability, a possible answer is that cells detect relative changes rather than the absolute levels of external ligand concentration. This mechanism successfully explained frequency tuning in response to ligand concentration change in multiple cell types and multiple ligand types previously [214, 8]. In the case of LPA-induced calcium spiking, whether a similar mechanism applies remains to be tested.

Matching what was shown in existing work that focused on a single calcium pulse induced by LPA (for example, [11, 13, 181, 12, 22]), we confirmed that IP_3-mediated ER calcium release accounts for LPA-induced calcium spiking. When investigating what other LPA-regulated pathways could shape LPA-induced calcium spiking, we found a surprising effect— calcium spiking speeds up upon PKA inhibitor addition—suggesting that the PKA pathway exerts inhibitory effects on cytosolic calcium. Our observation in Chapter 3, however, confirmed that activating the cAMP/PKA pathway can facilitate ER calcium release, a finding that matches the literature [8, 139]. To resolve this discrepancy, one potential explanation is compartmentalized regulation of the cAMP/PKA pathway in response to LPA. The cAMP/ PKA pathway can inhibit cytosolic calcium through phosphorylating and

activating either the SERCA pump which transports calcium into the ER, or the plasma membrane Ca^{2+} ATPase (PMCA) pump which transports cytosolic calcium to the extracellular space [215, 137]. Therefore, it is possible that LPA activates a subpopulation of PKA that acts dominantly on the SERCA pump and the PMCA pump, possibly by spatial compartmentalization. Upon phosphorylation by PKA, those pumps clear out cytosolic calcium faster, therefore inhibiting the calcium spiking rate.

Together, we identified a serum component, LPA, that accounts for serum-induced repetitive calcium spiking and characterized how LPA concentration is encoded in detailed features of the calcium dynamics. We also confirmed the calcium toolbox components that are responsible for regulating calcium spiking, and identified another LPA-induced signaling pathway that takes part in shaping the LPA-induced calcium spiking. Although we only systematically tested this phenomenon on one cell type, given the ubiquity of LPA receptor [179] as well as the universal presence of calcium toolbox components [4] across cell types, it is worth investigating whether this phenomenon exists in other cell types. It would also be interesting to explore differences in response and regulation between cell types and to relate these differences back to the differences in signaling networks.

4.4 Methods

Plasmid Construction

PCR fragments of jGCaMP7b were generated from pGP-CMV-jGCaMP7b (gift from Douglas Kim & GENIE Project, Addgene plasmid #104484, [173]), and gene fragments containing miRFP670 [157] and NES-T2A-H2B (Uniprot #B4DR52) were designed and purchased from Genewiz. The fragments were inserted into the pMJB001-PB-pCAG vector (gift from the laboratory of Dr. Wilson Wong) using NEB HiFi Assembly mix. Plasmids were sequence verified by Sanger Sequencing provided by Quintara Bioscience. The plasmid expressing the Piggybac transposase (pCag-Super-Piggybac) is a gift from the lab-

oratory of Dr. Wilson Wong.

Cell Culture and Reagents

NIH 3T3 fibroblasts (American Type Culture Collection, ATCC) were cultured from passages 1-12 in DMEM with 4.5 g/L glucose, L-glutamine, and sodium pyruvate (Corning), supplemented with 10% bovine serum (Gibco) and 1% penicillin-streptomycin (Invitrogen). Cells were maintained at 37°C and 5% CO_2 and passaged at 80-90% confluency with media changed every 2 to 3 days. PiggyBac Transposase system [154] was used to generate stable pools of sensor-expressing cells. Cells were plated and co-transfected with the constructs with jGCaMP7b-T2A-H2B-miRFP670 and Super PiggyBac Transposase at a ratio of 2:1 (w/w) DNA, respectively, using the Lipofectamine 3000 Transfection Reagent kit (Invitrogen) according to manufacturer's instructions. Stable pools were generated under selection with media supplemented with 2 μg/mL puromycin (Invivogen).

Preparation of charcoal-stripped serum media

Media containing charcoal-stripped serum was prepared following procedures described in [183, 185]. In brief, basal media was supplemented with 10% (v/v) bovine serum before being mixed with dextran-coated charcoal (Sigma). The mixture was incubated on a rotating apparatus overnight. After centrifugation of the mixture at 600g for 10 min, the supernatant was taken to go through a 0.45 μm filter and stored in the fridge.

Calcium Imaging and Microscopy

Changes in cytosolic calcium were recorded with live video microscopy. 24 hours before imaging, NIH 3T3 cells stably-expressing H2B-miRFP670 and jGCaMP7b were plated in growth media on glass-bottom 24-well plates at 30k cells / cm^2. 15 minutes before imaging, selection media was replaced with imaging media containing Fluorobrite DMEM (Gibco) supplemented with 1% Glutamax (Gibco). Imaging media was supplemented with either

varying concentrations of oleoyl-L-alpha-lysophosphatidic acid (LPA, Sigma-Aldrich), 3 different lots of 10% bovine serum (Gibco, Sigma, or Cytiva, lot number listed in the table below), or calcium-free DMEM (Gibco) for respective experiments. Cells were then moved to a stage-top incubator maintained at 37°C and 5% CO_2 (OKO Labs) and imaged through a 20X air objective on a Ti-2E Eclipse (Nikon Instruments) with Dragonfly Spinning Disk Confocal System (Oxford Instruments). Time-series images were acquired on an iXon 888 Life EMCCD camera (Oxford Instruments) through a 405/488/561/647 dichroic mirror (Chroma). For jGCaMP7b calcium sensor channel acquisition, an excitation laser/emission filter combination of 488nm/525nm was used. For H2B-miRFP670 nuclei channel acquisition, an excitation laser/emission filter combination of 637nm/698nm was used.

Drug Treatments

Pharmaceutical drugs were added to imaging wells using the following procedures. Imaging was paused, then half of the media volume was taken out from the imaging well, mixed with the drug, and added back in the well drop-wise to prevent mechanical perturbation to the cells. Imaging was resumed after 2 minutes. For experiments with calcium-free media, cells in the wells were rinsed twice with calcium-free PBS and then incubated in calcium-free media for 40 minutes to 1 hour before imaging.

Data Processing and Analysis

Cell segmentation and tracking

Time courses from each experiment were converted to TIF files using Fiji [155]. Individual cells in the time series were segmented and tracked with the Trackmate plugin [216, 217] integrated with the open-source machine-learning based software Cellpose [218], with segmentation running through a NVIDIA RTX A4000 GPU. Batch processing was run through Fiji with a custom-written Jython script. Only cells that were tracked

throughout the whole time series were included in the next steps of analysis.

Calcium dynamics analysis

Data analysis was conducted with custom-written scripts in Matlab (Mathworks Inc.) and open-source software Python [156]. Calcium dynamics in individual cells were measured by the mean sensor channel intensity based on segmentation over time. Raw intensity traces were normalized to the average intensity before LPA injection (for Fig.4·2, Fig C·3, and 4·3) or the minimum intensity of the first 2 minutes of acquisition (for the remaining figures). Spike detection was conducted using the built-in peak-finding algorithm in the Scipy package [159]. Peak-finding metrics were empirically chosen, and peaks were required to have 0.3 minimum prominence, 30-second minimum distance between peaks, and 180-second maximum width. In Fig 4·1, cells that have more than 3 detected spikes over a 12-minute time course were considered “spiking". Peak prominence is quantified as the average prominence of the detected spikes, and only spiking cells are included in this analysis. Because the spiking frequency is based on the average inter-spike interval, only cells that display more than 3 spikes are included for frequency quantification.

Cells and Cell Culture

Name	**Manufacturer**	**Lot/ Batch Number**
MDCK (NBL-2)	ATCC	70040764
DMEM	Corning (10013CV)	3142008
EMEM	ATCC (Catalog No. 30-2003)	80304222
Calcium Free DMEM	Gibco (21-068-028)	2302078
Glutamax	Gibco (35-050-061)	N/A
Penicillin-Streptomycin	Gibco (15140122)	2321129
Fluorobrite DMEM	Gibco (A1896701)	N/A
Bovine Serum Lot 1	Gibco (16170086)	1861237
Bovine Serum Lot 2	Sigma (B9433)	17M479
Bovine Serum Lot 3	Cytiva HyClone (SH30073.04HI)	AF29689085
Fetal Bovine Serum	Gibco	10457436
Charcoal Stripped Fetal Bovine Serum	Gibco (A33821-01)	2437548

Chemical Reagents

Name	Manufacturer	Lot Number
Oleoyl-L-α-lysophosphatidic acid sodium salt (LPA)	Sigma-Aldrich (L7260)	SLCG1241
GdCl3	Acros Organics (AC383560050)	A0388697
LaCl3	Sigma-Aldrich (262072)	MKCL3175
2-APB	Santa Cruz (sc-201487)	I1120
Thapsigargin	Invitrogen (T7458)	2403704
Y-27632	Hello Bio (HB2297)	E1039-1-1
U-73122	Sigma-Aldrich (U6756)	0000125649
Nifedipine	Sigma-Aldrich (N7634)	MKCL4570
PKI	Santa Cruz (sc-471154)	D0722
H89	Abcam (ab120341)	GR3296093-29
cAMPs-Rp	Hello Bio (HB0165)	E0627-1-1
Manganese(II) chloride	Sigma (M1787)	SLBW2106

Chapter 5

Conclusions

Understanding how cells use intracellular signaling to detect environmental changes and coordinate behaviors is of paramount importance to understanding a wide range of biological processes. Major gaps in knowledge include the regulation and role of dynamical changes in signaling molecules as well as how intracellular signals coordinate behaviors in multicellular contexts. Here, we applied theoretical and experimental approaches to study cell signaling processes that involve dynamical signaling or multicellular coordination.

In **Chapter 2**, we used theoretical modeling to identify the key network features that coordinate population cAMP signaling oscillations in the social amoebae, *Dictyostelium discoideum* (*Dicty*). We first selected five representative models describing the general coordinated population oscillation behavior. To be able to directly compare models against each other and against experimental data, we applied time scale and amplitude scale normalization as well as single-cell-based simulation frameworks on all the models. Through a systematic comparison between models and data, we suggested that the key single-cell level features that coordinate population-wide cAMP oscillations in *Dicty* are adaptive spiking in response to a step input and fold-change detection. Broadly, because coordinated oscillations and waves are widely observed in biology (for example, oscillatory YAP waves during vertebrate segmentation [90] and Cdk1 waves that synchronize cell cycles across large spatial scales [91]), the lessons we learned here can potentially be applied to understanding these systems as well.

We then focused on experimentally delineating the decoding of mammalian cell mi-

gration in response to transient activation of the cAMP pathway (**Chapter 3**). Harnessing an optogenetic tool, we achieved transient, reproducible, and tunable control of the cAMP pathway. We found that repetitive activation of the cAMP pathway inhibited migration in a dose-dependent manner in both fibroblast cells and epithelial cells. By characterizing single-cell level responses, we found that transient activation of the cAMP pathway induced a decrease of cellular forces accompanied by structural alteration of the actin cytoskeleton. We further identified one of the major mediators for the actin cytoskeleton reorganization as cytosolic calcium. These single-cell level results suggest that calcium-mediated actin cytoskeleton reorganization could account for the inhibitory effect of cAMP activation on cell migration. This work provides new insights into how transiently activated cAMP pathways modulate cell behaviors related to migration.

Lastly, we experimentally interrogated how cytosolic calcium dynamics in fibroblasts are encoded by serum supplement in culture media (**Chapter 4**). By measuring calcium dynamics using a genetically-encoded calcium reporter in different media conditions, we found serum supplementation in culture media induced trains of calcium spiking. We then identified one of the key serum components responsible for calcium spiking to be lysophosphatidic acid (LPA). Our results showed that LPA concentration modulates the fraction of spiking cells as well as the frequency of calcium spiking, and can potentially modulate the amplitude of calcium spiking. Using inhibitors that target different calcium sources and other signaling pathways that are parallelly activated by LPA, we found that LPA-induced calcium spiking in fibroblasts is mediated by calcium release from the endoplasmic reticulum (ER). Our results also suggested that the cAMP/PKA pathway plays a role in shaping LPA-induced calcium spiking. Our work provides a detailed characterization and mechanistic interrogation of LPA-induced calcium dynamics and informs future work on calcium dynamics to take note of the effect of this serum-borne component.

5.1 Future directions

Theoretical investigation in **Chapter 2** provided a unifying framework that allowed us to investigate the essential single-cell network features that *Dictyostelium* cells use to coordinate population cAMP oscillations. What is worth noting is that for all the models, we took a mean-field approach that neglets space and time for extracellular signal propagation. However, naturally, the signaling process happens without well-mixing and there is significant spatial heterogeneity in the environment (for instance, from soil particles around the cells and uneven diffusion efficiencies based on the heterogeneity in the moisture content of the soil). Investigating mechanisms that are essential for determining the cAMP signal spatial pattern in these more naturalistic contexts is an important future direction. Previous modeling work has proposed several mechanisms that modulate cAMP spatial patterns such as waves and spirals [61, 219, 220, 221, 222, 77, 223, 224]. However, it is still not clear what are the essential features both on single-cell signal processing and extracellular signal molecule turnover that determine the formation and dynamical features of the spatial patterns. The simulation framework we developed can be applied to interrogate these related questions.

In **Chapter 3**, we showed transient, direct activation of the cAMP pathway inhibits cell migration in a monolayer of migrating cells. Interrogation on single cells suggested that migration inhibition could be a result of changes in actin cytoskeleton structure and reduction in cell contractility. However, how single-cell level responses relate to changes in migratory behavior in a group of cells remains to be investigated. Simultaneously visualizing cell contractility/actin cytoskeleton structure and cell migratory behaviors (direction, velocity) could be a starting point of such investigation. Additionally, our work in **Chapter 3** showed cytosolic calcium mediates the actin cytoskeleton reorganization. Future work on the mechanisms underlying how calcium induces actin cytoskeleton reorganization would provide an additional piece of information that helps us understand cell behaviors upon

transient cAMP pathway activation.

In **Chapter 4**, we investigated the environmental encoding of calcium dynamics in response to serum component LPA. Our data showed that calcium dynamics display high cell-cell variability. It would be interesting to investigate the origin as well as the biological implications of this variability. Previous work has shown that cell-cell communication could potentially explain the variability [225], and that the fold difference of the external ligand is reliably encoded in the signal-to-noise ratio of calcium dynamics. Therefore, one possible future direction would be investigating the role of cell-cell communication and ligand concentration fold-change in the context of LPA-induced calcium spiking. Further, a surprising result from **Chapter 4** is that cAMP/PKA pathway inhibition enhanced LPA-induced calcium spiking. Further investigation into the mechanism driving this observation would offer more insights into the crosstalk between calcium and the cAMP/PKA pathway.

5.2 Concluding perspectives: theory-experiment interplay

In this Dissertation, theoretical and experimental approaches are used separately to study cell signaling in eukaryotic systems. Although the theoretical and experimental approaches use different sets of techniques, they are usually reinforced by one another. Theoretical models depend on data generated by experiments to formulate assumptions and quantitative descriptions of the process of interest. Additionally, the best way to verify a theory is by testing its predictions using experiments. Conversely, because models usually take a quantitative description of the mechanisms and use mathematical reasoning, they can be used to verify whether a mechanistic understanding can explain the experimental data. More importantly, models can be used to distinguish alternate mechanisms by generating falsifiable predictions based on different mechanisms that can be tested using experiments. The most powerful understanding can come from the tight interplay between the two approaches (an idea proposed in multiple reviews, for example, [41, 226, 43, 44]).

Such interplay has been shown to be powerful in understanding the mechanisms driving coordinated cAMP signaling oscillations in the cellular slime mold (textitDicty) cells. Because cells use dynamic changes of the signaling molecule cAMP and cell-cell communication to coordinate group-wide oscillations, it is challenging just to use qualitative models to test the validity of specific mechanisms and to distinguish different mechanisms. Theoretical models were constructed to check the validity of mechanisms such as desensitization of the surface receptor [227] that are suggested by previous experiments. Experimental measurements have also inspired the construction of models which suggests new important mechanisms such as noise in single cells [62, 228]. Additionally, as is shown in **Chapter 2**, systematic analysis of models guides the design of new experiments that could distinguish different mechanisms as is shown by the models. This type of tight interplay between experiments and models will continue to yield insights and deepen understanding of processes coordinated by cell signaling.

Appendix A

Appendix: supplementary information for Chapter 2

Model Details and Assumptions

I. Receptor Desensitization model

One of the earliest and most widely used models of population-level cAMP oscillations in *Dictyostelium* was developed by Martiel and Goldbeter [71] in response to the experimental observation that the cAMP receptor CAR1 is desensitized as external cAMP concentration increase [229, 230]. In this model, cells detect external cAMP using the cAMP receptor CAR1 (*R* in Figure 2·1), leading to the production and release of internal cAMP into the environment. As external cAMP concentrations increase, a negative feedback loop is triggered that leads to receptor desensitization and a corresponding decrease in internal cAMP production and excretion. This well-understood mechanism based on a negative feedback loop (i.e. receptor desensitization) with a time delay that naturally leads to population-level oscillations [231].

II. Coupled Direct and Indirect Negative Feedback (CDINFB) model

The authors of Maeda, et al. [73], building on earlier works including the Laub-Loomis model [72], developed a detailed mechanistic model of the *Dictyostelium* signal relay net-

work. In this model, external cAMP binds to the CAR1 receptor (*R* in Figure 2·1), leading to production of internal cAMP by the enzyme adenylyl cyclase (ACA, shown as *A* in Figure 2·1). The activation of ACA also triggers a pair of coupled negative feedback loops: a direct negative feedback mediated through protein kinase A (PKA, shown as *I* in Figure 2·1) that turns off cAMP production, and an additional indirect negative feedback mediated by the proteins RegA and ERK2 that activates PKA, once again leading to decrease in cAMP production. Additionally, the ERK2-RegA path leads to internal cAMP decrease through RegA acting as a internal phosphodiesterase that degrades cAMP.

III. Phenomenological Phase Oscillator model

Inspired by new experiments showing that even isolated single cells can oscillate in response to elevated levels of external cAMP, the authors of Gregor et al. [62] constructed a phenomenological model inspired by the Kuramoto model [232, 233] where the *Dictyostelium* signaling network is modeled as a phase-oscillator, with the phases of different cells coupled through the external cAMP concentration. Internal cAMP concentrations are assumed to be directly proportional to the *sine* of the phase of the oscillator.

IV. Interlocking Positive-Negative Feedback (IPNFB) model

This phenomenological model introduced in Sgro, et al. and expanded on in Noorbakhsh, et al. [63, 77] captures the key behaviors of the *Dictyostelium* signaling network using a generalization of the FitzHugh Nagumo (FHN) model, which commonly used in neuroscience to model excitable neural dynamics [79, 78]. The model consists of two elements: an activator species (*A*) and an inhibitor species (*I*). The presence of external cAMP leads to increased production of the activator species, suggested to be representa-

tive of adenylyl cyclase activity, which can trigger a fast positive feedback loop that results in even more activator production. The activator also triggers a slower negative feedback by producing an inhibitor species that suppresses production of the activator, though this inhibitor species is suggested to be representative of a larger network structure and not a specific molecular species. In this model, internal cAMP concentrations are assumed to track the activator concentration, with cells releasing cAMP into the environment when the activator is above a certain threshold.

V. Incoherent Feedforward Loop (IFFL) model

Like the IPNFB model, the incoherent feedforward loop (IFFL) model is a phenomenological model of the *Dictyostelium* signaling network that combines fast activation with inhibition on longer time scales inspired by the experimental observations in Kamino, et al. [74]. In the IFFL model, the receptor up-regulates both the activator (A) as well as the inhibitor species (I). Crucially, while the inhibition varies linearly with the concentration of external cAMP, the activator exhibits a Hill-like (sigmoid-like) kinetics in response to external cAMP concentrations. This model displays interesting behaviors in the single-cell context including fold-change detection [84, 80] and perfect adaptation [81].

VI. Model assumptions

Finally, we note that an important but subtle difficulty involved in comparing and contrasting these models with experiments is that they make very different assumptions about how the models are related to experimental observables. Model parameters are often specified in arbitrary units, so it is *a priori* unclear how to relate predictions across the five models. To address this problem, we chose to non-dimensionalize both the amplitudes and timescales of internal cAMP responses in terms of the height and width of the adaptive spike induced by one unit of external cAMP input in single cells. In almost all of the models cells respond to a small, sudden change in external cAMP by producing a spike of internal cAMP. The

height of this spike in each model gives a natural scale for measuring internal cAMP amplitudes whereas the width represents a natural time scale for normalizing times between models (see *Materials and Methods* for details).

Model Equations and Parameters

Note: Variable names in this section are as presented in the original literature. Some variable names in Figure 2·1 are renamed in order to emphasize which species act as different network components that may be common between models.

I. Receptor Desensitization model

The Receptor Desensitization model [71] is composed of three differential equations. $\rho_{T,i}$ and β_i denote the proportion of receptors in the active state and internal cAMP concentration in the ith cell,and γ stands for external cAMP concentration.

$$\frac{d\rho_{T,i}}{dt} = -f_1(\gamma)\rho_{T,i} + f_2(\gamma)(1-\rho_{T,i}) \tag{1}$$

$$\frac{d\beta_i}{dt} = q\sigma\Phi(\rho_{T,i},\gamma,\alpha) - (k_i + k_t)\beta_i \tag{2}$$

$$\frac{d\gamma}{dt} = k_t/h\frac{\sum^N \beta_i}{N} - k_c(\gamma - [cAMP]_{e,in}) \tag{3}$$

with:

$$f_1(\gamma) = \frac{k_1 + k_2\gamma}{1+\gamma}, \tag{4}$$

$$f_2(\gamma) = \frac{(k_1L_1 + k_2L_2c\gamma)}{1+c\gamma} \tag{5}$$

$$\Phi(\rho_{T,i},\gamma,\alpha) = \frac{\alpha(\lambda\theta + \varepsilon Y^2)}{1+\alpha\theta+\varepsilon Y^2(1+\alpha)} \tag{6}$$

$$Y = \frac{\rho_{T,i}\gamma}{1+\gamma} \tag{7}$$

$[cAMP]_{e,in}$ stands for cAMP concentration that is added externally and this notation is used across all models.

Parameter values are from Table II of the original literature[71]. Specifically, $k_1 =$

0.036, $k_2 = 0.666$, $L_1 = 10$, $L_2 = 0.005$, $c = 10$, $\lambda = 0.01$, $\theta = 0.01$, $\varepsilon = 1$, $q = 4000$, $k_i = 1.7$, $k_t = 0.9$,$k_c = 5.4$, $h = 5$, $N = 100$.

In Figure 2·4B, cell density and external cAMP degradation rates are varied by altering $\frac{1}{h}$ and k_c .

Time normalization parameters for the Receptor Desensitization model is 6.94, and its height normalization parameter is 210.53.

II. Coupled Direct and Indirect Negative Feedback (CDINFB) model

The CDINFB model represents a signaling network consisting of seven molecular species [73]. Within a population of N cells, respective concentrations of the biochemical species in the ith cell follow:

$$\frac{d[ACA]_i}{dt} = k_1[CAR1]_i - k_2[ACA]_i[PKA]_i \tag{8}$$

$$\frac{d[PKA]_i}{dt} = k_3[cAMP]_{cyt,i} - k_4[PKA]_i \tag{9}$$

$$\frac{d[ERK2]_i}{dt} = k_5[CAR1]_i - k_6[PKA]_i[ERK2]_i \tag{10}$$

$$\frac{d[RegA]_i}{dt} = k_7 - k_8[ERK2]_i[RegA]_i \tag{11}$$

$$\frac{d[cAMP]_{cyt,i}}{dt} = k_9[ACA]_i - k_{10}[RegA]_i[cAMP]_{cyt,i} \tag{12}$$

$$\begin{aligned}\frac{d[cAMP]_e}{dt} =& \rho k_{11}\frac{\sum^N[ACA]_i}{N} \\ & -k_{12}([cAMP]_e - [cAMP]_{e,in})\end{aligned} \tag{13}$$

$$\frac{d[CAR1]_i}{dt} = k_{13}[cAMP]_e - k_{14}[CAR1]_i \tag{14}$$

Parameters are $k_1 = 2, k_2 = 0.9, k_3 = 2.5, k_4 = 1.5, k_5 = 0.6, k_6 = 0.8, k_7 = 1.0, k_8 = 1.3, k_9 = 0.3, k_{10} = 0.8, k_{11} = 0.7, k_{12} = 4.9, k_{13} = 23, k_{14} = 4.5, \rho = 1, N = 100$.

In Figure 2·4C, cell density and external cAMP degradation rates are varied by altering ρ and k_{12} .

Time normalization parameters for the CDINFB model is 3.57, and its height normalization parameter is 3.15.

III. Phenomenological Phase Oscillator model

The Phase Oscillator model [62] considers each cell as a phase oscillator coupled by cAMP in the external medium. $[cAMP]cyt,i$ and θ_i denote the internal cAMP concentration and internal phase of the ith cell. Equations describing $[cAMP]cyt,i$ dynamics, θ_i, and external cAMP $[cAMP]_e$ are:

$$[cAMP]_{cyt,i} = \frac{(-A_{max}+A_{bas})\sin\theta_i + A_{max} + A_{bas}}{2} \tag{15}$$

$$\frac{d\theta_i}{dt} = \omega(1-\Phi([cAMP]_e)c_{excite}sin\theta_i) \tag{16}$$

With $\Phi([cAMP]_e) = \frac{K}{K+[cAMP]_e}$

$$\begin{aligned}\frac{d[cAMP]_e}{dt} =& \rho\frac{S_T V_C}{V_T S_C}c_{sec}\frac{1}{N}\sum^{N}[cAMP]_{cyt,i} \\ &- \frac{k}{Vt}([cAMP]_e - [cAMP]_{e,in})\end{aligned} \tag{17}$$

Parameter values are from the original paper [62]. Specifically, $A_{max} = 20, A_{bas} = 0.4, \omega = \pi/3, V_C = 1.1\cdot 10^{-9}, S_T = 1.33, S_C = 1.3\cdot 10^{-6}, K = 0.0004, c_{sec} = 3.6, c_{excite} = 1.01, N = 100, k = 5, \rho = 1/12, k = 5, V_t = 1$.

In Figure 2·4D, cell density and external cAMP degradation rates are varied by altering ρ and k .

Time normalization parameters for the Phase Oscillator model is 6, and its height normalization parameter is 19.6.

IV. Interlocking Positive-Negative Feedback (IPNFB) model

In the IPNFB model [63, 77], the signaling network in each cell is modeled following the FitzHugh-Nagumo framework [79]. The internal cAMP concentration and internal inhibitor concentration are represented by A_i, R_i. Equations describing A_i, R_i and external $cAMP_e$ dynamics are:

$$\frac{dA_i}{dt} = A_i - \frac{1}{3}A_i^3 - R_i + I([cAMP]_e) \tag{18}$$

$$\frac{dR_i}{dt} = \varepsilon(A_i - \gamma R_i + c_0) \tag{19}$$

$$\frac{d[cAMP]_e}{dt} = [cAMP]_{e,in} + \rho\alpha_0 + \rho S\frac{1}{N}\sum^{N}\Theta(A_i) - (J+\alpha_{PDE})[cAMP]_e \quad (20)$$

With $I([cAMP]_e) = a \cdot log(1+\frac{[cAMP]_e}{K_d})$, and $\Theta(A_i)$ being the Heaviside function: equal to 1 if $A_i > 0$ and otherwise equal to 0. Parameter values are from the original paper [63]. Specifically, $\varepsilon = 0.1, \gamma = 0.5, c_0 = 1.2, N = 100, \alpha = 0.058, \alpha_0 = 800, \alpha_{PDE} = 1000, K_d = 10^{-5}, S = 10^6, \rho = 10^{-3.5}, J = 0.5$. An offset of 1.5 is applied to A_i traces before outputs are height-normalized.

In Figure 2·4E, cell density and external cAMP degradation rates are varied by altering ρ and J .

Time normalization parameters for the IPNFB model is 27, and its height normalization parameter is 3.5.

V. Incoherent Feedforward Loop(IFFL) model

For the IFFL model [74], there are two key molecular players in each cell: an activator y_i that approximates internal cAMP concentration and an repressor x_i that represents internal inhibitor concentration. Equations describing y_i, x_i and external $cAMP_e$ dynamics are:

$$\frac{dx_i}{dt} = \frac{1}{\tau}([cAMP]_e + \delta - x_i) \quad (21)$$

$$\frac{dy_i}{dt} = \frac{([cAMP]_e + \delta)^n}{([cAMP]_e + \delta)^n + (Kx_i)^n} - y_i \quad (22)$$

$$\frac{d[cAMP]_e}{dt} = \rho k_t y_i - \gamma([cAMP]_e - [cAMP]_{e,in}) \quad (23)$$

δ is included for lower detection limit. Parameter values are from the original paper [74]. Specifically, $\tau = 1.5, n = 2, K = 4, k_t = 2, \delta = 0.01, \gamma = 3, \rho = 0.01, N = 100$. An offset of 0.058 is applied to y_i traces before outputs are height-normalized.

In Figure 2·4F, cell density and $cAMP_e$ degradation rates are varied by altering ρ and γ.

The time normalization parameter for the IFFL model is 5.23, and its height normaliza-

tion parameter is 0.26.

Supplementary Figures

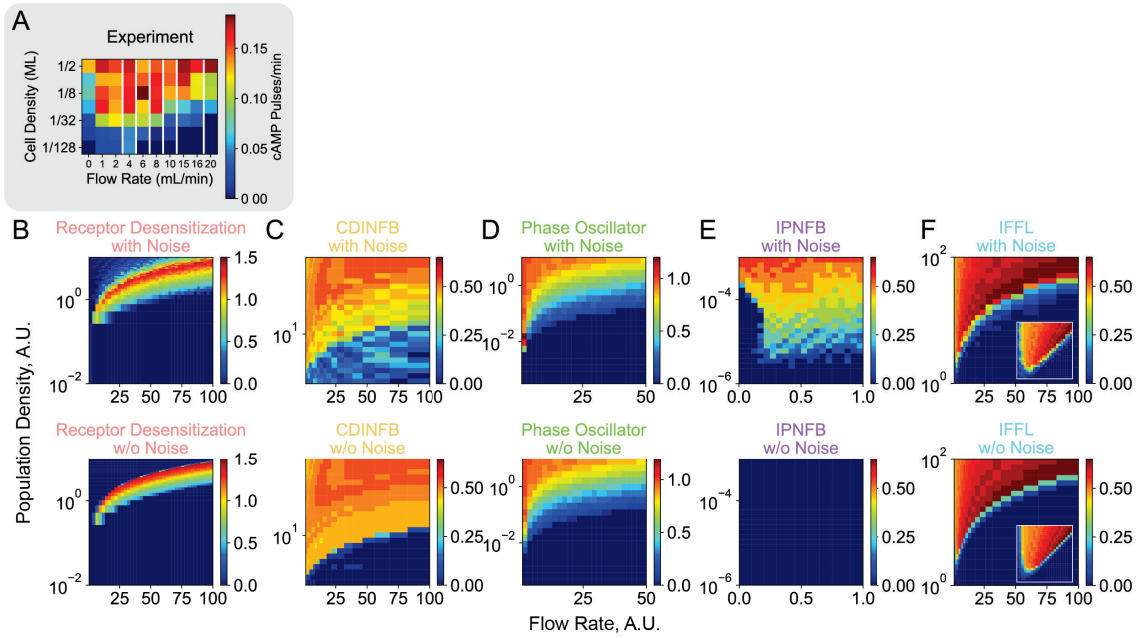

Figure A·1: The role of noise in the emergence of population-wide oscillations. **(A)** Experimental population firing rate phase diagram for *Dictyostelium* cells in a flow chamber with varying media flow rates and cell densities measured in fractions of a monolayer (ML) from Gregor, et al. [62]. **(B to F)**. Simulation results for all of the different models, with the upper panels displaying the results including single cell noise as shown in Figure 2·4, and the lower panels omitting single cell noise. Inset of **(F)** shows the same model output plotted with a logarithmic x-axis.

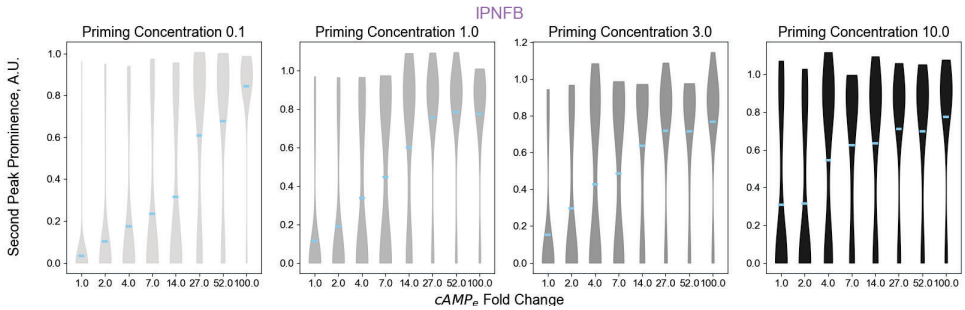

Figure A·2: Probability density of IPNFB fold-change detection responses. The IPNFB model has built-in single-cell noise so each simulation results in a different single-cell internal cAMP response. For each priming concentration-fold change pair, the means of the second-peak prominence (also shown in Figure 2·6C) are plotted as blue bars and the probability distributions are in shades of gray.

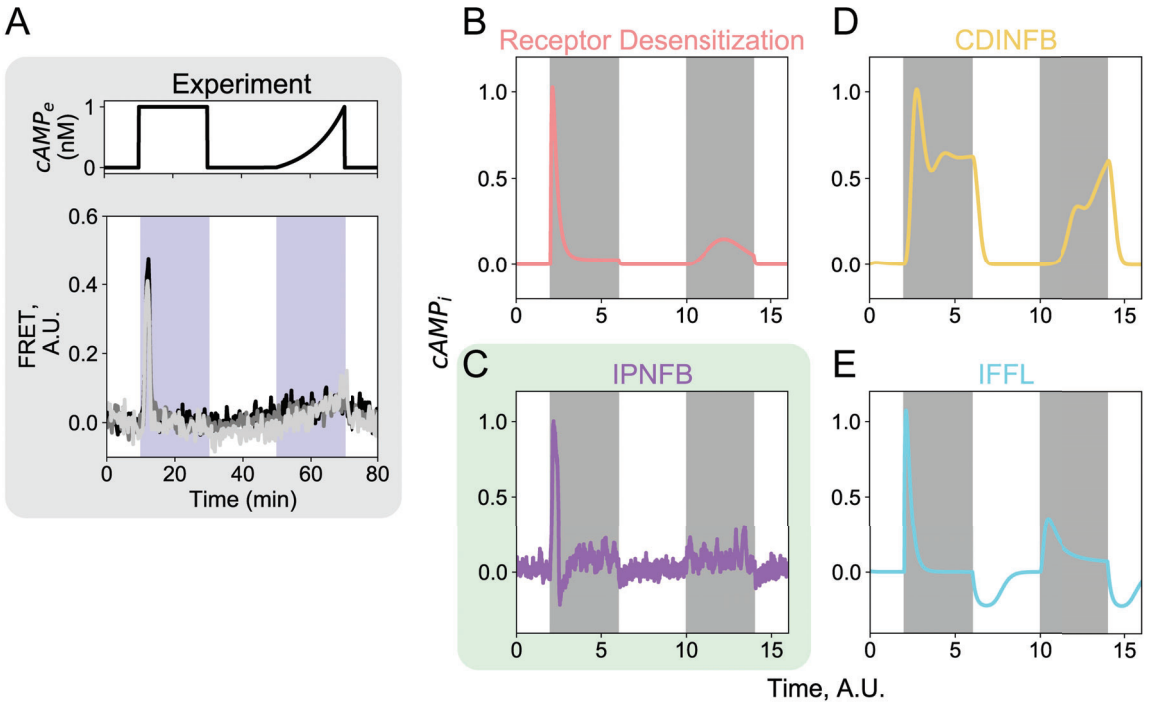

Figure A·3: Different models have different internal cAMP responses to $[cAMP]_e$ input dynamics. (A) Experimental data show single *Dictyostelium* cells display an internal cAMP spike in response to an abrupt 1 nM step input of external cAMP but remain mostly quiescent in response to a slow ramp input to 1 nM external cAMP. Data adapted from Sgro, et al. [63]. Top panel: external cAMP input temporal profile. Bottom panel: Experimental $[cAMP]_i$ traces from three example cells. **(B - E)** Model simulations of cell responses. The first and second shaded region denotes when the step and exponential ramp $[cAMP]_e$ inputs are applied respectively. The maximum concentration of external cAMP input in each model is the same as in Figure 2·5C. A gray shaded background behind the plots highlights experimental data. A green shaded background indicates models that reproduce the experimental observations.

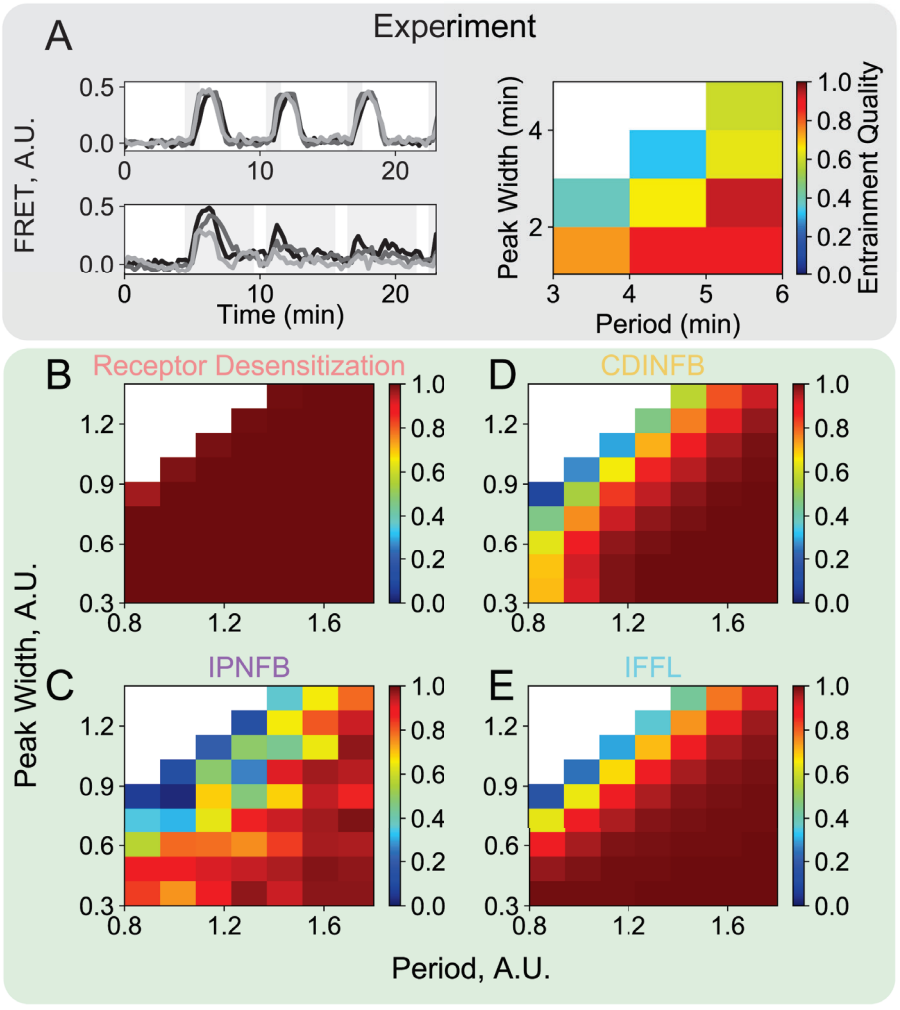

Figure A·4: Entrainment quality varies with $[cAMP]_e$ input cycle period and input peak width.

Experimental measurements adapted from Sgro, et al. [63] of how cells respond to repetitive external cAMP stimuli with different input peak widths and with different input cycle periods. This data illustrates single cells are entrainable and have a refractory period. Entrainment quality is quantified as the average Pearson's cross correlation coefficient of each of the subsequent $[cAMP]_i$ response spikes compared against the first response spike. **(A)** Left panel: $[cAMP]_i$ traces for three example cells experiencing a step input to 10 nM external cAMP. Shaded region indicates external cAMP input. Right panel: Entrainment quality increases with longer stimulation period and briefer peak width. **(B - E)** Model simulations show that all models that display adaptive spiking, even if not fully adaptive (Figure 2·5C), qualitatively match the experimental data. However, the entrainment quality metric does not take into account height variation between the first and subsequent spikes. The Receptor Desensitization model scores highly with this entrainment quality metric across the parameter regime we probe, but the spike height is reduced in some regimes indicating it has a refractory period (**B**). Based on what is used in experimental data, stimulation period and peak width is sampled from 0.8-1.8 and 0.4-1.4 times the respective timescale normalization parameter for each model. We set external cAMP input concentrations in each model to the same values as in Figure 2·5C. A gray shaded background behind the plots highlights experimental data. A green shaded background indicates models that reproduce the experimental observations.

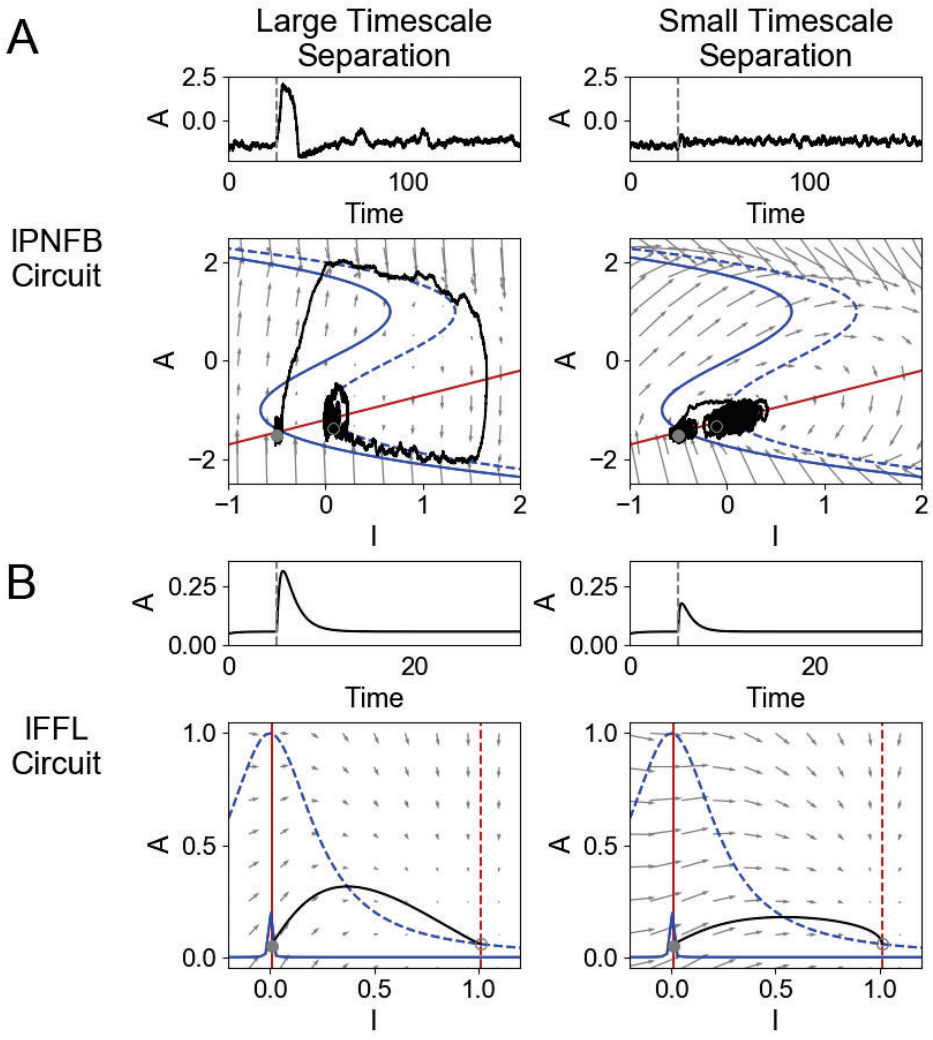

Figure A·5: The effect of decreasing timescale separation on the single-cell response to step inputs.

Activator (approximating internal cAMP level) response traces and nullcline analysis with different timescale separation parameters in the IPNFB circuit **(A)** and the IFFL circuit **(B)**. Left and right panels show model activator responses for large (IPNFB $\varepsilon = 0.1$, IFFL $\tau = 1.5$) and small (IPNFB $\varepsilon = 1$, IFFL $\tau = 0.5$) values of the time scale separation parameter between the activator (A) and inhibitor (I) species, respectively. In simulations, we applied one unit of external cAMP at the gray dashed line. Solid black lines show how the activator trajectory in the phase plane. Solid gray dots and gray circles mark the initial and end states of the systems. Solid and dashed blue lines are activator nullclines before and after external cAMP input. Solid and dashed red lines are inhibitor nullclines before and after external cAMP input. Gray lines with arrows display vector fields of the systems. Both models are displayed in their native units from the original publications and given in *Model Equations and Parameters*

Appendix B

Appendix: supplementary figures for Chapter 3

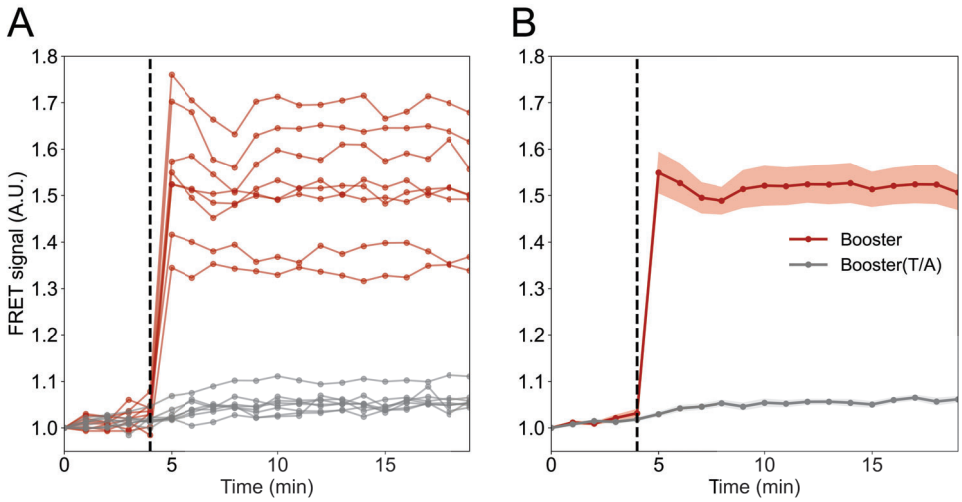

Figure B·1: PKA-Booster sensor validation. FRET signal from the PKA-Booster sensor (orange traces) or the non-responsive control sensor Booster (T/A) (grey traces) upon stimulation with the adenylyl cyclase activator forskolin. Traces of individual cells are shown in (**A**). The mean and S.E.M. of each sensor construct are shown in (**B**). n = 8 cells for each construct are included. At the black dashed line, 10 μM forskolin is applied.

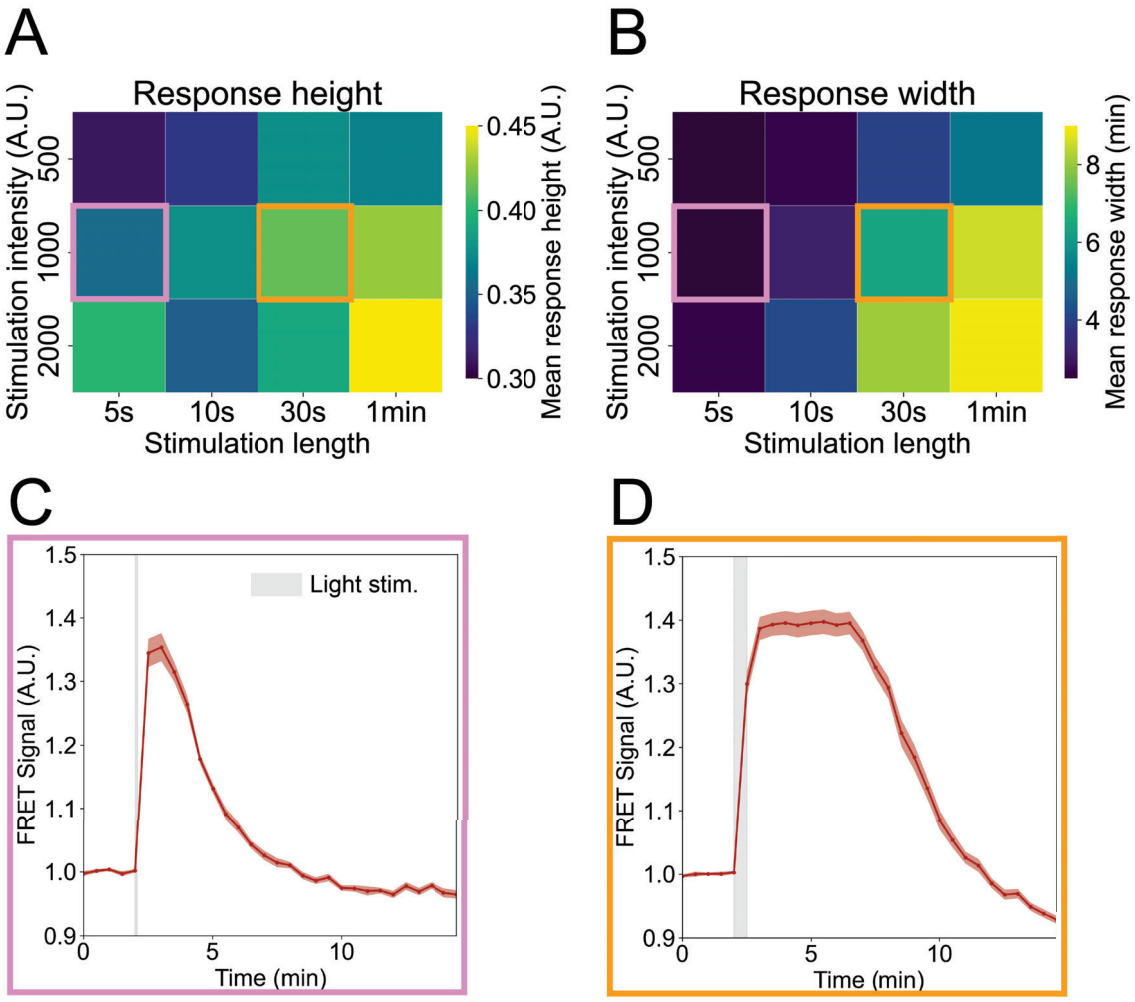

Figure B·2: Booster sensor is saturated at high light stimulation dose in cells expressing the bPac construct. PKA-Booster reporter signal height (**A**) and width (half max height width, (**B**)) in response to different light stimulation duration and intensity, with heatmap colors corresponding to the mean from multiple cells. The signal traces are normalized to the baseline average before calculating the height and widths. For each photostimulation condition, n = 12 to 21 cells are included. Light stimulation was conducted using the 465 nm LED on the Optoplatesystem [109]. Mean and S.E.M. from single-cell response traces with light stimulation dosages marked with the pink and orange squares are shown in (**C**) and (**D**), respectively. At the grey-shaded regions, light stimulation was turned on.

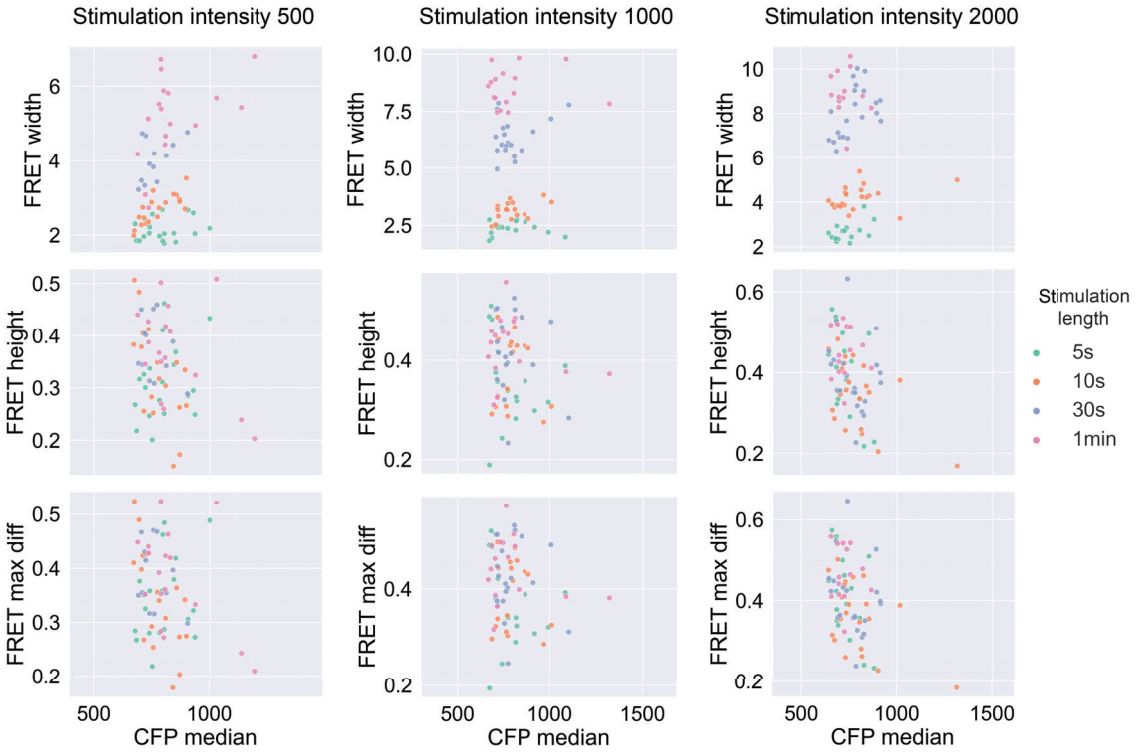

Figure B·3: bPac- induced PKA activation is not dependent on the expression level of the bPac construct. Each column shows the FRET signal (from the PKA-Booster reporter) width, height, and maximum difference from baseline with a scatter plot with median CFP intensity, which acts as an approximation of the bPac construct expression level. Each column shows data from a different stimulation intensity. Each dot represents a response from a single cell, and different colors represent different stimulation lengths (5 seconds, 10 seconds, 30 seconds, 1 minute). The baseline of the signal traces is normalized to the baseline signal before stimulation. For each photostimulation condition, n = 12 to 21 cells are included.

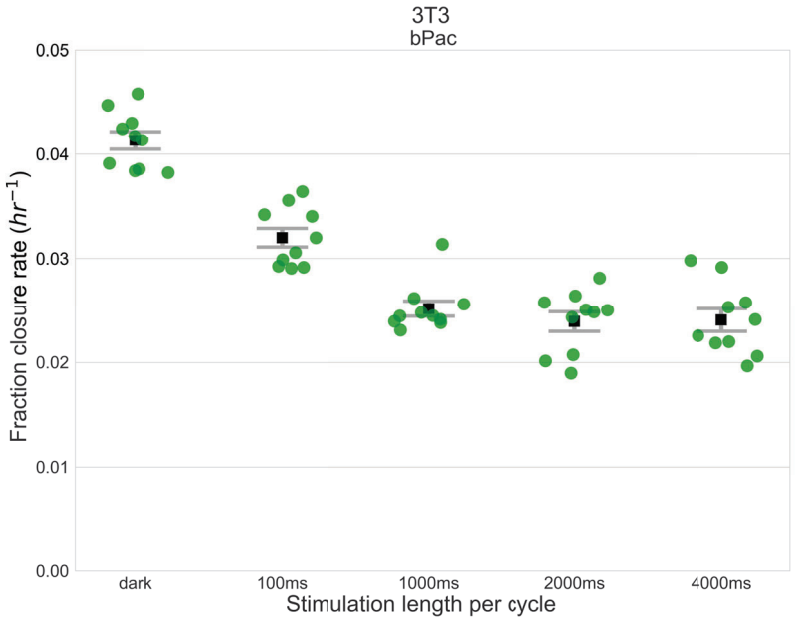

Figure B·4: bPac's inhibition effect on two-dimensional cell migration plateaus at high activation dosage (stimulation length). Percentage area closure rate was quantified with different light stimulation lengths (dark, light on for 100ms, 1000ms, 2000ms, and 4000ms every 5 minutes) in 3T3 fibroblasts expressing the bPac optogenetic construct (bPac-mTurquoise2-NES). Each colored dot represents an independent well. Black square dots and gray bars represent mean and S.E.M. 10 independent wells are included for each condition.

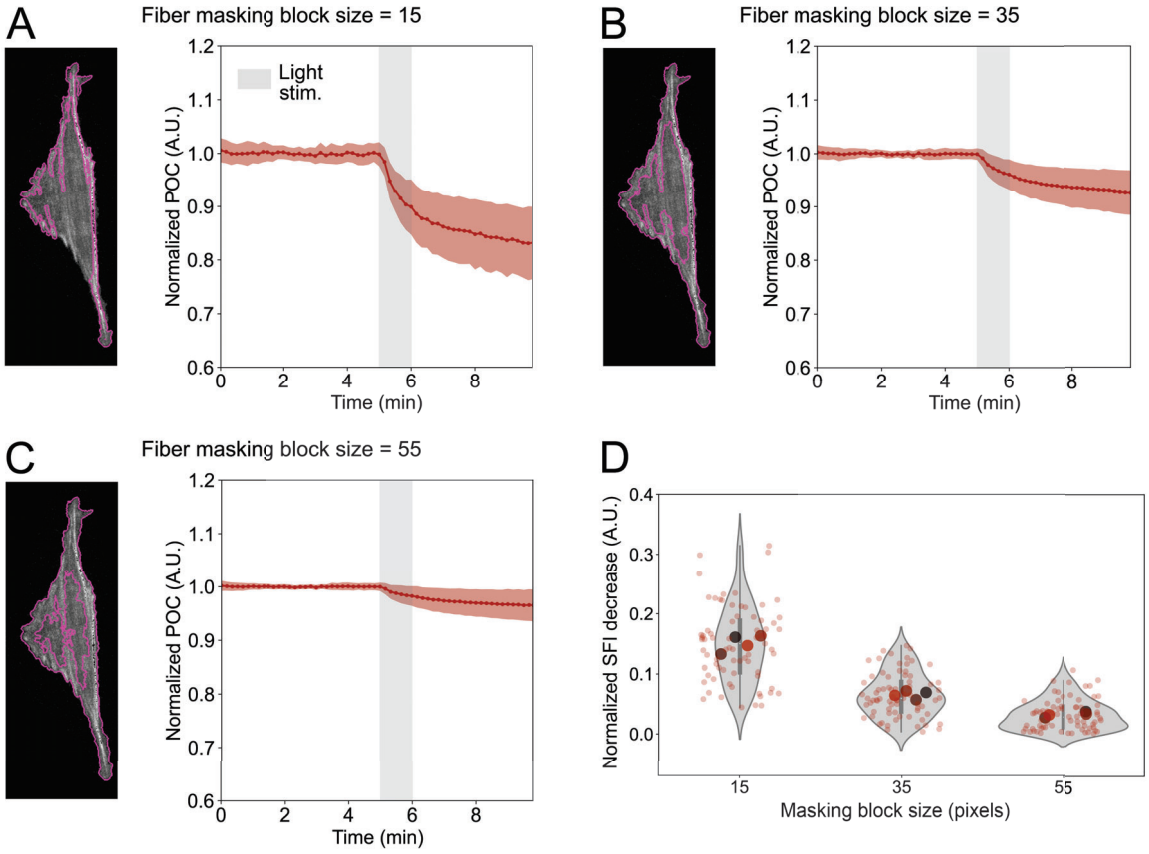

Figure B·5: The fiber integrity metric SFI is sensitive to masking parameter. In (**A**) to (**C**), the stress fiber mask (boundary shown in pink) overlaid on top of an example image of a cell is on the left, and the average and S.D. of stress fiber integrity of multiple cells are shown on the right. On the right panels, the grey-shaded regions mark the start to the end of the light stimulation. (**D**) shows the maximum decrease of normalized SFI after bPac activation with different fiber masking block sizes. In the violin plot, white dots represent the median, thick black bars represent the interquartile range, and the thin gray line represents the rest of the distribution. Large colored dots show average values within the same experiment (well), and small colored dots show data from single cells, with colors denoting different experiments. Cells express the LifeAct-mIRFP670 marker for tracking actin fiber structure and the bPac construct. n = 73 cells are included. 490 nm LED at 10% power is used for light stimulation.

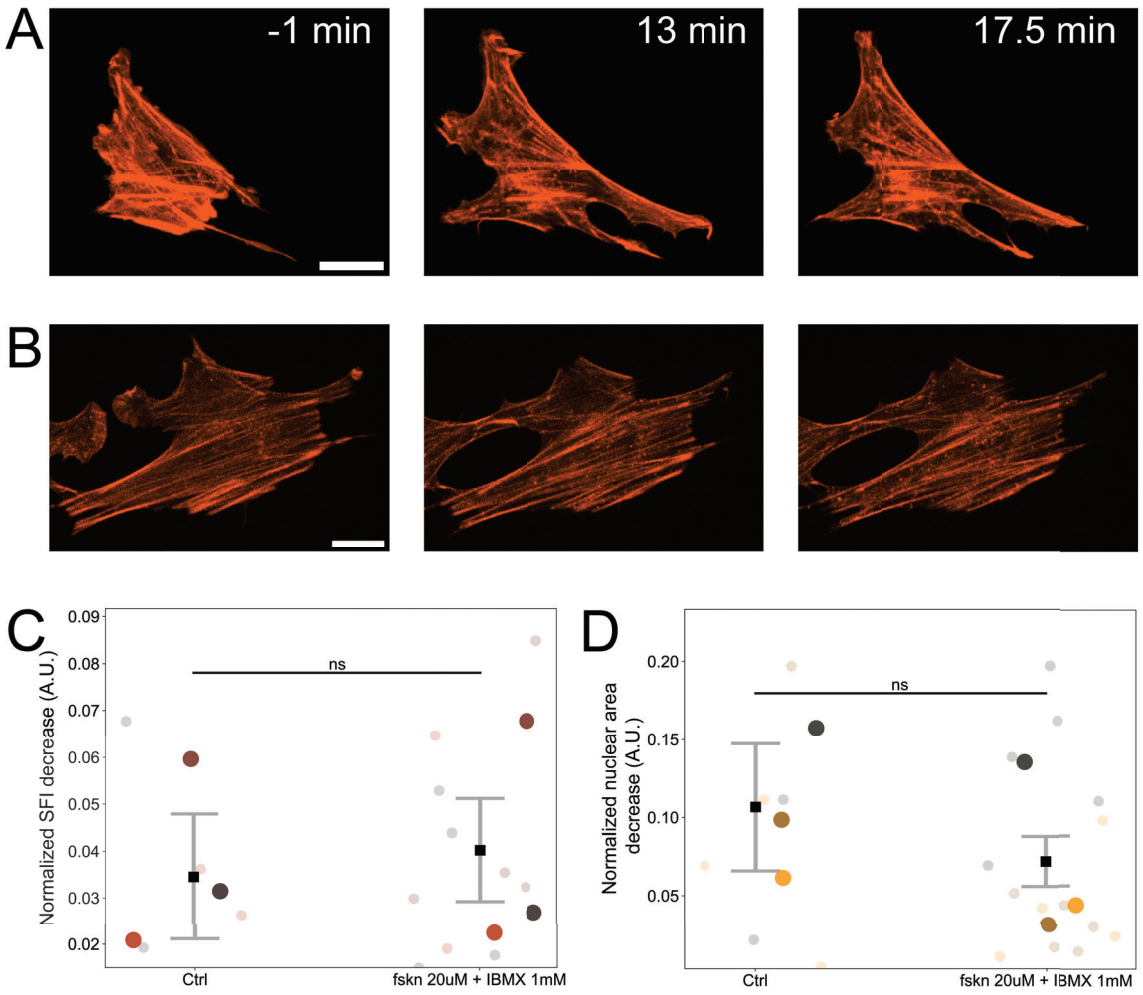

Figure B·6: Pharmaceutical activation of the cAMP pathway does not induce a similar rapid change in the stress fiber structure. (**A**) and (**B**) show actin markers from two example cells at 1 minute before adding cAMP activating cocktail (20 μM adenyl cyclase activator forskolin and 1 mM PDE inhibitor IBMX), 13 and 17.5 minutes after drug addition. Cells are labeled with actin cytoskeleton marker LifeAct-mScarlet (I) and the optogenetic tool bPac. A red light was used during drug injection to avoid activation of the tool. Scale bars = 20 μm. Maximum fractional decrease of SFI and nucleus area are shown in (**C**) and (**D**), with each large colored data point representing the mean value from an independent experiment (cell seeding day). n = 14 and 8 cells are included for drug (fskn 20 μM + IBMX 1mM) and control (DMSO) treatments respectively. Student t-test is used for testing between-group differences of single cells. ns: not significant.

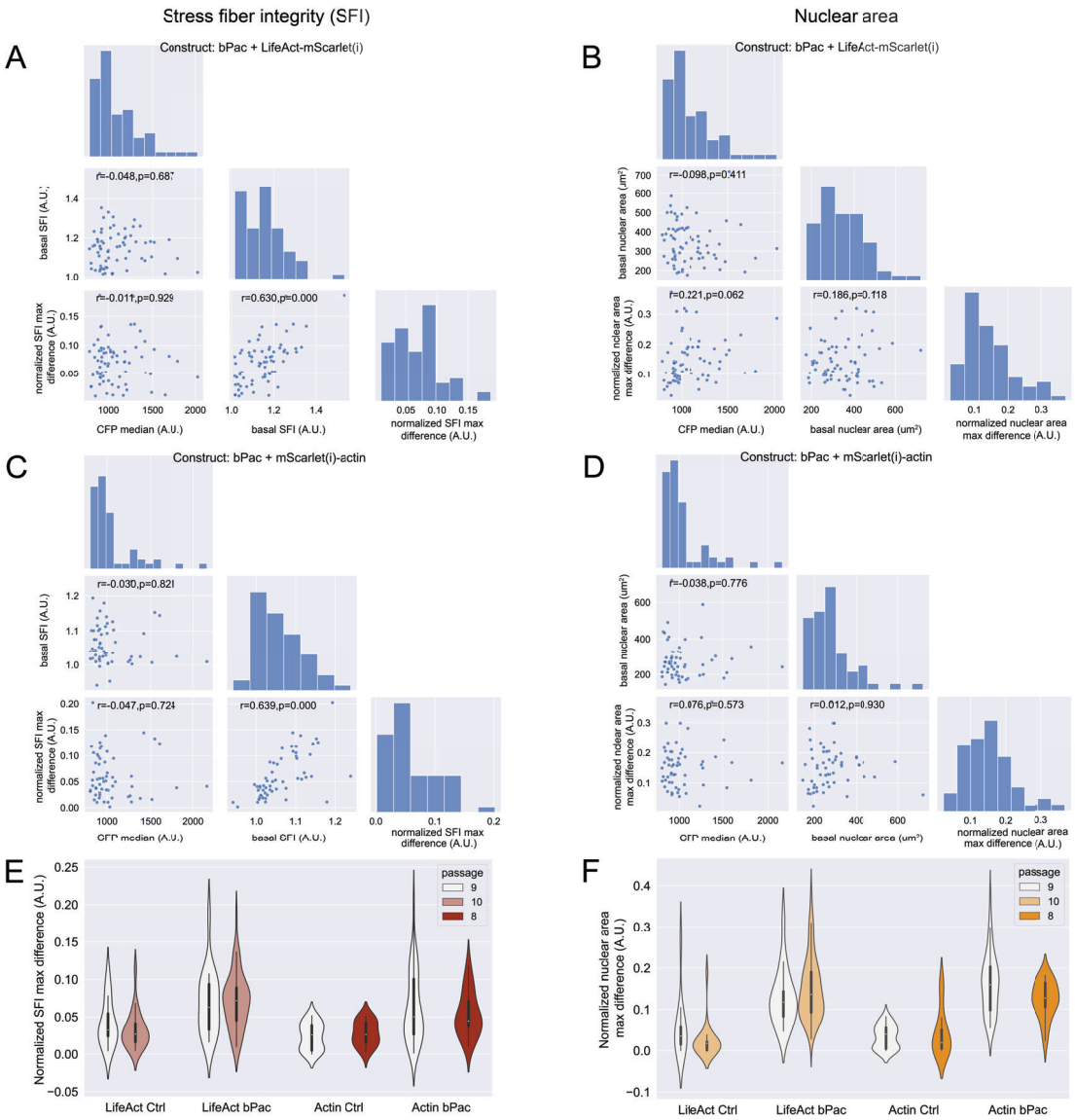

Figure B·7: Investigating potential correlation between SFI/ nucleus area decrease and bPac tool expression level, basal levels of the metrics, and cell passage.

(**A**) and (**C**) show scatter plots to investigate potential correlations between the expression of the bPac tool (CFP median), normalized SFI decrease (normalized SFI difference) after bPac stimulation, and the basal SFI level. (**B**) and (**D**) show scatter plots between the expression of the bPac tool (CFP median), normalized nucleus area-decrease upon bPac stimulation (normalized NA difference), and the basal nucleus area (basal NA). Pearson correlation coefficient r and corresponding p values (rounded to three decimal places) are displayed on the graphs. In (**A**) and (**B**), cells express the bPac construct and the LifeAct-mScarlet(i) marker or the mScarlet(i)-actin marker, respectively. (**E**) and (**F**) show violin plots of normalized SFI decrease and normalized nucleus area decrease with different passages, in which white dots represent the median, thick black bars represent the interquartile range, and the thin gray line represents the rest of the distribution.

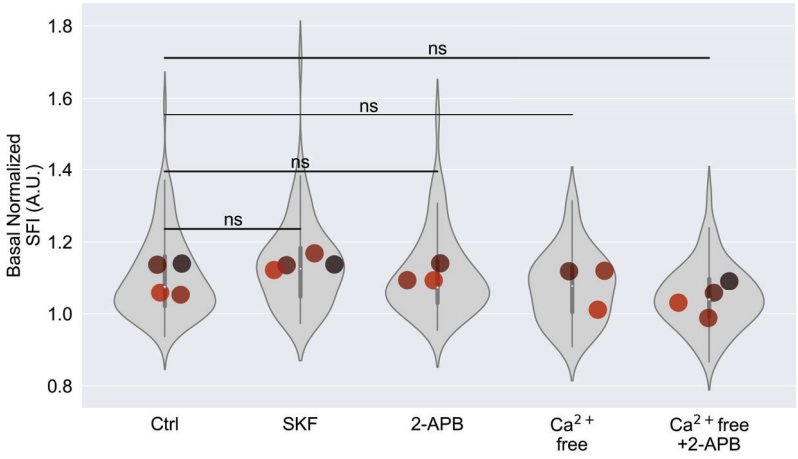

Figure B·8: Calcium inhibiting treatments do not significantly alter the basal level of stress fiber integrity (SFI). Basal stress-fiber integrity (SFI) measurement is displayed for different calcium inhibitor conditions. The large colored data points represent the mean value from an independent experiment (cell seeding day), with colors representing different experiments. The violin plots show the distribution of the basal SFI in individual cells, with white dots representing the median, thick black bars representing the interquartile range, and thin gray lines representing the rest of the distribution. Statistical tests between conditions are conducted between independent experiments with Tukey's HSD method for data with equal variance and Games-Howell post-hoc test for data that does not show equal variance. ns: not significant. Statistical results are only calculated between the control media and other treatment conditions.

Appendix C

Appendix: supplementary figures for Chapter 4

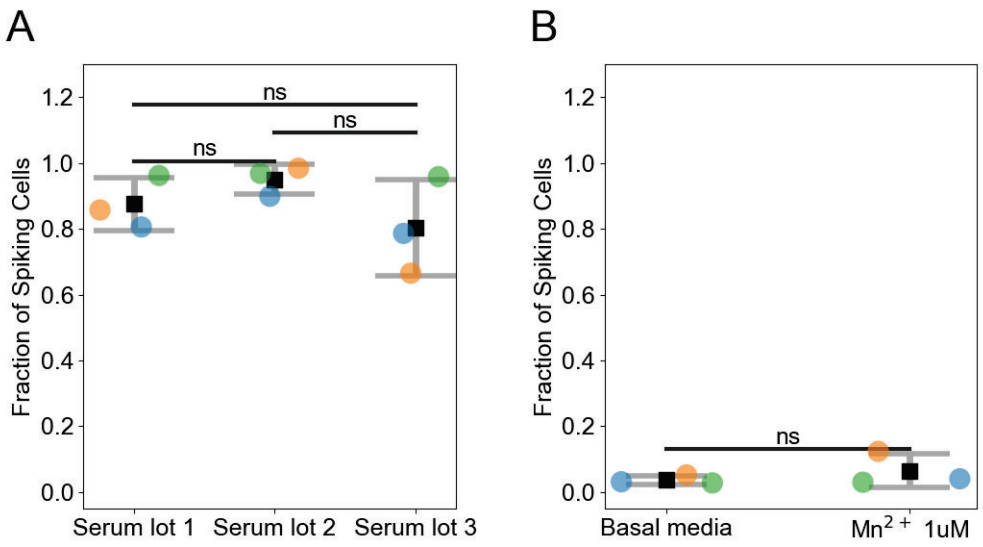

Figure C·1: Serum induces calcium spiking in most cells across 3 different serum lots, and serum-induced spiking is not rescued by Mn^{2+} supplement. (**A**) Serum induces calcium spiking in most cells across 3 different serum lots. For each serum lot, n = 760, 621, and 351 cells were included. For each condition, data is from 3 independent experiments (cell seeding days). (**B**) Very few spiking cells are observed in basal media and basal media supplemented with 1 μM Mn^{2+}. n = 829 cells in basal media condition and 931 cells in Mn^{2+} condition were included. In both (**A**) and (**B**), colored dots represent the mean from independent experiments (cell seeding days), with the colors representing different experiments. Black squares and error bars represent the mean and S.D. between experiments. Statistical tests between conditions are done with Tukey's HSD method for data with equal variance and Games-Howell post-hoc test for data that does not show equal variance. ns, not significant, ($p>0.05$).

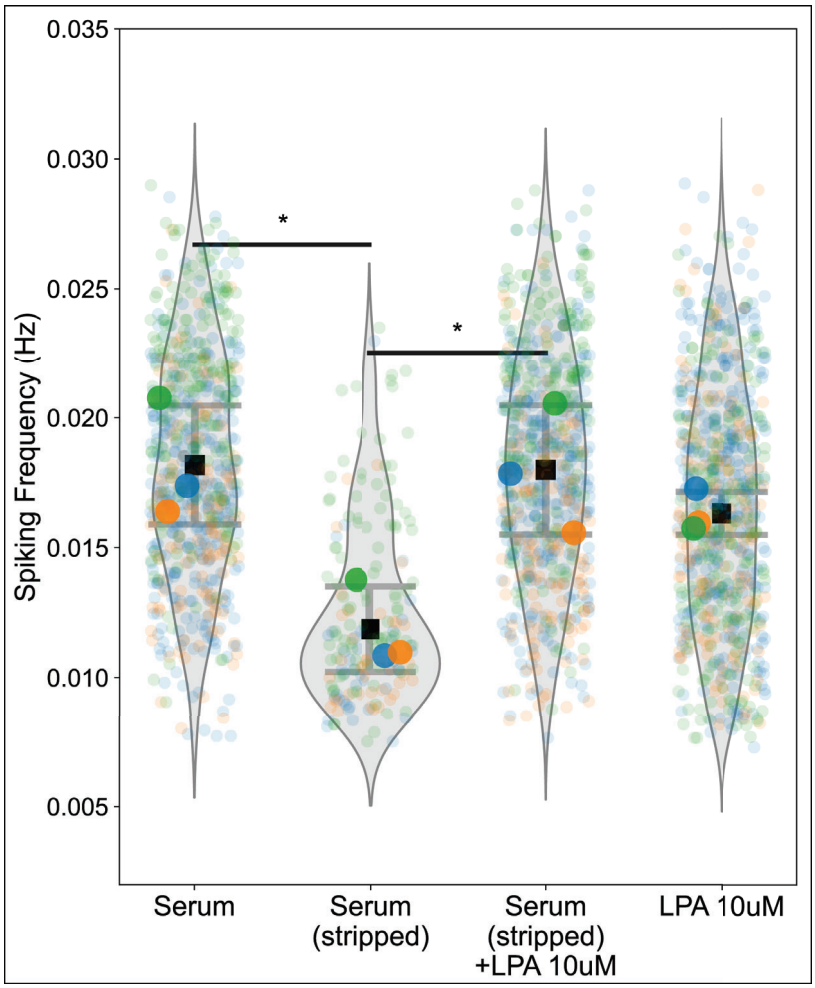

Figure C·2: The serum component LPA tunes calcium spiking frequency in 3T3 fibroblast cells. Calcium spiking frequency was calculated by the mean of inter-spike interval in different media conditions: media supplemented with serum, charcoal-stripped serum, charcoal-stripped serum with 10 μM LPA, and 10 μM LPA alone. For each condition, n = 662, 180, 661, and 727 cells were included across 3 independent experiments (cell seeding days). Small colored dots represent the frequency of single cells, and large colored dots represent the mean from cells in each experiment, with the colors representing different experiments. Black squares and error bars represent the mean and S.D. between different experiments. Statistical tests were conducted with data from the means of independent experiments. Tukey's HSD method was used for data with equal variance and Games-Howell post-hoc test was used for data that does not show equal variance. * $p<0.05$. The significance value is not marked for condition pairs that do not show a significant difference.

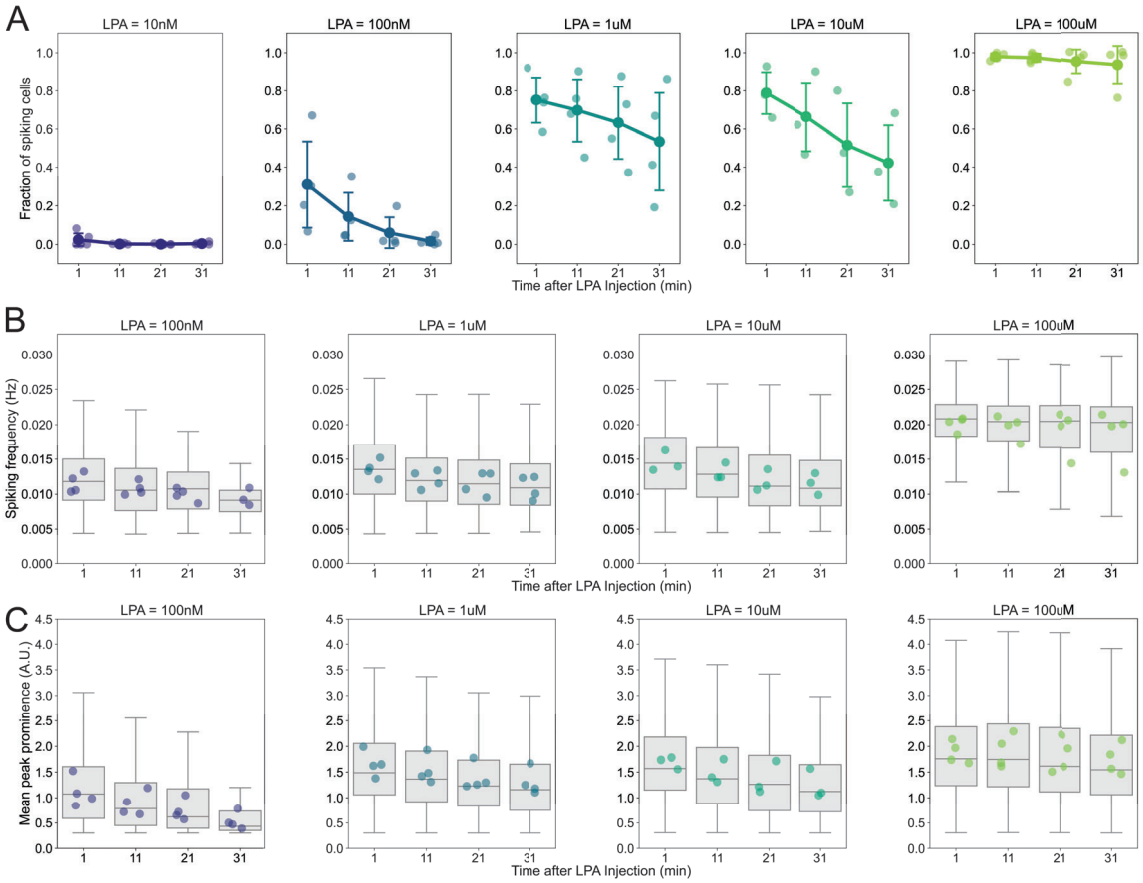

Figure C·3: Both LPA concentration and time after LPA addition both modulate calcium spiking. Fraction of spiking cells (**A**), spiking frequency (**B**), and mean prominence of normalized spikes (**C**) are modulated by LPA concentration (10 nM, 100 nM, 1 μM, 10 μM, 100 μM) as well as time after LPA injection. Each dot represents average data from cells from an independent experiment. In (**A**), squares and error bars represent the mean and S.D. from different experiments. In (**B**) and (**C**), box plots show data from individual cells, with the upper and lower bars representing the maximum and minimum value, box boundaries representing the 75th and 25th percentile, and the center bars representing the median of data.

Bibliography

[1] Azeloglu, E. U. & Iyengar, R. Signaling Networks: Information Flow, Computation, and Decision Making. *Cold Spring Harbor Perspectives in Biology* **7**, a005934 (2015).

[2] Antebi, Y. E., Nandagopal, N. & Elowitz, M. B. An operational view of intercellular signaling pathways. *Current Opinion in Systems Biology* **1**, 16–24 (2017).

[3] Lim, W. A. Designing customized cell signalling circuits. *Nature Reviews Molecular Cell Biology* **11**, 393–403 (2010).

[4] Berridge, M. J., Bootman, M. D. & Roderick, H. L. Calcium signalling: dynamics, homeostasis and remodelling. *Nature Reviews Molecular Cell Biology* **4**, 517–529 (2003).

[5] Clapham, D. E. Calcium Signaling. *Cell* **131**, 1047–1058 (2007).

[6] Wacquier, B., Voorsluijs, V., Combettes, L. & Dupont, G. Coding and decoding of oscillatory Ca2+ signals. *Seminars in Cell & Developmental Biology* **94**, 11–19 (2019).

[7] Handly, L. N., Pilko, A. & Wollman, R. Paracrine communication maximizes cellular response fidelity in wound signaling. *eLife* **4**, e09652 (2015).

[8] Thurley, K. *et al.* Reliable Encoding of Stimulus Intensities Within Random Sequences of Intracellular Ca2+ Spikes. *Science Signaling* **7**, ra59–ra59 (2014).

[9] Courtney, A. H., Lo, W.-L. & Weiss, A. TCR Signaling: Mechanisms of Initiation and Propagation. *Trends in Biochemical Sciences* **43**, 108–123 (2018).

[10] Trebak, M. & Kinet, J.-P. Calcium signalling in T cells. *Nature Reviews Immunology* **19**, 154–169 (2019).

[11] Nadal, A., Fuentes, E., Pastor, J. & McNaughton, P. A. Plasma albumin is a potent trigger of calcium signals and DNA synthesis in astrocytes. *Proceedings of the National Academy of Sciences* **92**, 1426–1430 (1995).

[12] Jalink, K., van Corven, E. J. & Moolenaar, W. H. Lysophosphatidic acid, but not phosphatidic acid, is a potent Ca2(+)-mobilizing stimulus for fibroblasts. Evidence for an extracellular site of action. *Journal of Biological Chemistry* **265**, 12232–12239 (1990).

[13] Lichte, K. *et al.* Lysophospholipid Receptor-Mediated Calcium Signaling in Human Keratinocytes. *Journal of Investigative Dermatology* **128**, 1487–1498 (2008).

[14] Shao, X., Li, Q., Mogilner, A., Bershadsky, A. D. & Shivashankar, G. V. Mechanical stimulation induces formin-dependent assembly of a perinuclear actin rim. *Proceedings of the National Academy of Sciences* **112**, E2595–E2601 (2015).

[15] Hung, W.-C. *et al.* Confinement Sensing and Signal Optimization via Piezo1/PKA and Myosin II Pathways. *Cell Reports* **15**, 1430–1441 (2016).

[16] Wales, P. *et al.* Calcium-mediated actin reset (CaAR) mediates acute cell adaptations. *eLife* **5**, e19850 (2016).

[17] Kim, T.-J. *et al.* Substrate rigidity regulates Ca2+ oscillation via RhoA pathway in stem cells. *Journal of Cellular Physiology* **218**, 285–293 (2009).

[18] Kim, T.-J. *et al.* Distinct mechanisms regulating mechanical force-induced Ca2+ signals at the plasma membrane and the ER in human MSCs. *eLife* **4**, e04876 (2015).

[19] Tsai, F.-C., Kuo, G.-H., Chang, S.-W. & Tsai, P.-J. Ca2+ Signaling in Cytoskeletal Reorganization, Cell Migration, and Cancer Metastasis. *BioMed Research International* **2015**, e409245 (2015).

[20] Wei, C. *et al.* Calcium Flickers Steer Cell Migration. *Nature* **457**, 901–905 (2009).

[21] Ridley, A. J. *et al.* Cell Migration: Integrating Signals from Front to Back. *Science* **302**, 1704–1709 (2003).

[22] Tigyi, G., Dyer, D. L. & Miledi, R. Lysophosphatidic acid possesses dual action in cell proliferation. *Proceedings of the National Academy of Sciences* **91**, 1908–1912 (1994).

[23] Ni, Q. *et al.* Signaling diversity of PKA achieved via a Ca2+-cAMP-PKA oscillatory circuit. *Nature Chemical Biology* **7**, 34–40 (2011).

[24] Sassone-Corsi, P. The Cyclic AMP Pathway. *Cold Spring Harbor Perspectives in Biology* **4**, a011148 (2012).

[25] Purvis, J. E. & Lahav, G. Encoding and Decoding Cellular Information through Signaling Dynamics. *Cell* **152**, 945–956 (2013).

[26] Santos, S. D. M., Verveer, P. J. & Bastiaens, P. I. H. Growth factor-induced MAPK network topology shapes Erk response determining PC-12 cell fate. *Nature Cell Biology* **9**, 324–330 (2007).

[27] Batchelor, E., Loewer, A., Mock, C. & Lahav, G. Stimulus-dependent dynamics of p53 in single cells. *Molecular Systems Biology* **7**, 488 (2011).

[28] Purvis, J. E. *et al.* p53 Dynamics Control Cell Fate. *Science* **336**, 1440–1444 (2012).

[29] Dupont, G. & Combettes, L. Fine tuning of cytosolic Ca 2+ oscillations. *F1000Research* **5**, F1000 Faculty Rev–2036 (2016).

[30] Smedler, E. & Uhlén, P. Frequency decoding of calcium oscillations. *Biochimica et Biophysica Acta (BBA) - General Subjects* **1840**, 964–969 (2014).

[31] Noren, D. P. *et al.* Endothelial cells decode VEGF-mediated Ca2+ signaling patterns to produce distinct functional responses. *Science Signaling* **9**, ra20–ra20 (2016).

[32] Hannanta-anan, P. & Chow, B. Optogenetic Control of Calcium Oscillation Waveform Defines NFAT as an Integrator of Calcium Load. *Cell Systems* **2**, 283–288 (2016).

[33] Waters, C. M. & Bassler, B. L. QUORUM SENSING: Cell-to-Cell Communication in Bacteria. *Annual Review of Cell and Developmental Biology* **21**, 319–346 (2005).

[34] Mehta, P. & Gregor, T. Approaching the molecular origins of collective dynamics in oscillating cell populations. *Current Opinion in Genetics & Development* **20**, 574–580 (2010).

[35] Laman Trip, D. S. & Youk, H. Yeasts collectively extend the limits of habitable temperatures by secreting glutathione. *Nature Microbiology* **5**, 943–954 (2020).

[36] Chen, C.-C. *et al.* Organ-Level Quorum Sensing Directs Regeneration in Hair Stem Cell Populations. *Cell* **161**, 277–290 (2015).

[37] De Monte, S., d'Ovidio, F., Danø, S. & Sørensen, P. G. Dynamical quorum sensing: Population density encoded in cellular dynamics. *Proceedings of the National Academy of Sciences* **104**, 18377–18381 (2007).

[38] Bonner, J. T. *The social amoebae* (Princeton University Press, 2008).

[39] Richard, P. The rhythm of yeast. *FEMS microbiology reviews* **27**, 547–557 (2003).

[40] Danø, S., Sørensen, P. G. & others. Quantitative characterization of cell synchronization in yeast. *Proceedings of the National Academy of Sciences* **104**, 12732–12736 (2007).

[41] Gunawardena, J. Models in biology: 'accurate descriptions of our pathetic thinking'. *BMC Biology* **12**, 29 (2014).

[42] Berro, J. "Essentially, all models are wrong, but some are useful"—a cross-disciplinary agenda for building useful models in cell biology and biophysics. *Biophysical Reviews* **10**, 1637–1647 (2018).

[43] Howard, J. Quantitative cell biology: The essential role of theory. *Molecular Biology of the Cell* **25**, 3438–3440 (2014).

[44] Zhu, X., Hager, E. R., Huyan, C. & Sgro, A. E. Leveraging the model-experiment loop: Examples from cellular slime mold chemotaxis. *Experimental Cell Research* **418**, 113218 (2022).

[45] Wang, S.-W. & Tang, L.-H. Emergence of collective oscillations in adaptive cells. *Nature Communications* **10**, 5613 (2019).

[46] Papin, J. & Subramaniam, S. Bioinformatics and cellular signaling. *Current Opinion in Biotechnology* **15**, 78–81 (2004).

[47] Emmert-Streib, F., Dehmer, M. & Haibe-Kains, B. Gene regulatory networks and their applications: understanding biological and medical problems in terms of networks. *Frontiers in Cell and Developmental Biology* **2** (2014).

[48] Yan, J., Risacher, S. L., Shen, L. & Saykin, A. J. Network approaches to systems biology analysis of complex disease: integrative methods for multi-omics data. *Briefings in Bioinformatics* **19**, 1370–1381 (2018).

[49] Samarth, N. H. & Singh, S. Methods to study systems biology of signaling networks: A case study of NSCLC. In *Advances in Protein Molecular and Structural Biology Methods*, 625–634 (Elsevier, 2022).

[50] Yao, J., Pilko, A. & Wollman, R. Distinct cellular states determine calcium signaling response. *Molecular Systems Biology* **12**, 894 (2016).

[51] Ganesan, A. & Zhang, J. How cells process information: Quantification of spatiotemporal signaling dynamics. *Protein Science : A Publication of the Protein Society* **21**, 918–928 (2012).

[52] McCormick, J. W., Pincus, D., Resnekov, O. & Reynolds, K. A. Strategies for Engineering and Rewiring Kinase Regulation. *Trends in Biochemical Sciences* **0** (2019).

[53] Kyung, T. *et al.* Optogenetic control of endogenous Ca 2+ channels in vivo. *Nature Biotechnology* **33**, 1092–1096 (2015).

[54] Kim, J. M., Lee, M., Kim, N. & Heo, W. D. Optogenetic toolkit reveals the role of Ca2+ sparklets in coordinated cell migration. *Proceedings of the National Academy of Sciences* **113**, 5952–5957 (2016).

[55] Lai, Y.-S. *et al.* Ca2+-regulated cell migration revealed by optogenetically engineered Ca2+ oscillations. *Journal of Cellular Physiology* **236**, 4681–4693 (2021).

[56] Potter, G. D., Byrd, T. A., Mugler, A. & Sun, B. Communication shapes sensory response in multicellular networks. *Proceedings of the National Academy of Sciences* **113**, 10334–10339 (2016).

[57] Bartos, M., Vida, I. & Jonas, P. Synaptic mechanisms of synchronized gamma oscillations in inhibitory interneuron networks. *Nature Reviews Neuroscience* **8**, 45–56 (2007).

[58] Liu, J. *et al.* Metabolic codependence gives rise to collective oscillations within biofilms. *Nature* **523**, 550–554 (2015).

[59] Prindle, A. *et al.* Ion channels enable electrical communication in bacterial communities. *Nature* **527**, 59–63 (2015).

[60] Durston, A. Dictyostelium: The Mathematician's Organism. *Current genomics* **14**, 355–360 (2013).

[61] Tomchik, K. J. & Devreotes, P. N. Adenosine 3',5'-Monophosphate waves in Dictyostelium discoideum: A demonstration by isotope Dilution–Fluorography. *Science (New York, N.Y.)* **212**, 443–446 (1981).

[62] Gregor, T., Fujimoto, K., Masaki, N. & Sawai, S. The Onset of Collective Behavior in Social Amoebae. *Science (New York, N.Y.)* **328**, 1021–1025 (2010).

[63] Sgro, A. E. *et al.* From intracellular signaling to population oscillations: Bridging size- and time-scales in collective behavior. *Molecular systems biology* **11** (2015).

[64] Chen, P.-S. *et al.* The initiation of the heart beat. *Circulation Journal* **74**, 221–225 (2010).

[65] De Monte, S., d'Ovidio, F., Danø, S. & Sørensen, P. G. Dynamical quorum sensing: Population density encoded in cellular dynamics. *Proceedings of the National Academy of Sciences* **104**, 18377–18381 (2007).

[66] François, P., Hakim, V. & Siggia, E. D. Deriving structure from evolution: Metazoan segmentation. *Molecular Systems Biology* **3**, 154 (2007).

[67] Atkinson, M. R., Savageau, M. A., Myers, J. T. & Ninfa, A. J. Development of Genetic Circuitry Exhibiting Toggle Switch or Oscillatory Behavior in Escherichia coli. *Cell* **113**, 597–607 (2003).

[68] Von Dassow, G. & Odell, G. M. Design and constraints of theDrosophila segment polarity module: Robust spatial patterning emerges from intertwined cell state switches. *Journal of Experimental Zoology* **294**, 179–215 (2002).

[69] Albert, R. & Othmer, H. G. The topology of the regulatory interactions predicts the expression pattern of the segment polarity genes in Drosophila melanogaster. *Journal of theoretical biology* **223**, 1–18 (2003).

[70] Ingolia, N. T. Topology and Robustness in the Drosophila Segment Polarity Network. *PLoS Biology* **2**, e123 (2004).

[71] Martiel, J.-L. & Goldbeter, A. A Model Based on Receptor Desensitization for Cyclic AMP Signaling in Dictyostelium Cells. *Biophysical Journal* **52**, 807–828 (1987).

[72] Laub, M. T., Loomis, W. F. & Shapiro, L. A Molecular Network That Produces Spontaneous Oscillations in Excitable Cells of Dictyostelium. *Molecular Biology of the Cell* **9**, 3521–3532 (1998).

[73] Maeda, M. *et al.* Periodic Signaling Controlled by an Oscillatory Circuit That Includes Protein Kinases ERK2 and PKA. *Science (New York, N.Y.)* **304**, 875–878 (2004).

[74] Kamino, K. *et al.* Fold-change detection and scale invariance of cell–cell signaling in social amoeba. *Proceedings of the National Academy of Sciences of the United States of America* **114**, E4149–E4157 (2017).

[75] Palo, G. D., Yi, D. & Endres, R. G. A critical-like collective state leads to long-range cell communication in Dictyostelium discoideum aggregation. *PLoS Biology* **15**, e1002602 (2017).

[76] Schwab, D. J., Baetica, A. & Mehta, P. Dynamical quorum-sensing in oscillators coupled through an external medium. *Physica D: Nonlinear Phenomena* **241**, 1782–1788 (2012).

[77] Noorbakhsh, J., Schwab, D. J., Sgro, A. E., Gregor, T. & Mehta, P. Modeling oscillations and spiral waves in Dictyostelium populations. *Physical review. E, Statistical, nonlinear, and soft matter physics* **91**, 062711 (2015).

[78] Izhikevich, E. M. *Dynamical systems in neuroscience: The geometry of excitability and bursting*. Computational neuroscience (MIT Press, Cambridge, Mass, 2007).

[79] Izhikevich, E. M. & FitzHugh, R. FitzHugh-Nagumo Model. *Scholarpedia* **1**, 1349 (2006).

[80] Adler, M. & Alon, U. Fold-change detection in biological systems. *Current Opinion in Systems Biology* **8**, 81–89 (2018).

[81] Ma, W., Trusina, A., El-Samad, H., Lim, W. A. & Tang, C. Defining Network Topologies that Can Achieve Biochemical Adaptation. *Cell* **138**, 760–773 (2009).

[82] Tsai, T. Y.-C. *et al.* Robust, Tunable Biological Oscillations from Interlinked Positive and Negative Feedback Loops. *Science (New York, N.Y.)* **321**, 126–129 (2008).

[83] Skataric, M. & Sontag, E. D. A Characterization of Scale Invariant Responses in Enzymatic Networks. *PLoS Computational Biology* **8**, e1002748 (2012).

[84] Adler, M., Szekely, P., Mayo, A. & Alon, U. Optimal Regulatory Circuit Topologies for Fold-Change Detection. *Cell Systems* **4**, 171–181.e8 (2017).

[85] Olsman, N. & Goentoro, L. Allosteric proteins as logarithmic sensors. *Proceedings of the National Academy of Sciences of the United States of America* (2016).

[86] Süel, G. M., Kulkarni, R. P., Dworkin, J., Garcia-Ojalvo, J. & Elowitz, M. B. Tunability and noise dependence in differentiation dynamics. *Science (New York, N.Y.)* **315**, 1716–1719 (2007).

[87] Süel, G. M., Garcia-Ojalvo, J., Liberman, L. M. & Elowitz, M. B. An excitable gene regulatory circuit induces transient cellular differentiation. *Nature* **440**, 545–550 (2006).

[88] Xiong, Y., Huang, C.-H., Iglesias, P. A. & Devreotes, P. N. Cells navigate with a local-excitation, global-inhibition-biased excitable network. *Proceedings of the National Academy of Sciences of the United States of America* **107**, 17079–17086 (2010).

[89] Shams, D. P., Yang, X., Mehta, P. & Schwab, D. J. Spatial gradient sensing and chemotaxis via excitability in *Dictyostelium discoideum*. *Physical Review E: Statistical Physics, Plasmas, Fluids, and Related Interdisciplinary Topics* **101**, 062410 (2020).

[90] Hubaud, A., Regev, I., Mahadevan, L. & Pourquié, O. Excitable Dynamics and Yap-Dependent Mechanical Cues Drive the Segmentation Clock. *Cell* **171**, 668–682.e11 (2017).

[91] Deneke, V. E., Melbinger, A., Vergassola, M. & Di Talia, S. Waves of Cdk1 activity in S phase synchronize the cell cycle in Drosophila embryos. *Developmental cell* **38**, 399–412 (2016).

[92] Danino, T., Mondragón-Palomino, O., Tsimring, L. & Hasty, J. A synchronized quorum of genetic clocks. *Nature* **463**, 326–330 (2010).

[93] Prindle, A. *et al.* A sensing array of radically coupled genetic 'Biopixels'. *Nature* **481**, 39–44 (2012).

[94] Trepat, X., Chen, Z. & Jacobson, K. Cell Migration. In *Comprehensive Physiology*, 2369–2392 (John Wiley & Sons, Ltd, 2012).

[95] SenGupta, S., Parent, C. A. & Bear, J. E. The principles of directed cell migration. *Nature Reviews Molecular Cell Biology* **22**, 529–547 (2021).

[96] Seetharaman, S. & Etienne-Manneville, S. Cytoskeletal Crosstalk in Cell Migration. *Trends in Cell Biology* **30**, 720–735 (2020).

[97] Howe, A. K. Regulation of actin-based cell migration by cAMP/PKA. *Biochimica et Biophysica Acta (BBA) - Molecular Cell Research* **1692**, 159–174 (2004).

[98] Svec, K. V. & Howe, A. K. Protein Kinase A in cellular migration—Niche signaling of a ubiquitous kinase. *Frontiers in Molecular Biosciences* **9** (2022).

[99] Newell-Litwa, K. A. & Horwitz, A. R. Cell Migration: PKA and RhoA Set the Pace. *Current Biology* **21**, R596–R598 (2011).

[100] Jin, H. *et al.* A PKA-Csk-pp60Src signaling pathway regulates the switch between endothelial cell invasion and cell-cell adhesion during vascular sprouting. *Blood* **116**, 5773–5783 (2010).

[101] Toriyama, M. *et al.* Phosphorylation of Doublecortin by Protein Kinase A Orchestrates Microtubule and Actin Dynamics to Promote Neuronal Progenitor Cell Migration. *The Journal of Biological Chemistry* **287**, 12691–12702 (2012).

[102] Sinha, C. *et al.* PKA and Actin Play Critical Roles as Downstream Effectors in MRP4-Mediated Regulation of Fibroblast Migration. *Cellular signalling* **27**, 1345–1355 (2015).

[103] Howe, A. K., Baldor, L. C. & Hogan, B. P. Spatial regulation of the cAMP-dependent protein kinase during chemotactic cell migration. *Proceedings of the National Academy of Sciences* **102**, 14320–14325 (2005).

[104] Tkachenko, E. *et al.* Protein kinase A governs a RhoA–RhoGDI protrusion–retraction pacemaker in migrating cells. *Nature Cell Biology* **13**, 660–667 (2011).

[105] Lochner, A. & Moolman, J. A. The Many Faces of H89: A Review. *Cardiovascular Drug Reviews* **24**, 261–274 (2006).

[106] Stierl, M. *et al.* Light Modulation of Cellular cAMP by a Small Bacterial Photoactivated Adenylyl Cyclase, bPAC, of the Soil Bacterium Beggiatoa. *Journal of Biological Chemistry* **286**, 1181–1188 (2011).

[107] Watabe, T., Terai, K., Sumiyama, K. & Matsuda, M. Booster, a Red-Shifted Genetically Encoded Förster Resonance Energy Transfer (FRET) Biosensor Compatible with Cyan Fluorescent Protein/Yellow Fluorescent Protein-Based FRET Biosensors and Blue Light-Responsive Optogenetic Tools. *ACS Sensors* (2020).

[108] Insel, P. A. & Ostrom, R. S. Forskolin as a Tool for Examining Adenylyl Cyclase Expression, Regulation, and G Protein Signaling. *Cellular and Molecular Neurobiology* 10 (2003).

[109] Bugaj, L. J. & Lim, W. A. High-throughput multicolor optogenetics in microwell plates. *Nature Protocols* **14**, 2205–2228 (2019).

[110] Jonkman, J. E. N. *et al.* An introduction to the wound healing assay using live-cell microscopy. *Cell Adhesion & Migration* **8**, 440–451 (2014).

[111] Pijuan, J. *et al.* In vitro Cell Migration, Invasion, and Adhesion Assays: From Cell Imaging to Data Analysis. *Frontiers in Cell and Developmental Biology* **7** (2019).

[112] Schmitt, J. M. & Stork, P. J. S. Cyclic AMP-Mediated Inhibition of Cell Growth Requires the Small G Protein Rap1. *Molecular and Cellular Biology* **21**, 3671 (2001).

[113] Yamada, T. *et al.* AVP inhibits EGF-stimulated MAP kinase cascade in Madin-Darby canine kidney cells. *Kidney International* **48**, 745–752 (1995).

[114] Niethammer, P. Components and Mechanisms of Nuclear Mechanotransduction. *Annual Review of Cell and Developmental Biology* **37**, 233–256 (2021).

[115] Alam, S. G. *et al.* The nucleus is an intracellular propagator of tensile forces in NIH 3T3 fibroblasts. *Journal of Cell Science* **128**, 1901–1911 (2015).

[116] Driscoll, T. P., Cosgrove, B. D., Heo, S.-J., Shurden, Z. E. & Mauck, R. L. Cytoskeletal to Nuclear Strain Transfer Regulates YAP Signaling in Mesenchymal Stem Cells. *Biophysical Journal* **108**, 2783–2793 (2015).

[117] Wang, Y. L. & Pelham, R. J. Preparation of a flexible, porous polyacrylamide substrate for mechanical studies of cultured cells. *Methods in Enzymology* **298**, 489–496 (1998).

[118] Dembo, M. & Wang, Y. L. Stresses at the cell-to-substrate interface during locomotion of fibroblasts. *Biophysical Journal* **76**, 2307–2316 (1999).

[119] Lekka, M., Gnanachandran, K., Kubiak, A., Zieliński, T. & Zemła, J. Traction force microscopy – Measuring the forces exerted by cells. *Micron* **150**, 103138 (2021).

[120] Parsons, J. T., Horwitz, A. R. & Schwartz, M. A. Cell adhesion: integrating cytoskeletal dynamics and cellular tension. *Nature Reviews Molecular Cell Biology* **11**, 633–643 (2010).

[121] Rigor, R. R., Shen, Q., Pivetti, C. D., Wu, M. H. & Yuan, S. Y. Myosin Light Chain Kinase Signaling in Endothelial Barrier Dysfunction. *Medicinal research reviews* **33**, 911–933 (2013).

[122] Ohta, Y., Akiyama, T., Nishida, E. & Sakai, H. Protein kinase C and cAMP-dependent protein kinase induce opposite effects on actin polymerizability. *FEBS Letters* **222**, 305–310 (1987).

[123] Riedl, J. *et al.* Lifeact: a versatile marker to visualize F-actin. *Nature Methods* **5**, 605–607 (2008).

[124] Melak, M., Plessner, M. & Grosse, R. Actin visualization at a glance. *Journal of Cell Science* **130**, 525–530 (2017).

[125] Belin, B. J., Goins, L. M. & Mullins, R. D. Comparative analysis of tools for live cell imaging of actin network architecture. *BioArchitecture* **4**, 189–202 (2014).

[126] Peterson, L. J. *et al.* Simultaneous Stretching and Contraction of Stress Fibers In Vivo. *Molecular Biology of the Cell* **15**, 3497–3508 (2004).

[127] Sugawara, M. *et al.* Dynamics of Actin Stress Fibers and Focal Adhesions during Slow Migration in Swiss 3T3 Fibroblasts: Intracellular Mechanism of Cell Turning. *BioMed Research International* **2016**, e5749749 (2016).

[128] Masur, S. K., Dewal, H. S., Dinh, T. T., Erenburg, I. & Petridou, S. Myofibroblasts differentiate from fibroblasts when plated at low density. *Proceedings of the National Academy of Sciences* **93**, 4219–4223 (1996).

[129] Hinz, B. Myofibroblasts. *Experimental Eye Research* **142**, 56–70 (2016).

[130] Pakshir, P. *et al.* The myofibroblast at a glance. *Journal of Cell Science* **133**, jcs227900 (2020).

[131] Schell, M. J., Erneux, C. & Irvine, R. F. Inositol 1,4,5-Trisphosphate 3-Kinase A Associates with F-actin and Dendritic Spines via Its N Terminus*. *Journal of Biological Chemistry* **276**, 37537–37546 (2001).

[132] Bindels, D. S. *et al.* mScarlet: a bright monomeric red fluorescent protein for cellular imaging. *Nature Methods* **14**, 53–56 (2017).

[133] Wang, R. & Brattain, M. G. The maximal size of protein to diffuse through the nuclear pore is larger than 60kDa. *FEBS letters* **581**, 3164–3170 (2007).

[134] Dong, J.-M., Leung, T., Manser, E. & Lim, L. cAMP-induced Morphological Changes Are Counteracted by the Activated RhoA Small GTPase and the Rho Kinase ROKα*. *Journal of Biological Chemistry* **273**, 22554–22562 (1998).

[135] Lu, D., Aroonsakool, N., Yokoyama, U., Patel, H. H. & Insel, P. A. Increase in Cellular Cyclic AMP Concentrations Reverses the Profibrogenic Phenotype of Cardiac Myofibroblasts: A Novel Therapeutic Approach for Cardiac Fibrosis. *Molecular Pharmacology* **84**, 787–793 (2013).

[136] Stephens, A. D., Banigan, E. J. & Marko, J. F. Chromatin's physical properties shape the nucleus and its functions. *Current opinion in cell biology* **58**, 76–84 (2019).

[137] Howe, A. K. Cross-talk between calcium and protein kinase A in the regulation of cell migration. *Current Opinion in Cell Biology* **23**, 554–561 (2011).

[138] Taylor, C. W. Regulation of IP3 receptors by cyclic AMP. *Cell Calcium* **63**, 48–52 (2017).

[139] Konieczny, V., Tovey, S. C., Mataragka, S., Prole, D. L. & Taylor, C. W. Cyclic AMP Recruits a Discrete Intracellular Ca 2+ Store by Unmasking Hypersensitive IP 3 Receptors. *Cell Reports* **18**, 711–722 (2017).

[140] Kim, S., Harris, M. & Varner, J. A. Regulation of Integrin αvβ3-mediated Endothelial Cell Migration and Angiogenesis by Integrin α5β1 and Protein Kinase A*. *Journal of Biological Chemistry* **275**, 33920–33928 (2000).

[141] Huang, C.-H. & Iglesias, P. A. Cell memory and adaptation in chemotaxis. *Proceedings of the National Academy of Sciences* **111**, 15287–15288 (2014).

[142] Ramakers, G. J. & Moolenaar, W. H. Regulation of astrocyte morphology by RhoA and lysophosphatidic acid. *Experimental Cell Research* **245**, 252–262 (1998).

[143] Feld, L. *et al.* Cellular contractile forces are nonmechanosensitive. *Science Advances* **6**, eaaz6997 (2020).

[144] Robinson, R. C. *et al.* Domain Movement in Gelsolin: A Calcium-Activated Switch. *Science* **286**, 1939–1942 (1999).

[145] Gremm, D. & Wegner, A. Gelsolin as a calcium-regulated actin filament-capping protein. *European Journal of Biochemistry* **267**, 4339–4345 (2000).

[146] Nag, S. *et al.* Ca2+ binding by domain 2 plays a critical role in the activation and stabilization of gelsolin. *Proceedings of the National Academy of Sciences* **106**, 13713–13718 (2009).

[147] Bock, A. *et al.* Optical Mapping of cAMP Signaling at the Nanometer Scale. *Cell* **182**, 1519–1530 (2020).

[148] Zhang, J. Z. *et al.* Phase Separation of a PKA Regulatory Subunit Controls cAMP Compartmentation and Oncogenic Signaling. *Cell* **182**, 1531–1544 (2020).

[149] Stoufflet, J. *et al.* Primary cilium-dependent cAMP/PKA signaling at the centrosome regulates neuronal migration. *Science Advances* **6**, eaba3992 (2020).

[150] Truong, M. E. *et al.* Vertebrate cells differentially interpret ciliary and extraciliary cAMP. *Cell* **184**, 2911–2926 (2021).

[151] Hofer, A. M. Interactions between calcium and cAMP signaling. *Current Medicinal Chemistry* **19**, 5768–5773 (2012).

[152] Zaccolo, M. & Pozzan, T. cAMP and Ca2+ interplay: a matter of oscillation patterns. *Trends in Neurosciences* **26**, 53–55 (2003).

[153] Eisner, D. A., Caldwell, J. L., Kistamás, K. & Trafford, A. W. Calcium and Excitation-Contraction Coupling in the Heart. *Circulation Research* **121**, 181–195 (2017).

[154] Yusa, K., Rad, R., Takeda, J. & Bradley, A. Generation of transgene-free induced pluripotent mouse stem cells by the *piggyBac* transposon. *Nature Methods* **6**, 363–369 (2009).

[155] Schindelin, J. *et al.* Fiji: an open-source platform for biological-image analysis. *Nature Methods* **9**, 676–682 (2012).

[156] Van Rossum, G. & Drake, F. L. *Python 3 Reference Manual* (CreateSpace, Scotts Valley, CA, 2009).

[157] Shcherbakova, D. M. *et al.* Bright monomeric near-infrared fluorescent proteins as tags and biosensors for multiscale imaging. *Nature Communications* **7**, 12405 (2016).

[158] van der Walt, S. *et al.* scikit-image: image processing in Python. *PeerJ* **2**, e453 (2014).

[159] Virtanen, P. *et al.* SciPy 1.0: fundamental algorithms for scientific computing in Python. *Nature Methods* **17**, 261–272 (2020).

[160] Tse, J. R. & Engler, A. J. Preparation of hydrogel substrates with tunable mechanical properties. *Current Protocols in Cell Biology* **Chapter 10**, Unit 10.16 (2010).

[161] Muncie, J. M. *et al.* Mechanical Tension Promotes Formation of Gastrulation-like Nodes and Patterns Mesoderm Specification in Human Embryonic Stem Cells. *Developmental Cell* **55**, 679–694.e11 (2020).

[162] Tseng, Q. *et al.* Spatial organization of the extracellular matrix regulates cell-cell junction positioning. *Proceedings of the National Academy of Sciences* **109**, 1506–1511 (2012).

[163] Martiel, J.-L. *et al.* Chapter 15 - Measurement of cell traction forces with ImageJ. In Paluch, E. K. (ed.) *Methods in Cell Biology*, vol. 125 of *Biophysical Methods in Cell Biology*, 269–287 (Academic Press, 2015).

[164] Gibson, D. G. *et al.* Enzymatic assembly of DNA molecules up to several hundred kilobases. *Nature Methods* **6**, 343–345 (2009).

[165] Wei, C., Wang, X., Zheng, M. & Cheng, H. Calcium gradients underlying cell migration. *Current Opinion in Cell Biology* **24**, 254–261 (2012).

[166] Webb, S. E. & Miller, A. L. Calcium signalling during embryonic development. *Nature Reviews Molecular Cell Biology* **4**, 539–551 (2003).

[167] Zheng, S., Wang, X., Zhao, D., Liu, H. & Hu, Y. Calcium homeostasis and cancer: insights from endoplasmic reticulum-centered organelle communications. *Trends in Cell Biology* **0** (2022).

[168] Dupont, G., Combettes, L., Bird, G. S. & Putney, J. W. Calcium Oscillations. *Cold Spring Harbor Perspectives in Biology* **3**, a004226–a004226 (2011).

[169] Kuo, I. Y. & Ehrlich, B. E. Signaling in Muscle Contraction. *Cold Spring Harbor Perspectives in Biology* **7**, a006023 (2015).

[170] Godbout, C. *et al.* The Mechanical Environment Modulates Intracellular Calcium Oscillation Activities of Myofibroblasts. *PLoS ONE* **8**, e64560 (2013).

[171] Lembong, J., Sabass, B., Sun, B., Rogers, M. E. & Stone, H. A. Mechanics regulates ATP-stimulated collective calcium response in fibroblast cells. *Journal of the Royal Society Interface* **12** (2015).

[172] Liang, C. *et al.* Human cancer cells generate spontaneous calcium transients and intercellular waves that modulate tumor growth. *Biomaterials* **290**, 121823 (2022).

[173] Dana, H. *et al.* High-performance calcium sensors for imaging activity in neuronal populations and microcompartments. *Nature Methods* **16**, 649–657 (2019).

[174] Cluzel, C. *et al.* The mechanisms and dynamics of $\alpha v\beta 3$ integrin clustering in living cells. *Journal of Cell Biology* **171**, 383–392 (2005).

[175] Chen, J., Salas, A. & Springer, T. A. Bistable regulation of integrin adhesiveness by a bipolar metal ion cluster. *Nature Structural & Molecular Biology* **10**, 995–1001 (2003).

[176] Zhang, K. & Chen, J. The regulation of integrin function by divalent cations. *Cell Adhesion & Migration* **6**, 20–29 (2012).

[177] Sjaastad, M. D. & Nelson, W. J. Integrin-mediated calcium signaling and regulation of cell adhesion by intracellular calcium. *BioEssays* **19**, 47–55 (1997).

[178] Takao, M. & Nakao, S. Manganese Stimulates Ca^{2+} Mobilization in Human Gingival Fibroblasts. *International Journal of Oral-Medical Sciences* **4**, 148–153 (2006).

[179] Geraldo, L. H. M. *et al.* Role of lysophosphatidic acid and its receptors in health and disease: novel therapeutic strategies. *Signal Transduction and Targeted Therapy* **6**, 1–18 (2021).

[180] Kano, K. *et al.* Suppressing postcollection lysophosphatidic acid metabolism improves the precision of plasma LPA quantification. *Journal of Lipid Research* **62**, 100029 (2021).

[181] Jans, R. *et al.* Lysophosphatidic Acid Promotes Cell Migration through STIM1- and Orai1-Mediated Ca2+i Mobilization and NFAT2 Activation. *Journal of Investigative Dermatology* **133**, 793–802 (2013).

[182] Vicogne, D. *et al.* Fetal Bovine Serum impacts the observed N-glycosylation defects in TMEM165 KO HEK cells. *Journal of inherited metabolic disease* **43**, 357–366 (2020).

[183] Chen, R. F. Removal of Fatty Acids from Serum Albumin by Charcoal Treatment. *Journal of Biological Chemistry* **242**, 173–181 (1967).

[184] Yu, F.-X. *et al.* Regulation of the Hippo-YAP Pathway by G-Protein-Coupled Receptor Signaling. *Cell* **150**, 780–791 (2012).

[185] Sikora, M. J., Johnson, M. D., Lee, A. V. & Oesterreich, S. Endocrine Response Phenotypes Are Altered by Charcoal-Stripped Serum Variability. *Endocrinology* **157**, 3760–3766 (2016).

[186] Parrill, A. L., Sardar, V. M. & Yuan, H. Sphingosine 1-phosphate and lysophosphatidic acid receptors: agonist and antagonist binding and progress toward development of receptor-specific ligands. *Seminars in Cell & Developmental Biology* **15**, 467–476 (2004).

[187] Ohta, H. *et al.* Ki16425, a Subtype-Selective Antagonist for EDG-Family Lysophosphatidic Acid Receptors. *Molecular Pharmacology* **64**, 994–1005 (2003).

[188] Tang, Y. & Othmer, H. G. Frequency encoding in excitable systems with applications to calcium oscillations. *Proceedings of the National Academy of Sciences* **92**, 7869–7873 (1995).

[189] Dhyani, V. *et al.* GPCR mediated control of calcium dynamics: A systems perspective. *Cellular Signalling* **74**, 109717 (2020).

[190] Putney, J. W. & Bird, G. S. Calcium Signaling in Lacrimal Glands. *Cell calcium* **55**, 290–296 (2014).

[191] Schweizer, N., Kummer, U., Hercht, H. & Braunbeck, T. Amplitude-encoded calcium oscillations in fish cells. *Biophysical Chemistry* **159**, 294–302 (2011).

[192] Tang, J. *et al.* CD147 reinforces [Ca 2+] i oscillations and promotes oncogenic progression in hepatocellular carcinoma. *Oncotarget* **6**, 34831–34845 (2015).

[193] Deng, H., Gerencser, A. A. & Jasper, H. Signal integration by Ca2+ regulates intestinal stem-cell activity. *Nature* **528**, 212–217 (2015).

[194] Mehari, F. T. *et al.* Intravital calcium imaging in myeloid leukocytes identifies calcium frequency spectra as indicators of functional states. *Science Signaling* **15**, eabe6909 (2022).

[195] Aguilera, L. *et al.* Robustness of frequency vs. amplitude coding of calcium oscillations during changing temperatures. *Biophysical Chemistry* **245**, 17–24 (2019).

[196] Dupont, G. & Sneyd, J. Recent developments in models of calcium signalling. *Current Opinion in Systems Biology* **3**, 15–22 (2017).

[197] Tang, X., Benesch, M. G. K. & Brindley, D. N. Lipid phosphate phosphatases and their roles in mammalian physiology and pathology. *Journal of Lipid Research* **56**, 2048–2060 (2015).

[198] Tomsig, J. L. *et al.* Lipid phosphate phosphohydrolase type 1 (LPP1) degrades extracellular lysophosphatidic acid in vivo. *The Biochemical journal* **419**, 611–618 (2009).

[199] Rajagopal, S. & Shenoy, S. K. GPCR desensitization: Acute and prolonged phases. *Cellular Signalling* **41**, 9–16 (2018).

[200] Alcántara-Hernández, R., Hernández-Méndez, A., Campos-Martínez, G. A., Meizoso-Huesca, A. & García-Sáinz, J. A. Phosphorylation and Internalization of Lysophosphatidic Acid Receptors LPA1, LPA2, and LPA3. *PLoS ONE* **10**, e0140583 (2015).

[201] Zhao, J., Stephens, T. & Zhao, Y. Molecular Regulation of Lysophosphatidic Acid Receptor 1 Maturation and Desensitization. *Cell Biochemistry and Biophysics* **79**, 477–483 (2021).

[202] Tigyi, G. & Miledi, R. Lysophosphatidates bound to serum albumin activate membrane currents in Xenopus oocytes and neurite retraction in PC12 pheochromocytoma cells. *The Journal of Biological Chemistry* **267**, 21360–21367 (1992).

[203] Dubin, A. E., Herr, D. R. & Chun, J. Diversity of Lysophosphatidic Acid Receptor-Mediated Intracellular Calcium Signaling in Early Cortical Neurogenesis. *The Journal of Neuroscience* **30**, 7300–7309 (2010).

[204] Chen, C., Corbley, M. J., Roberts, T. M. & Hess, P. Voltage-Sensitive Calcium Channels in Normal and Transformed 3T3 Fibroblasts. *Science* **239**, 1024–1026 (1988).

[205] Ellefsen, K. L. *et al.* Myosin-II mediated traction forces evoke localized Piezo1-dependent Ca 2+ flickers. *Communications Biology* **2**, 1–13 (2019).

[206] Franklin, J. M., Ghosh, R. P., Shi, Q., Reddick, M. P. & Liphardt, J. T. Concerted localization-resets precede YAP-dependent transcription. *Nature Communications* **11**, 4581 (2020).

[207] Bae, C., Sachs, F. & Gottlieb, P. A. The Mechanosensitive Ion Channel Piezo1 Is Inhibited by the Peptide GsMTx4. *Biochemistry* **50**, 6295–6300 (2011).

[208] Yang, J. X. & Lin, Y. The action of PKA on smooth muscle myosin phosphorylation. *Life Sciences* **77**, 2669–2675 (2005).

[209] Lembong, J., Sabass, B. & Stone, H. A. Calcium oscillations in wounded fibroblast monolayers are spatially regulated through substrate mechanics. *Physical Biology* **14**, 045006 (2017).

[210] Inaba, H., Miao, Q. & Nakata, T. Optogenetic control of small GTPases reveals RhoA mediates intracellular calcium signaling. *Journal of Biological Chemistry* **296**, 100290 (2021).

[211] Narumiya, S., Ishizaki, T. & Ufhata, M. Use and properties of ROCK-specific inhibitor Y-27632. In Balch, W. E., Der, C. J. & Hall, A. (eds.) *Methods in Enzymology*, vol. 325 of *Regulators and Effectors of Small GTPases - Part D: Rho Family*, 273–284 (Academic Press, 2000).

[212] Dalton, G. D. & Dewey, W. L. Protein kinase inhibitor peptide (PKI): A family of endogenous neuropeptides that modulate neuronal cAMP-dependent protein kinase function. *Neuropeptides* **40**, 23–34 (2006).

[213] Liu, C., Ke, P., Zhang, J., Zhang, X. & Chen, X. Protein Kinase Inhibitor Peptide as a Tool to Specifically Inhibit Protein Kinase A. *Frontiers in Physiology* **11** (2020).

[214] Thurley, K. & Falcke, M. Derivation of Ca2+ signals from puff properties reveals that pathway function is robust against cell variability but sensitive for control. *Proceedings of the National Academy of Sciences* **108**, 427–432 (2011).

[215] Bruce, J. I. E., Straub, S. V. & Yule, D. I. Crosstalk between cAMP and Ca2+ signaling in non-excitable cells. *Cell Calcium* **34**, 431–444 (2003).

[216] Tinevez, J.-Y. *et al.* TrackMate: An open and extensible platform for single-particle tracking. *Methods* **115**, 80–90 (2017).

[217] Ershov, D. *et al.* Bringing TrackMate into the era of machine-learning and deep-learning (2021). URL `https://www.biorxiv.org/content/10.1101/2021.09.03.458852v2`.

[218] Stringer, C. & Pachitariu, M. Cellpose 2.0: how to train your own model (2022). URL `https://www.biorxiv.org/content/10.1101/2022.04.01.486764v1`.

[219] Pálsson, E. *et al.* Selection for spiral waves in the social amoebae Dictyostelium. *Proceedings of the National Academy of Sciences* **94**, 13719–13723 (1997).

[220] Sawai, S., Thomason, P. A. & Cox, E. C. An autoregulatory circuit for long-range self-organization in Dictyostelium cell populations. *Nature* **433**, 323–326 (2005).

[221] Grace, M. & Hütt, M.-T. Predictability of spatio-temporal patterns in a lattice of coupled FitzHugh–Nagumo oscillators. *Journal of The Royal Society Interface* **10**, 20121016 (2013).

[222] Grace, M. & Hütt, M.-T. Regulation of Spatiotemporal Patterns by Biological Variability: General Principles and Applications to Dictyostelium discoideum. *PLoS Computational Biology* **11**, e1004367 (2015).

[223] Vidal-Henriquez, E. & Gholami, A. Spontaneous center formation in Dictyostelium discoideum. *Scientific Reports* **9**, 3935 (2019).

[224] Zhai, X., Larkin, J. W., Süel, G. M. & Mugler, A. Spiral Wave Propagation in Communities with Spatially Correlated Heterogeneity. *Biophysical Journal* **118**, 1721–1732 (2020).

[225] Potter, G. D., Byrd, T. A., Mugler, A. & Sun, B. Dynamic Sampling and Information Encoding in Biochemical Networks. *Biophysical Journal* **112**, 795–804 (2017).

[226] Phillips, R. Theory in biology: Figure 1 or figure 7? *Trends in Cell Biology* **25**, 723–729 (2015).

[227] Martiel, J.-L. & Goldbeter, A. A Model Based on Receptor Desensitization for Cyclic AMP Signaling in Dictyostelium Cells. *Biophysical Journal* **52**, 807–828 (1987).

[228] Sgro, A. E. *et al.* From intracellular signaling to population oscillations: bridging size- and time-scales in collective behavior. *Molecular Systems Biology* **11** (2015).

[229] Klein, P., Theibert, A., Fontana, D. & Devreotes, P. N. Identification and cyclic AMP-Induced modification of the cyclic AMP receptor in Dictyostelium discoideum. *Journal of Biological Chemistry* **260**, 1757–1764 (1985).

[230] Cao, X., Yan, J., Shu, S., Brzostowski, J. A. & Jin, T. Arrestins function in cAR1 GPCR-Mediated signaling and cAR1 internalization in the development of Dictyostelium discoideum. *Molecular Biology of the Cell* **25**, 3210–3221 (2014).

[231] Novák, B. & Tyson, J. J. Design principles of biochemical oscillators. *Nature Reviews Molecular Cell Biology* **9**, 981–991 (2008).

[232] Kuramoto, Y. Self-entrainment of a population of coupled non-linear oscillators. In Araki, H. (ed.) *International Symposium on Mathematical Problems in Theoretical Physics*, Lecture Notes in Physics, 420–422 (Springer, Berlin, Heidelberg, 1975).

[233] Strogatz, S. H. From Kuramoto to Crawford: Exploring the onset of synchronization in populations of coupled oscillators. *Physica D: Nonlinear Phenomena* **143**, 1–20 (2000).

CURRICULUM VITAE